



Delft University of Technology

**Document Version**

Final published version

**Citation (APA)**

Yan Toe, C. (2026). *Dynamics of the Accumulation of Floating Plastic Particles in Open Channel Flow*. [Dissertation (TU Delft), Delft University of Technology]. <https://doi.org/10.4233/uuid:8ae1d057-a1c2-47f5-8747-7e412c9221f8>

**Important note**

To cite this publication, please use the final published version (if applicable). Please check the document version above.

**Copyright**

In case the licence states "Dutch Copyright Act (Article 25fa)", this publication was made available Green Open Access via the TU Delft Institutional Repository pursuant to Dutch Copyright Act (Article 25fa, the Taverne amendment). This provision does not affect copyright ownership.

Unless copyright is transferred by contract or statute, it remains with the copyright holder.

**Sharing and reuse**

Other than for strictly personal use, it is not permitted to download, forward or distribute the text or part of it, without the consent of the author(s) and/or copyright holder(s), unless the work is under an open content license such as Creative Commons.

**Takedown policy**

Please contact us and provide details if you believe this document breaches copyrights. We will remove access to the work immediately and investigate your claim.

*This work is downloaded from Delft University of Technology.*



# **Dynamics of the Accumulation of Floating Plastic Particles in Open Channel Flow**

**Chit Yan Toe**

# Dynamics of the Accumulation of Floating Plastic Particles in Open Channel Flow



# Dynamics of the Accumulation of Floating Plastic Particles in Open Channel Flow

DISSERTATION

for the purpose of obtaining the degree of doctor  
at Delft University of Technology  
by the authority of the Rector Magnificus,  
Prof.dr.ir. H. Bijl,  
Chair of the Board for Doctorates  
to be defended publicly on  
Thursday 21 May 2026 at 12:30

by

Chit YAN TOE

**This dissertation has been approved by the (co)promotors.**

**Composition of the doctoral committee:**

Rector Magnificus,	chairperson
Prof.dr.ir. W. S. J. Uijtewaal,	Delft University of Technology, <i>promotor</i>
Dr.ir. D. Wüthrich,	Delft University of Technology, <i>copromotor</i>

**Independent members:**

Prof.dr.ir. C. Poelma,	Delft University of Technology
Prof.dr. B. Dewals,	University of Liège, BE
Dr.ir. D. Valero Huerta,	Imperial College London, UK
Dr.ir. F. Huthoff,	IHE Delft Institute for Water Education, NL
Prof.dr.ir. B. J. Boersma,	Delft University of Technology, <i>reserve member</i>

**Other Member:**

Dr.ir. P. Simões Costa,	Delft University of Technology
-------------------------	--------------------------------

**nuffic**  
meet the world



This thesis was financially supported by the [Orange Knowledge Programme](#) of NUFFIC, [Rijkswaterstaat](#) under project no. 31180385, and [Seed Fund of Climate Action Programme](#) of TUDelft.

This work made use of computational resources of the DelftBlue supercomputer, provided by Delft High Performance Computing Centre (<https://www.tudelft.nl/dhpc>), and the Dutch national e-infrastructure with the support of the SURF Cooperative using grant no. EINF-11242 and grant no. EINF-12970.

Keywords: [Plastic waste](#), [Debris accumulation](#), [Wall-bounded turbulence](#)

Printed by: [Name of the Printing house](#)

Copyright © 2026 by Chit Yan Toe

ISBN: 978-94-6384-949-4

An electronic version of this dissertation is available at <https://repository.tudelft.nl>

---

This dissertation is dedicated to my father and those who make the world a better place.



# Contents

<b>Summary</b>	<b>xi</b>
<b>Samenvatting</b>	<b>xiii</b>
<b>အကျဉ်းချုပ်</b>	<b>xvii</b>
<b>1 Introduction</b>	<b>1</b>
1.1 Background . . . . .	3
1.2 Scientific challenges . . . . .	7
1.3 Thesis outline . . . . .	11
<b>2 Stability of an Idealised Floating Carpet</b>	<b>13</b>
2.1 Introduction . . . . .	15
2.2 Conceptual model for carpet stability . . . . .	17
2.3 Methods . . . . .	25
2.3.1 Experimental setup for experiments on carpet stability .	27
2.3.2 Experimental setup for velocity measurement under the stable carpet . . . . .	28
2.4 Results & Discussion . . . . .	30
2.4.1 Stability regime of the carpet formation . . . . .	30
2.4.2 Flow properties under a stable carpet . . . . .	32
2.4.3 Analysis of the stability of floating carpets . . . . .	37
2.5 Conclusions . . . . .	39
2.A Measurement of rise velocity of particles . . . . .	40
2.B Analysis of secondary currents . . . . .	40
<b>3 Numerical Simulation of an Open-to-Closed Channel Transi-   tion</b>	<b>45</b>
3.1 Introduction . . . . .	47

3.2	Methods . . . . .	50
3.2.1	Governing equations and numerical methods . . . . .	51
3.2.2	Simulation scenarios . . . . .	53
3.3	Results and Discussions . . . . .	56
3.3.1	Streamwise development of global quantities . . . . .	56
3.3.2	Skin friction . . . . .	67
3.3.3	Eddy viscosity and $z_m$ versus $z_{\tau=0}$ . . . . .	70
3.3.4	Streamlines near the transition and flow separation . . . . .	72
3.3.5	Principal-strain and vorticity . . . . .	75
3.3.6	Statistics of the forces on the particles . . . . .	78
3.4	Conclusions . . . . .	82
3.A	Validation of volume penalisation method in CaNS . . . . .	84
3.B	Determination of virtual origin and $k_{s\infty}$ . . . . .	85
3.C	Streamwise development of turbulent normal stresses . . . . .	87
3.D	Validation of case TS with Blasius profile . . . . .	88
3.E	Turbulence model of Donaldson et al. [1] . . . . .	89
<b>4</b>	<b>Drag and lift forces on a particle in different configurations with respect to a floating carpet</b>	<b>93</b>
4.1	Introduction . . . . .	95
4.2	Methods . . . . .	97
4.2.1	Flow configurations . . . . .	98
4.2.2	Numerical methods . . . . .	101
4.3	Results and Discussion . . . . .	103
4.3.1	Drag and lift forces . . . . .	103
4.3.2	Drag and lift coefficients . . . . .	111
4.4	Conclusions . . . . .	114
<b>5</b>	<b>Conclusion and Outlook</b>	<b>117</b>
5.1	Conclusion . . . . .	119
5.1.1	Societal Impacts . . . . .	123
5.2	Outlook . . . . .	124
5.2.1	Scientific aspects . . . . .	125
5.2.2	Societal aspects . . . . .	127
	<b>References</b>	<b>131</b>
	<b>Acknowledgements</b>	<b>141</b>

<b>Curriculum vitae</b>	<b>143</b>
<b>Scientific output</b>	<b>145</b>

## CONTENTS

---

# Summary

This thesis presents the fundamental insights into physical processes governing accumulation of plastic debris in rivers and canals. Plastic debris degrades ocean ecosystems and threatens human health through the food web, making it an urgent global issue. Since rivers transport large quantities of plastic waste to the ocean, intercepting them within river systems using waste-collection devices offers a promising mitigation strategy. Effective design and deployment of such devices require a solid understanding of the interactions between plastic debris, waste-collection devices, and the ambient flow conditions.

Accumulation of plastic debris at hydraulic structures in urban drainage systems can also increase flood risk by reducing conveyance capacity of the structures. Moreover, because debris accumulation can impose loads on hydraulic structures that exceed their design specifications, it can also compromise their structural durability. Therefore, quantifying the cumulative force of the debris accumulation is crucial for future-proof design of hydraulic structures.

This research investigates the stability of the debris accumulation, or the carpet, composed of floating spherical particles using laboratory experiments and numerical simulations. Two different kinds of particle instability are identified: (a) squeezing in which a particle inside the carpet is pushed by its neighbouring particles due to cumulative compressive force, and (b) erosion in which the particle at the leading edge of the carpet is dislodged owing to the incoming flow and pressure fluctuation forces.

In Chapter 2, analytical predictions for two instability modes are developed based on the force equilibrium between particle buoyancy and fluid forces. Squeezing instability is found mainly dependent on the cumulative shear stress along the carpet whereas erosion instability depends on streamline deflection angle of the approach flow associated with flow transition. The flow transition phenomenon is observed when the open channel transforms to the closed channel due to the debris accumulation layer, inducing an additional bound-

ary layer at the carpet. Streamwise development of velocity profiles obtained by velocity measurements using Laser Doppler Anemometry also proves the presence of flow transition and influence of the carpet on the ambient flow.

Chapter 3 focuses on flow transitions from open channel to smooth-closed channel and rough-closed channel using high-fidelity Direct Numerical Simulation with volume penalisation method. The presence of a smooth carpet induces the smooth turbulent boundary layer after initial phase of Blasius-type laminar boundary layer. However, a rough carpet leads directly to the rough turbulent boundary layer and an asymmetric closed channel due to the roughness differences between the top carpet and the bottom bed. In this asymmetric flow, the location of maximum velocity is observed to shift toward the bottom, and this location is also found to mismatch with that of zero shear stress, thereby complicating the assumption of  $k-\varepsilon$  turbulence closure models. Boundary layer development associated with the carpet causes a larger cumulative shear force on the carpet and consequently increasing higher probability of squeezing instability of the particle.

In Chapter 4, influence of the carpet on hydrodynamic forces (drag and lift) on the particles is investigated using the aforementioned numerical methods. Fixed particles are placed in different horizontal and vertical positions in the computational domain with respect to the carpet. Particles in the vicinity of leading edge of the carpet are observed to experience a strong downward force whilst the particles located in the flow separation zone (immediately after the leading edge) are impacted by larger fluctuation forces, thus leading to higher risk of erosion instability. Floating particles dislodged from the leading edge of the carpet can trap inside the particles of the downstream part of the carpet. Hence, these trapped particles are observed to be more stable due to the shielding effect of neighbouring particles.

Finally, Chapter 5 summarises the research findings, and recommends future research directions and societal applications. Field measurement campaigns are suggested to validate the model and to improve understanding of the physical processes governing debris accumulation at hydraulic structures, especially for different types and sizes of debris. Regarding societal applications, the impact of debris accumulation should be incorporated into urban flood forecasting models by including an additional friction term.

# Samenvatting

Dit proefschrift presenteert fundamentele inzichten in de fysische processen die de ophoping van plastic afval in rivieren en kanalen bepalen. Plastic afval tast de ecosystemen binnen oceanen aan en vormt een bedreiging voor de volksgezondheid via de voedselketen, waardoor het een urgent wereldwijd vraagstuk is. Omdat rivieren grote hoeveelheden plastic afval naar de oceaan transporteren, biedt het onderscheppen ervan binnen riviersystemen met behulp van afval-opvang apparaten een veelbelovende mitigatiestrategie. Een effectief ontwerp en een doeltreffende inzet van dergelijke inrichtingen vereisen een gedegen begrip van de wisselwerkingen tussen plastic afval, afval-opvang apparaten en de omgevingsstroomcondities.

Ophoping van plastic afval bij hydraulische kunstwerken in stedelijke afvoersystemen kan tevens het overstromingsrisico verhogen door de doorstroomcapaciteit van deze kunstwerken te verminderen. Bovendien kan ophoping van afval belastingen op hydraulische kunstwerken veroorzaken die de ontwerp-specificaties overschrijden, waardoor de constructieve duurzaamheid in gevaar kan komen. Het kwantificeren van de cumulatieve kracht van de afvalophoping is daarom van cruciaal belang voor het toekomstbestendig ontwerpen van hydraulische kunstwerken.

Dit onderzoek bestudeert de stabiliteit van de afvalophoping — ook wel het tapijt genoemd — bestaande uit drijvende bolvormige deeltjes, aan de hand van laboratoriumexperimenten en numerieke simulaties. Twee verschillende vormen van deeltjesinstabiliteit worden geïdentificeerd: (a) uitknippen, waarbij een deeltje binnenin het tapijt door zijn naburige deeltjes wordt weggedrukt als gevolg van de cumulatieve drukspanning, en (b) erosie, waarbij het deeltje aan de voorrand van het tapijt losraakt door de inkomende stroming en drukvariaties.

In Hoofdstuk 2 worden analytische voorspellingen voor beide instabiliteits modi ontwikkeld op basis van het krachterevenwicht tussen de drijfkraft van het deeltje en de vloeistofkrachten. De uitknijpinstabiliteit blijkt voornamelijk

afhankelijk te zijn van de cumulatieve schuifspanning langs het tapijt, terwijl erosie-instabiliteit afhankelijk is van de stroomlijnbuigingshoek van de toestromende stroming, samenhangend met de stromingsovergang. Het fenomeen van stromingsovergang wordt waargenomen wanneer het open kanaal overgaat in een gesloten kanaal als gevolg van de ophopingslaag, waardoor een aanvullende grenslaag aan het tapijt ontstaat. De stroomwaartse ontwikkeling van snelheidsprofielen, verkregen door snelheidsmetingen met Laser-Doppler-anemometrie, bevestigt tevens de aanwezigheid van stromingsovergang en de invloed van het tapijt op de omgevingsstroming.

Hoofdstuk 3 richt zich op de stromingsovergang van open kanaal naar glad gesloten kanaal en ruw gesloten kanaal, met behulp van hoogwaardige directe numerieke simulatie met de volumepenaliseringsmethode. De aanwezigheid van een glad tapijt induceert een gladde turbulente grenslaag na een initiële fase van een laminaire grenslaag van het Blasius-type. Een ruw tapijt leidt daarentegen rechtstreeks tot een ruwe turbulente grenslaag en een asymmetrisch gesloten kanaal als gevolg van de ruwheidsverschillen tussen het bovenste tapijt en de onderste bodem. In deze asymmetrische stroming verschuift de locatie van de maximale snelheid richting de bodem; deze locatie valt tevens niet samen met die van de nulschuifspanning, hetgeen de aanname van  $k - \varepsilon$  turbulentieafsluitingsmodellen compliceert. De grenslaagontwikkeling samenhangend met het tapijt veroorzaakt een grotere cumulatieve schuifkracht op het tapijt, en bijgevolg een hogere kans op uitknijpinstabiliteit van het deeltje.

In Hoofdstuk 4 wordt de invloed van het tapijt op de hydrodynamische krachten (weerstand en lift) op de deeltjes onderzocht met behulp van de eerdergenoemde numerieke methoden. Vaste deeltjes worden op verschillende horizontale en verticale posities in het rekendomein geplaatst ten opzichte van het tapijt. Deeltjes in de nabijheid van de voorrand van het tapijt ondervinden een sterke neerwaartse kracht, terwijl deeltjes in de stromingscheidingszone (onmiddellijk achter de voorrand) blootstaan aan grotere fluctuerende krachten, hetgeen leidt tot een hoger risico op erosie-instabiliteit. Drijvende deeltjes die losraken van de voorrand van het tapijt kunnen vastlopen tussen de deeltjes van het stroomafwaartse gedeelte van het tapijt. Deze ingesloten deeltjes blijken stabiel te zijn vanwege het afscherpende effect van de naburige deeltjes.

Tot slot vat Hoofdstuk 5 de onderzoeksbevindingen samen en worden aanbevelingen gedaan voor toekomstig onderzoek en maatschappelijke toepassingen. Veldmeetcampagnes worden aanbevolen ter validatie van het model en ter verbetering van het begrip van de fysische processen die afvalophoping bij

hydraulische kunstwerken bepalen, in het bijzonder voor verschillende typen en afmetingen van afval. Met betrekking tot maatschappelijke toepassingen dient de invloed van afvalophoping te worden opgenomen in stedelijke overstromingsvoorspellingsmodellen door een aanvullende wrijvingsterm te introduceren.



ဤပါရဂူဘွဲ့ ကျမ်းတွင် မြစ်ချောင်း များ နှင့် ရေမြောင်း များ အတွင်း ပလတ်စတစ် အမှိုက် များ စုပြုံလာ ရခြင်း၏ ရူပဗေဒ အကြောင်းရင်းခံ တရား များ နှင့် အကျိုး တရား များ ကို လေ့လာ သုတေသန ပြုထားပါသည်။ ပလတ်စတစ် အမှိုက် များသည် သမုဒ္ဒရာ ကြီး များ၏ ဂေဟစနစ်ကို ယိုယွင်း ပျက်စီးစေသည့် အပြင် လူသား တို့၏ကျန်းမာရေး ကိုလည်း အစာ ကွင်းဆက် မှ တဆင့် ခြိမ်းခြောက် လျက် ရှိပါသည်။ ထို့ကြောင့် လည်း ပလတ်စတစ် အမှိုက် ပြဿနာသည် ကမ္ဘာလုံးဆိုင်ရာ အရေးပေါ် ပြဿနာ ဖြစ်ပါသည်။ ပလတ်စတစ် အမှိုက် အမြောက်အမြားသည် မြစ်ချောင်း များမှ တဆင့် ပင်လယ် သမုဒ္ဒရာ ကြီး များ ဆီသို့ ဝင်ရောက် လျက် ရှိသောကြောင့် သမုဒ္ဒရာ ကြီး များ ဆီ မရောက် မှီ မြစ်ချောင်း များ အတွင်း၌ အချိန် မှီ ဆယ်ယူ ထား နိုင်ပါက အကျိုး ရလဒ်ပိုကောင်းမွန်နိုင်ပါသည်။ သို့ဖြစ်ရာ ထိရောက်လျင်မြန်သော အမှိုက်သိမ်းစက်ယန္တရားများ တီထွင်ဖန်တီး နိုင်ရန် နှင့် မြစ်ချောင်း များ အတွင်း ထိုစက်ယန္တရား များ စနစ်တကျ နေရာချထား နိုင်ရန်အတွက် အသိပညာ ဗဟုသုတများ ရှိရန်လိုအပ်ပါသည်။ အဆိုပါ အသိပညာဗဟုသုတများသည် မြစ်ချောင်း များ နှင့် အမှိုက်သရိုက် များအကြား ရူပဗေဒဆိုင်ရာအပြန်အလှန် ဆက်နွှယ်နှိုးနှောမှုသဘောတရားများဖြစ်ပါသည်။

မြစ်ချောင်း များ နှင့် ရေမြောင်း များ အတွင်း ရေထိန်းတံခါး များ ရှိရာ အမှိုက်သရိုက် များသည် ထိုရေထိန်း တံခါး များ အနောက်တွင် တဖြည်းဖြည်း စုစည်းပြီး အမှိုက်ပြင်ကြီးပမာ ဖြစ်ပေါ်လာပါသည်။ ထိုအခါ ရေစီးရေ လာကို ပိတ်ဆို့စေပြီး ရေကြီးရေလျှံဖြစ်ပေါ်ကာ လူမှုစီးပွား ထိခိုက်စေပါသည်။ ထိုကဲ့သို့သော ပြဿနာ များ ကို ဖြေရှင်းနိုင်ရန် အလို့ငှာ "အမှိုက်သရိုက် များ-ရေထိန်း အဆောက်အအုံ များ-မြစ်ကြောင်း အနေအထား" ထို ရုပ်သဘောသုံးခုအကြား အပြန်အလှန် အကျိုးသက်ရောက်မှုကို နားလည်တတ်ကျွမ်းရန်လိုအပ်လှပါသည်။ ဤပါရဂူဘွဲ့ ကျမ်းသည် အဆိုပါ ပြဿနာကို လေးနှစ်ကြာမျှ သုတေသနပြု လေ့လာမှတ်တမ်းတင်ထားသော စာအုပ်တစ်အုပ်ဖြစ်ပါသည်။

လေ့လာတွေ့ရှိထားသော သုတေသနရလဒ်များကို ဤစာအုပ်၏ အခန်းကြီး(၃) ခန်းတွင် အသေးစိတ် ဖော်ပြထား ရှိပါသည်။ အခန်း(၁) တွင် သုတေသန နိဒါန်းကို တင်ပြထားပြီး အခန်း(၅)တွင် သုတေသန ရလဒ် နှင့် ဆက်လက်လေ့လာရမည့် အကြောင်းအခြင်းအရာတို့ကို တင်ပြထားပါသည်။ အခန်း(၂) တွင် လက်တွေ့ စမ်းသပ်မှုကို အဓိကရှင်းလင်းတင်ပြထားပြီး အခန်း (၃) နှင့် အခန်း (၄) တွင် ကွန်ပျူတာတွက်ချက်မှုများကို ရှင်းလင်းဖော်ပြထားပါသည်။



# 1

## Introduction

“If people do not believe that mathematics is simple, it is only because they do not realize how complicated life is.”

— John von Neumann (1903 – 1957)



## 1.1 Background

Plastic waste results from human innovation, emerging from our development and use of synthetic materials called plastics. Plastics created by the chemists in 19<sup>th</sup> century has been used to manufacture light-weight and durable consumer products in daily lives since 1950s, when the mass production of plastics emerged [2]. However, because of their long-lasting durability and chemical structure, plastics do not break down quickly and safely in the environment after the duration of intended use. This causes plastic waste to accumulate in the terrestrial environment as shown in figure 1.1, threatening valuable ecosystems and human health [2]. Therefore, reducing and mitigating plastic pollution is an urgent priority, as highlighted by the United Nations’ Sustainable Development Goal (SDG) 14: “Conserve and sustainably use the oceans, seas, and marine resources for sustainable development.”



Figure 1.1: Plastic pollution in South Tangerang, Indonesia (photo: Tom Fisk).

Plastic debris is defined as “objects consisting of synthetic or heavily modified natural polymers as an essential ingredient that, when present in natural

1 environments without fulfilling an intended function, are solid and insoluble at 20 °C” by Hartmann et al. [3]. There exist multiple classifications for plastic debris based on (a) chemical compositions (polymers, additives, copolymers, composites), (b) solid state, (c) solubility, (d) size, (e) shape and structure, (f) colour, (g) origin [3], and (h) density. Based on the largest dimension of irregular-shaped debris, it can be categorized roughly as (a) nanoplastics: 1 to 1000 nm, (b) microplastics: 1 to < 1000 µm, (c) mesoplastics: 1 to < 10 mm, and (d) macroplastics: 1 cm and larger [3], while microplastics are defined as particles from 1 µm to 5 mm in the review by Thompson et al. [2]. Microplastics can be found primarily in the original source e.g. cosmetics and paints, and secondarily via the fragmentation of macroplastics which is considered a major source of microplastics in the marine environment [2]. These small-sized plastic particles can easily cause toxicological harm to animals, humans, and ecosystems [2]. The scope of this research is limited to the physical properties of debris, with an emphasis on floating macroplastic debris, which can negatively affect hydraulic structures through channel blockages [4], and can also break down into microplastics in the longer term.

To demonstrate the scale of macroplastic pollution, quantitative figures from published studies [2, 5] are presented. The global emission of macroplastic debris is estimated to be 52.1 [48.3–56.3] million metric tonnes per year (Mt/year), based on machine learning and probabilistic material flow analysis of data from 50,702 municipality-level administrations by Cottom et al. [6]. It is estimated that around 22.2 Mt of macroplastic waste are susceptible to entering aquatic environments annually [6]. According to Jambeck et al. [5], the estimated input of macroplastics from terrestrial sources to the marine environment ranges from 4.8 to 12.7 Mt in 2010. Based on four data sources (Ryberg et al. [7], The Pew Charitable Trusts [8], Jambeck et al. [5] and Organisation for Economic Co-operation and Development (OECD) [9]) Thompson et al. [2] quantified the average annual leakage of macroplastics from land to the ocean at approximately 7.6 Mt/year, with potentially disastrous consequences for essential marine resources.

Rivers are considered the main conveyor of plastic debris toward the ocean [2]. Once the plastic debris enters the ocean, it becomes more challenging to track and collect them due to a highly dynamic nature of the oceanic processes e.g. waves, currents, horizontal and vertical circulations and wind transport [10]. Hence, collecting macroplastic debris from the river will facilitate clean-up procedure before they reach the ocean and being further diluted and dispersed. In recent years, waste-collection devices have been installed in some

rivers to intercept floating macroplastic debris [11, 12]. Effectiveness of these devices are still questionable in relation to initial costs, regular maintenance, capturing efficiency, and ecological impacts [11, 12, 13], thus necessitating the scientific evidence to prove and improve their effectiveness.



Figure 1.2: Accumulation of macroplastic debris at hydraulic structures: (a) waste accumulation at a culvert in Ghana (photo: Delft Global Initiative), and (b) waste accumulation in an urban drainage system in Jamaica (photo: The Ocean Cleanup).

On the other hand, mismanaged macroplastic debris also harms urban drainage system due to the clogging or accumulation at hydraulic structures such as lock gates and culverts as shown in figure 1.2. These debris accumulations affect the performance of hydraulic structures and result in additional flooding. Furthermore, the accumulative loading of the debris can cause structural damage in hydraulic structures [14]. Hence, understanding the accumulation process of plastic debris is crucial to better design hydraulic structures. Including the processes of debris accumulation will also lead to accurate parametrisation for flow conveyance formulations that are used in operational flood models.

While plastic debris occurs in rivers in a wide range of sizes, shapes, densities, and materials [15], as also shown in figure 1.2, this research emphasises floating large debris that can cause significant blockage at hydraulic structures. Furthermore, to provide a fundamental understanding of the physical processes, spherical particles are considered as a simplification. Moreover, a single type of debris is considered in this study, although different types of plastic debris are typically observed collectively in reality.

This research addresses the physical processes of plastic debris accumulation at hydraulic structures, which include floatable waste-collection devices deployed in rivers, and culverts used in urban drainage systems. The overarching objective of this dissertation is:

to advance our understanding of accumulation processes of floating macro-sized particles at hydraulic structures, and analyse the stability of the accumulation layer under varying hydraulic conditions and particle properties.

To analyse the research problem, we subdivided the accumulation process into three subprocesses as shown in figure 1.3: (1) the overall stability of the accumulation layer, also called the carpet, and its dependency on the characteristics of flow and particles, (2) the flow response (e.g. mean flow velocity profile, turbulence intensities and boundary shear stresses) to the presence of the carpet, and (3) detailed analysis of hydrodynamic forces (lift and drag) acting on the individual particles located in different horizontal and vertical positions with respect to the carpet. Altogether these processes give a comprehensive description of the accumulation of floating macroplastics at hydraulic structures. In practice, both the plastic debris and flow around structures have huge diversities in appearance. We therefore have to simplify the debris as well as the flow geometry in order to improve our understanding of processes. In this study, plastic debris is simplified as positively buoyant, monodisperse spheres with uniform properties.

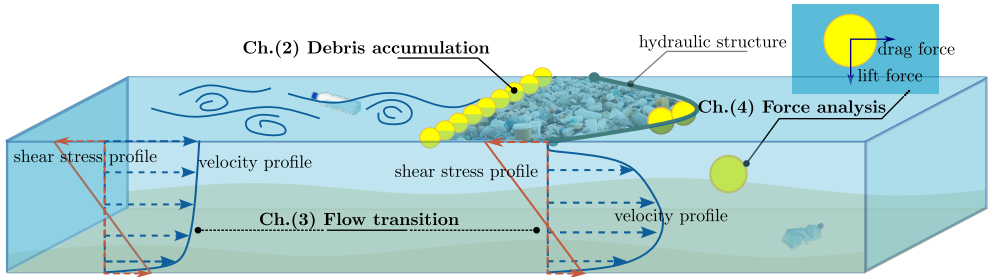


Figure 1.3: Three subprocesses of the debris accumulation at a hydraulic structure: (1) overall stability of the accumulation layer or the carpet, (2) flow response due to the presence of the accumulation layer, and (3) quantification of hydrodynamic forces action on the particle in different configurations with respect to the accumulation layer.

We study these three subprocesses in detail in the upcoming chapters. Before diving into these chapters, we highlight the scientific challenges encountered in understanding of accumulation process, fluid dynamics of flow transition, and quantification of particle forces in the presence of a carpet, in the following Sec. 1.2. These challenges are hindering the development of predictive modelling of plastic debris accumulation, and better parametrisation of conveyance parameters of hydraulic structures used in flood modelling.

## 1.2 Scientific challenges

The clogging of noncohesive particles has been studied mainly in micro-scale confined channels with a single-phase flow, whereas macro-scale particles in two-interface flows such as the air-water interface have received comparatively little attention [16]. Clogging of particles and thin (or) platelike particles in the channel forms a configuration that could resemble a line of spheres or a plane of plates, due to the forced boundary conditions [16]. This configuration can, however, deform if the driving force onto the particles or plates persists, and exceeds the restoring force. This leads to the instability of the layer as illustrated in figure 1.4 [17, 18, 19]. While previous studies (e.g. [17, 18]) focused on the buckling instability of the configuration in the single-phase channel, our understanding of the buckling in an open channel system remains limited.

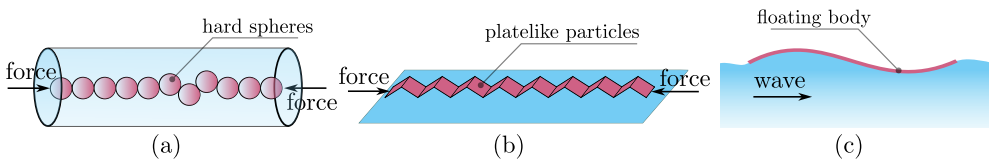


Figure 1.4: Different instability mechanisms: (a) buckling of force-chains in a cylindrical tube due to a compressive force [17], (b) folding of platelike particles at a water-air interface due to uniaxial compression [20], and motion of a floating elastic plate in waves [21].

Moreover, elastic motion of large floating bodies induced by ocean waves has also been investigated since it has implications on renewable energy and sea ice shelf [21, 22]. These bodies may be either monolithic or composed of several structurally connected components, other than surface friction, to prevent disintegration. This structural connection aspect differs from that of freely connected particles in the debris accumulation layer, which is the focus of the present study. Furthermore, interparticle forces vary between these two configurations, though both of them exist in free surface flow.

Given the complexity of interactions, physical processes of debris accumulation and subsequent breakup in open channel flow are not yet fully understood. Fundamentally, these processes can be described by the force balance of Newton's second law. However, the key challenge lies in identifying which types of forces are involved in these physical interactions and quantifying them through measurable parameters such as mean flow velocity, debris size, and

the densities of water and debris.

Hence, the initial step involves identifying the physical mechanisms responsible for debris accumulation and breakup using a controlled laboratory setting, which leads to the following research question:

(1) How does floating plastic debris accumulate at hydraulic structures to form a carpet layer, and under what conditions does the layer become unstable?

Similarly, it is important to know whether the presence of the carpet affects the open channel flow, and if so, how the flow responds to the carpet and vice versa. As illustrated in figure 1.3, the debris carpet imposes an additional boundary at the free surface of the river channel, thus transforming an open channel toward a closed channel by inducing a new boundary layer development at the carpet. Since the roughness of the debris carpet differs from that of the river bed, the flow in this closed channel can be considered an asymmetric closed channel. Such an asymmetric channel can also be observed at ice jams or driftwood accumulations in rivers [23, 24, 25].

Figure 1.5(a) schematises a closed channel where both walls are either smooth or rough (symmetric channel), or one wall is smooth while the other is rough (asymmetric channel). Flow in a closed symmetric channel has been extensively studied, particularly focusing on the streamwise evolution of the friction coefficient and the development length scales [26, 27]. Similarly, flow behaviour in an asymmetric channel was studied experimentally by Hanjalić and Launder [28] and numerically by Ikeda and Durbin [29], who considered a fully developed condition without including a flow transition. Due to the asymmetric roughness conditions, the resulting velocity profile and stress profile are also asymmetric, showing a substantial deviation compared to the profiles in a symmetric closed channel [28, 29]. Bradshaw et al. [30] proposed the superposition method for two interacting boundary layers in duct flow, as shown in figure 1.5(a), by using the empirical information of the basic boundary layer method.

As shown in figure 1.3, the free surface (i.e., slip boundary condition) of the open channel transitions toward a rough surface (i.e., no-slip boundary condition) due to the carpet. This gives rise to two different physical processes: (a) inducing a new boundary layer development at the carpet, and (b) formation of a step change in the roughness. Boundary layer development over a smooth or rough flat plate (e.g. figure 1.5(b)) has been a classical problem in fluid mechanics [34], emphasising the evolution of the friction coefficient along the surface. In case of a smooth surface, the flow encounters a laminar

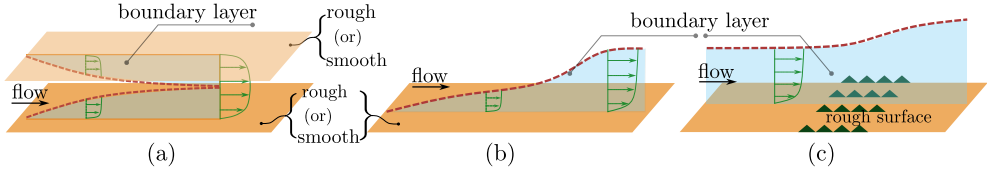


Figure 1.5: Different types of boundary layer development (a) in a closed channel in which both walls can be smooth or rough (symmetric [27]), or one wall is rough while other wall is smooth (asymmetric [28, 29]), (b) over a flat plate where the boundary can be rough or smooth [31, 32], and (c) over a surface with a step change in roughness [33].

regime, or Blasius boundary layer, for longer distance before transitioning to a turbulent boundary layer [31] whereas over a rough surface the transition to a boundary layer occurs earlier.

Flow response to a step change in roughness on the surface (figure 1.5(c)) has been studied experimentally and numerically [35, 33, 36]. Once the flow encounters a change in roughness, the boundary layer responds immediately near the surface, forming an internal boundary layer within the original one. Consequently, the shear stress and friction coefficient are also affected and need to be quantified to calculate the drag force and the cumulative shear force on the carpet. This research focuses on two physical processes: (1) flow transition from the open-to-closed channel including a new boundary layer at the top and a transition-induced boundary layer response at the bottom, and (2) an asymmetric closed channel with a rough top and a smooth bottom. This flow transition can impact the stability of the carpet, requiring a comprehensive assessment. Therefore, to better understand how the debris accumulation affects an open channel flow, we ask the following question,

(2) How does debris accumulation modify channel hydrodynamics such as boundary-layer development and momentum balance, and how do these changes affect the stability of the debris layer?

Flow acceleration will occur at the transition where the contracting flow can result in flow separation underneath the carpet immediately downstream [37]. These flow processes influence the hydrodynamic forces, drag and lift forces, acting on the individual particles inside the carpet. In other words, the drag and lift coefficients of the particles in the presence of a carpet need to be quantified, as they are important to estimate the destabilizing forces parametrically in the flood models.

The drag and lift forces acting on a sphere in a turbulent background flow have been studied by Homann et al. [38] for a particle in homogeneous and

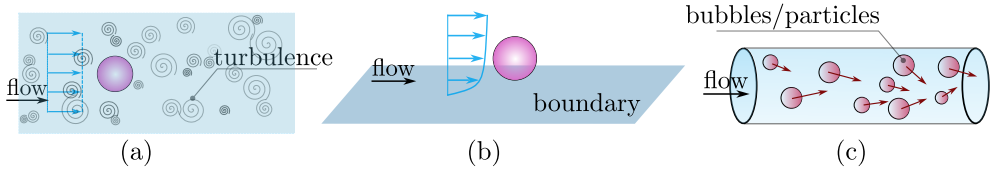


Figure 1.6: Particle in the flow: (a) with homogeneous and isotropic turbulence, (b) with a boundary layer, and (c) particle-laden flow in a closed pipe.

isotropic turbulence as shown in figure 1.6(a), and by Zeng et al. [39] for a particle located in a wall-bounded turbulence in figure 1.6(b), using high-fidelity numerical simulations. The intensity of turbulence in the flow influences the average drag and lift forces, and therefore causes an inaccuracy in traditional force correlations. In a particle-laden flow, the situation becomes complicated as particle-particle interaction plays an important role and the particles also move with the ambient flow, as illustrated in figure 1.6(c). Numerical simulation and experimental measurement of the hydrodynamic forces on each moving particle are challenging and computationally expensive [40, 41] though they provide a huge amount of information. This extensive simulation technique is suitable for modeling the dynamic motion of particles in the carpet; however, it is beyond the scope of our study, which focuses on determining the forces acting on quasi-static particles. In this study, we are interested in how the particles are influenced by the flow transition induced by the debris carpet within a turbulent flow, leading to the following research question

(3) How does the accumulation affect the hydrodynamic forces, drag and lift forces, acting on the individual particles in the vicinity of the transition point and underneath the layer?

The answer to this question will provide a better understanding of particle mobility in the flow transition, and instability mechanisms of the carpet. Finally, a thorough understanding of carpet formation, its influence on the flow dynamics, and hydrodynamic forces acting on the particles in the vicinity of the carpet will help fill knowledge gaps regarding debris accumulation of different materials, including logs, ice, and organic matter.

### 1.3 Thesis outline

The thesis starts with the experimental study of debris accumulation processes, and development of analytical framework for the carpet stability, detailed in Chapter 2. Chapter 3 discusses the hydrodynamic response to the presence of the carpet inducing a complex flow transition, especially bottom and top boundary layer developments, and their corresponding friction coefficients using numerical simulations. Moreover, the implication of flow transition on the particle mobility near the bottom boundary and instability of particles in the carpet is also discussed. In Chapter 4, we present the drag and lift forces acting on the individual particle located in different locations with respect to the carpet, and the corresponding force coefficients, which are also important for particle instability. Finally, Chapter 5 presents the concluding remarks and outlines future perspectives.



# 2

## Stability of an Idealised Floating Carpet <sup>◦</sup>

“It is the mark of an educated mind to rest satisfied with the degree of precision that the nature of the subject admits, and not to seek exactness when only an approximation is possible.”

— Aristotle, *Nicomachean Ethics*, Book I, Chapter 3

---

<sup>◦</sup>Published as: **Chit Yan Toe**, Wim Uijttewaal, and Davide Wüthrich, *Stability of an Idealized Floating Carpet of Plastic Spheres in an Open Channel Flow*, Journal of Hydraulic Engineering **151** (4), 04025010. Experiments, analysis and writing are done by Chit Yan Toe, supervision by Uijttewaal, and Wüthrich. Proofread by everyone.



## 2.1 Introduction

Plastic debris of different sizes, shapes, densities, and polymer compositions is constantly found in riverine, estuarine and marine environments, worsening their ecological and aesthetic values [42]. Moreover, high volumes of plastic waste can increase the risk of urban flooding [4], since accumulation of waste upstream of hydraulic structures (e.g., culverts, gates) reduces flow capacity of drainage systems [43]. Therefore, removal and disposal of plastic debris from aquatic environments is an urgent issue, aligning with the United Nations' sustainable development goal number 14 — *Conserve and sustainably use the oceans, seas and marine resources*.

Plastic debris in the ocean can be reduced in a cost-effective way if they are intercepted on land, since rivers are the main conveyors of debris toward the ocean [44]. Effective cleanup of plastic debris necessitates a thorough knowledge of not only their transport mechanisms in river systems, but also the impact of hydraulic structures on their pathways [44]. In fact, hydraulic structures including waste-collection devices disturb the transport of buoyant plastic debris in open channel flows, causing accumulation of debris upstream of the structures. This results in the formation of a so-called *floating carpet* (figure 2.1). Understanding the failure mechanism and stability criteria of the carpet is important for a better design of waste collection devices.

Similar accumulations of different materials is observed in rivers, for example, ice-jams [25, 24, 45, 46], and log-wood clogging at racks [47], bridges [48], and flexible barriers [49]. Most studies emphasize the impact of these accumulations on the increase of upstream water level. Among them, Jueyi et al. [45] focused on the stability of a carpet composed of ice particles using laboratory experiments. They used a floating foam panel to simulate an ice-jam and considered the motion of floating particles as representative of ice particles. The same study developed a relationship between shear Reynolds number and dimensionless shear stress for the incipient motion of individual ice particles, the so-called Shields parameter. This parameter can be used to estimate flow velocity required for ice particles to move from their initial position.

Similarly, designing waste-collection devices requires a better understanding of carpet formation processes and carpet stability to effectively capture plastic debris. However, few studies have thoroughly investigated how plastic debris accumulates upstream of structures to form a carpet, and how this

becomes unstable. Therefore, this study aims to better understand instability mechanisms of a floating carpet composed of buoyant spherical particles, including an assessment of the forces acting on it. An analytical framework is also developed to predict the threshold flow velocity for the particles to become unstable.



Figure 2.1: Accumulation of plastic debris at waste-collection devices, creating the so-called *carpet*. (a) Plastic debris captured by the floating boom, looking at upstream direction. (b) Aerial view of the carpet formations upstream of the waste-collection device. Photo Credit: The Ocean Cleanup.

In this research, we idealized a buoyant carpet upstream of a hydraulic structure as shown in figure 2.2. Real plastic debris was simplified as spherical particles to focus on the fundamental physical processes of the carpet. A carpet is considered stable if particles' restoring forces (e.g., buoyancy) are in equilibrium with hydraulic forces (e.g., drag force). Otherwise, the carpet becomes unstable and consequently particles inside the carpet will move in flow direction [45]. If a stable carpet is formed upstream of a hydraulic structure, a boundary layer develops under the carpet. Therefore, the velocity profile will transition from open channel flow to closed channel flow. Due to the carpet's additional resistance to the flow, upstream water level will also increase [47].

This paper focuses on the incipient motion of buoyant spherical particles of a carpet through laboratory experiments in a hydraulic flume using different flow velocities, leading to the development of analytical formulae. This paper is organized as follows — the next section presents the conceptual models for stability of the carpet formation, “Methods” section explains laboratory setups of the experiments conducted to investigate carpet stability and measure flow properties, “Results & Discussion” section discusses experimental findings and implications for carpet stability, while the main conclusions are drawn in the

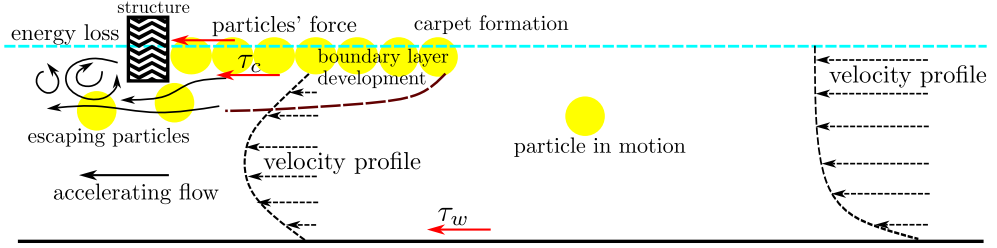


Figure 2.2: Idealization of the carpet formation with buoyant spherical particles captured at a hydraulic structure.  $\tau_c$  denotes the boundary shear stress under the carpet and  $\tau_w$  the boundary shear stress at the bottom of the channel.

final section.

## 2.2 Conceptual model for carpet stability

In this section, a conceptual model (figure 2.3a) is developed for the stability of the carpet, considering forces acting on individual particles. It is assumed that the hydraulic structure and individual particles do not deform due to the cumulative compressive force  $F_c$  of the particles and normal contact force  $F_n$  between particles. In a stable carpet, the forces acting on the particles are in equilibrium. This means that the buoyant force  $F_b$  and friction force  $F_t$  between particles balance the gravity force  $F_g$  in the vertical direction. Horizontally, the fluid drag force acting on the particle  $F_D$  is balanced by the reaction force  $F_n$  of the neighbouring particle. When particles are not perfectly aligned horizontally, the normal forces generate a vertical component that could exceed the buoyant force. This process is similar to the buckling phenomenon with compressed slender rods. In fact, Winkelmann et al. [17] and Tordesillas and Muthuswamy [18] observed buckling behaviour for a line of spheres under a longitudinal compressive force and a restoring centripetal force. The linear chain of spheres can turn into a ziz-zag pattern due to the longitudinal compressive force ( $F_c + F_D$ ) shown in Figs. 2.3a and 2.3b [17]. Kuhn and Chang [19] and Tordesillas and Muthuswamy [18] investigated theoretically and numerically the buckling phenomenon of a hexagonal close packing of the spheres to predict the positions of the particles in a matrix. However, in the present study the force chains of the carpet are in the horizontal plane and simplified to one dimension, as shown in figure 2.3a for the later analysis.

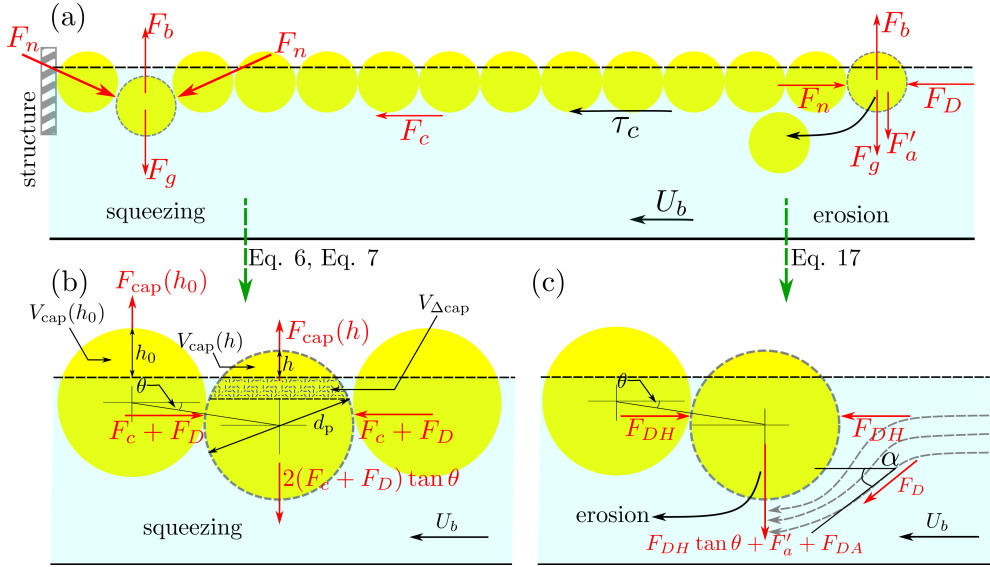


Figure 2.3: Conceptual model for carpet stability: (a) overview of forces acting on the carpet, (b) squeezing instability due to unbalance between vertical component of the cumulative compression force and restoring force, (c) erosion instability at the upstream edge owing to exceeding pressure fluctuation force and drag force. Normal force  $F_n$  is decomposed into horizontal component,  $F_n \cos \theta = F_c + F_D$ , and vertical component,  $F_n \sin \theta = (F_c + F_D) \tan \theta$ . In the figures,  $F_c$  denotes the compressive force,  $F_D$  the drag force on the particle,  $F_b$  the particle's buoyancy force,  $F_g$  the gravity force,  $F'_a$  the turbulent fluctuation force,  $F_{\text{cap}}$  the restoring force,  $F_{DH}$  horizontal component of  $F_D$  directing along the curved streamline,  $F_{DA}$  downward component of  $F_D$  resulting from the curved streamline,  $h_0$  initial submerged height,  $V_{\text{cap}}$  emerged volume of the sphere, and  $\theta$  the misalignment angle between the particles.

In this study, two instabilities are identified — (1) squeezing and (2) erosion. *Squeezing* instability is defined as the configuration of the carpet in which the particles are pushed toward each other by horizontal compressive forces ( $F_n \cos \theta = F_c + F_D$ ), resulting in a vertical displacement once the perfect alignment is disturbed. This in turn leads to vertical downward force, which is  $F_n \sin \theta = (F_c + F_D) \tan \theta$ . Figure 2.3b illustrates the squeezing phenomenon and defines variables at play. A buoyant particle inside the carpet floats as long as its net buoyancy, later referred to as restoring force, is larger than downward destabilizing force. The potential restoring force is proportional to the emerged volume  $V_{\text{cap}}$  of the particle. Since the restoring force  $F_{\text{cap}}$  varies with the submerged volume and thus the vertical position of the sphere in

water (or emerged height  $h$  of the sphere), we can write

$$F_{\text{cap}}(h) = \rho g V_{\text{cap}}(h) = \rho g \frac{\pi h^2}{3} \left( \frac{3}{2} d_p - h \right) \quad (2.1)$$

where

$$h = h_0 - d_p \sin \theta \quad (2.2)$$

in which  $h_0$  denotes the initial emerged height of the sphere before squeezing,  $g$  the acceleration due to gravity,  $d_p$  the diameter of the particle and  $\theta$  the misalignment angle between the center of the squeezed sphere and the fully floating sphere (figure 2.3b). Eq. 2.2 shows that (1) in the undisturbed situation  $\theta = 0$  then  $h = h_0$ , and (2) once the particle gets gradually submerged, the condition  $\theta > 0$  leads to  $h < h_0$ . Finally, for fully submerged spheres (i.e.,  $h = 0$ ), the maximum angle of submergence can be calculated as

$$\theta_{\text{max}} = \arcsin \left( \frac{h_0}{d_p} \right) \quad (2.3)$$

and  $h_0$  is found by solving for the volume equivalent to the reduced weight

$$\frac{\pi h_0^2}{3} \left( \frac{3}{2} d_p - h_0 \right) = \left( 1 - \frac{\rho_p}{\rho} \right) \frac{1}{6} \pi d_p^3 \quad (2.4)$$

where the left hand side is the initial emerged volume  $V_{\text{cap}}(h_0)$  that can be directly linked to the relative density of the particle,  $\rho_p/\rho$  where  $\rho_p$  is the density of the particle and  $\rho$  is the density of water.

During the squeezing process, the emerged volume of the sphere varies from the initially emerged volume  $V_{\text{cap}}(h_0)$  to a smaller emerged volume  $V_{\text{cap}}(h < h_0)$  by the amount of  $V_{\text{cap}}(h_0) - V_{\text{cap}}(h)$  in which  $h$  goes from  $h_0$  to 0. Therefore, the force required for this volume change  $V_{\Delta\text{cap}}$  to sink in the water is

$$F_{\Delta\text{cap}}(h) = F_{\text{cap}}(h_0) - F_{\text{cap}}(h) = \rho g [V_{\text{cap}}(h_0) - V_{\text{cap}}(h)]. \quad (2.5)$$

After some algebraic manipulations the required force  $F_{\Delta\text{cap}}(h)$  can be expressed in terms of the misalignment angle  $\theta$  as

$$F_{\Delta\text{cap}}(\theta) = \rho g \frac{\pi}{3} [3h_0 d_p^2 (\sin \theta + \sin^2 \theta) - 3h_0^2 d_p \sin \theta - d_p^3 \sin^2 \theta (\sin \theta + 1.5)]$$

or

$$F_{\Delta\text{cap}}(\theta) = \underbrace{\rho g \frac{\pi}{6} d_p^3}_{\text{sphere weight}} \underbrace{\left[ 6 \frac{h_0}{d_p} (\sin \theta + \sin^2 \theta) - 6 \frac{h_0^2}{d_p^2} \sin \theta - 2 \sin^2 \theta (\sin \theta + 1.5) \right]}_{\text{contribution due to changing geometry}} \quad (2.6)$$

Eq. 2.6 is shown in figure 2.4a as the dotted line depicting the relation between the generated restoring force  $F_{\Delta\text{cap}}$  and the misalignment angle  $\theta$  between two particles where the notation  $\uparrow$  in the figure indicates that the force is pointing upwards.

The vertical destabilizing force is acting on a particle within the carpet due to the vertical component of the cumulative compressive force transferred through the upstream particles. The cumulative compressive force consists mainly of (1) shear stress under the carpet  $F_c$ , and (2) drag force acting on the particle at the upstream edge of the carpet  $F_D$ . Only the vertical component of the cumulative compressive force ( $F_c + F_D$ ) will drag the sphere down by overcoming the required submerged force  $F_{\Delta\text{cap}}(\theta)$ . Therefore, for the sphere to be in equilibrium before squeezing occurs, there exists a vertical force balance such that

$$2(F_c + F_D) \tan \theta \leq F_{\Delta\text{cap}}(\theta) \quad (2.7)$$

assuming that the tangential component of the friction between particles is negligible. It should be noted that since the particle is squeezed by the compressive forces from both sides (as shown in figure 2.3b), the left hand side of Eq. 2.7 was multiplied by 2. The misalignment angle  $\theta$  can initially be caused by the infinitesimal motion inherited from turbulent fluctuations or surface oscillations, and slight differences in densities of the particles within the carpet. This misalignment angle will generate the downward component of compressive force acting on the particle. If the stabilising buoyant force is larger than the destabilizing force, then the particle will not move downwards and the carpet can be considered as stable.

The contribution of the shear force  $F_c$  can be estimated by integrating the shear stress  $\tau_c$  over the unit surface area of the carpet, which is product of the particle diameter  $d_p$  and carpet length  $\lambda$ , therefore resulting in  $F_c = \tau_c \lambda d_p$ . The shear stress acting on the carpet can be estimated as

$$\tau_c = \frac{1}{2} \rho C_f^t U_b^2 \quad (2.8)$$

where  $C_f^t$  denotes the friction coefficient of the carpet and  $U_b$  the bulk flow velocity.

Next, the particle drag force  $F_D$  can be calculated as

$$F_D = \frac{1}{2} \rho C_D U_b^2 A_p \quad (2.9)$$

where  $C_D$  is the drag coefficient of a sphere ( $\simeq 0.5$ ) and  $A_p$  is the frontal area of the sphere, which is approximated (for simplicity) as its whole cross-sectional area, i.e.  $A_p = \pi d_p^2/4$ .

Therefore, the expression for the vertical component of the compressive force acting on the particle during squeezing process will be

$$2(F_c + F_D) \tan \theta = \underbrace{\frac{1}{2} C_D \rho U_b^2 \frac{\pi}{4} d_p^2}_{\text{particle drag force}} \underbrace{\left[ \frac{8 C_f^t \lambda}{\pi C_D d_p} + 2 \right]}_{\text{carpet + edge}} \tan \theta \quad (2.10)$$

which defines the left hand side (LHS) of Eq. 2.7. For the quantities used in the experimental work later on, figure 2.4a shows the relation of downward force and restoring force as a function of  $\theta$  by substituting appropriate values for the parameters in Eq. 2.6 and Eq. 2.10. To do so, we used the values  $d_p = 19.95$  mm,  $\rho_p = 861.7$  kg/m<sup>3</sup>,  $C_f^t = 10.88 \times 10^{-3}$ ,  $\lambda = 2$  m, and  $C_D = 0.5$  in the following analysis. It is noted that the maximum limit of the  $\theta$ -axis in figure 2.4a shows that the particle will be fully submerged if the misalignment angle between the particles reaches the value of  $\theta_{\max} = 13.51^\circ$  for a typical density ratio  $\rho_p/\rho = 0.8617$ .

The dotted line in figure 2.4a describes the required force for squeezing the particle, as described by Eq. 2.6, while the solid lines describe the downward force acting on the particle as mentioned in Eq. 2.10, both forces varying with  $\theta$ . Again, the solid lines are represented for the downward force  $F_{\downarrow}(U_b)$  for different bulk velocities  $U_b$  where the notation  $\downarrow$  indicates downward direction. At  $\theta \simeq 0$ , i.e. the condition with small misalignment or disturbance, high flow velocities are required for the particle to be dragged down, whereas the particles under larger disturbances (large  $\theta$ ) are more likely squeezed because of larger downward component of compressive force.

From figure 2.4a, one can determine the flow velocity at which the particle is squeezed unconditionally, i.e., at  $\theta = 0$ , the so-called critical bulk velocity  $U_{b,c}$  for squeezing instability. To find the critical velocity  $U_{b,c}$ , the slope of the buoyancy force  $F_{\Delta\text{cap}}$  curve should be smaller than the slope of the downward force  $F_{\downarrow}(U_b)$  curve near  $\theta \simeq 0$  in figure 2.4a. Therefore, the critical bulk velocity that always results in instability is estimated by equating the slopes:

$$U_{b,c} = \sqrt{\frac{\left[ \frac{dF_{\Delta\text{cap}}}{d\theta} \right]_{\theta=0}}{C_D \rho \frac{\pi}{4} d_p^2 \left( \frac{4 C_f^t \lambda}{\pi C_D d_p} + 1 \right)}} \quad (2.11)$$

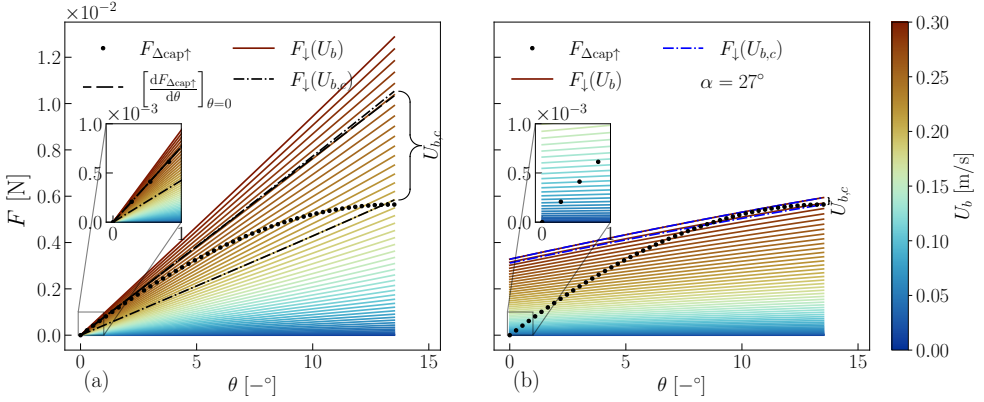


Figure 2.4: Force balance between the required force for submergence  $F_{\Delta\text{cap}\uparrow}$  (Eq. 2.6) and downward force  $F_{\downarrow}(U_b)$  (Eq. 2.10 for squeezing, and LHS of Eq. 2.17 for erosion). (a) Squeezing instability — Eq. 2.7, and (b) erosion instability — Eq. 2.15 at the angle of approach flow  $\alpha = 27^\circ$ . The force balance around misalignment angle  $\theta = 0$  are detailed in inset plots. In figure 2.4a, the upper dash-dotted line represents the downward force for  $U_{b,c} = 0.26$  m/s and the lower dash-dotted line for  $U_{b,c} = 0.21$  m/s. Both figures are considered for sphere diameter  $d_p = 19.95$  mm which is the large particle used in the experiments.

where

$$\left[ \frac{dF_{\Delta\text{cap}}}{d\theta} \right]_{\theta=0} = \rho g \frac{\pi}{6} d_p^3 \left( 6 \frac{h_0}{d_p} - 6 \frac{h_0^2}{d_p^2} \right) \quad (2.12)$$

as indicated by the dashed line. The corresponding downward force curve is also shown in figure 2.4a by the upper dash-dotted line that is very similar to the dashed line, especially near  $\theta = 0$ .

Contrary to such a strict definition of  $U_{b,c}$  for unconditional squeezing regardless of the magnitude of the perturbation, there might be different definitions of  $U_{b,c}$  for the particle to squeeze in case of strong perturbations. These circumstances can give rise to relatively low values of  $U_{b,c}$  compared to the case of unconditional squeezing. Different values of  $U_{b,c}$  for squeezing instability under different magnitudes of perturbations, i.e., from 0.21 m/s to 0.26 m/s, are indicated by the brace notation } in figure 2.4a while the lower limit of  $U_{b,c}$  is denoted by the lower dash-dotted line and the upper limit is denoted by the upper dash-dotted line whose slope is  $\left[ \frac{dF_{\Delta\text{cap}}}{d\theta} \right]_{\theta=0}$ .

In case of total submergence, i.e.,  $\theta = \theta_{\text{max}}$ , the buoyant force  $F_{\text{cap}} = \pi/6(\rho_p - \rho)gd_p^3$  can be expressed in terms of the particle rise velocity  $u_s$  as

follows:

$$F_{\text{cap}} = \frac{1}{2} \rho u_s^2 C_D A_p. \quad (2.13)$$

And, since it is known that  $F_{\text{cap}}$  is balanced against the downward force defined in Eq. 2.10, we equate Eq. 2.10 and Eq. 2.13 for the condition  $\theta = \theta_{\text{max}}$ ,

$$\frac{1}{2} \rho u_s^2 C_D A_p = \frac{1}{2} \rho U_b^2 C_D A_p \left[ \frac{8 C_f^t \lambda}{\pi C_D d_p} + 2 \right] \tan \theta_{\text{max}} \quad (2.14a)$$

$$\frac{u_s^2}{U_b^2} = \left[ \frac{8 C_f^t \lambda}{\pi C_D d_p} + 2 \right] \tan \theta_{\text{max}} \quad (2.14b)$$

implying that ratio of rise velocity to bulk flow velocity at the onset of instability depends on the carpet length, drag and friction coefficients.

In *erosion* instability, the particles upstream of the carpet are mobilized due to exceeding drag force compared to the restoring buoyancy force of the particle. Its graphical explanation is provided in figure 2.3c. The erosion instability is expected to be independent of the carpet length because the particles at the upstream edge do not experience any compressive force from upstream. Regarding the erosion instability of the most-upstream particle, the driving force for the particle's movement is the combination of three forces indicated in figure 2.3c. The first one is the downward component of the contact force induced by the adjacent particle,  $F_{DH} \tan \theta$ , in which  $F_{DH}$  denotes the horizontal component of the drag force directing along the curved streamline. The second one is turbulent (downward) fluctuation force  $F'_a$ , and the third one is the downward component of drag force,  $F_{DA}$ , resulting from the streamline angle of the approach flow bending downwards near the upstream edge of the carpet. Moreover, since the submergence of the particle can also increase the streamline angle, the total deflection angle of the streamline would be  $(\alpha + \theta)$  in which  $\alpha$  denotes the angle of the approach flow with respect to the horizontal axis.

Then, the force balance in vertical direction for erosion instability can be written as

$$F_{DH} \tan \theta + F'_a + F_{DA} \leq F_{\Delta \text{cap}}(\theta) \quad (2.15)$$

where

$$F_{DH} = \frac{1}{2} \rho C_D U_b^2 A_p \cos(\alpha + \theta), \text{ and } F_{DA} = \frac{1}{2} \rho C_D U_b^2 A_p \sin(\alpha + \theta). \quad (2.16)$$

As for the definition of  $F'_a$ , it can be considered as a pressure fluctuation multiplied by the submerged surface area of the sphere. Since the approach

flow is fully developed it is expected that the large scale turbulence that reaches the free surface can induce a significant distortion of the particle's vertical position. According to Calmet and Magnaudet [50], velocity fluctuations near the free surface can be characterised by the friction velocity  $u_*$ , implying that pressure fluctuations could also be characterised by  $\rho u_*^2 = 0.5\rho C_f U_b^2$ . Here,  $C_f$  denotes the friction coefficient of the flume bed as the turbulent fluctuations of the developed open channel flow are considered to be dominant.

Therefore, after rearrangements one can write Eq. 2.15 as

$$\frac{1}{2}\rho U_b^2 C_D A_p \left[ \cos(\alpha + \theta) \tan \theta + \frac{C_f}{C_D} + \sin(\alpha + \theta) \right] \leq F_{\Delta\text{cap}}(\theta). \quad (2.17)$$

Figure 2.4b shows the relation between destabilizing force and restoring force of Eq. 2.15 for  $\alpha = 27^\circ$ , which is the angle between vertical component and horizontal component of the approach flow measured in the laboratory experiment discussed in the Methods section and Appendix 2.B. The parameters used in figure 2.4b are the same as in figure 2.4a and refer to a large particle with diameter  $d_p = 19.95$  mm.

As the erosion instability is defined by the condition of the leading edge particle that is completely detached from the neighbouring particles, the force required for this instability to occur is equivalent to  $F_{\Delta\text{cap}}(h = 0)$ . When the particle is completely submerged, the required force does not change anymore, i.e.  $dF_{\Delta\text{cap}}/d\theta = 0$  but is equal to  $F_{\text{cap}}$ . Therefore in case of erosion instability  $\theta = \theta_{\text{max}}$ , the required force  $F_{\text{cap}}$  (Eq. 2.13) is balanced by the downward destabilizing force described in LHS of Eq. 2.17 as

$$\frac{1}{2}\rho u_s^2 C_D A_p = \frac{1}{2}\rho U_b^2 C_D A_p \left[ \cos(\alpha + \theta_{\text{max}}) \tan \theta_{\text{max}} + \frac{C_f}{C_D} + \sin(\alpha + \theta_{\text{max}}) \right] \quad (2.18a)$$

$$\frac{u_s^2}{U_b^2} = \cos(\alpha + \theta_{\text{max}}) \tan \theta_{\text{max}} + \frac{C_f}{C_D} + \sin(\alpha + \theta_{\text{max}}). \quad (2.18b)$$

Differently from the squeezing instability, here the ratio of particle's rise velocity to bulk velocity depends on the angle of approach flow  $\alpha$ , but not on the carpet length, as expected.

To estimate the critical bulk velocity required for erosion instability, we equate  $F_{\text{cap}}$  with the driving force at the instance of total submergence  $\theta_{\text{max}}$ , and after some mathematical manipulations we obtain

$$U_{b,c} = \sqrt{\frac{4(\rho - \rho_p)gd_p}{3\rho C_D \left[ \cos(\alpha + \theta_{\text{max}}) \tan \theta_{\text{max}} + \frac{C_f}{C_D} + \sin(\alpha + \theta_{\text{max}}) \right]}}. \quad (2.19)$$

The lower dash-dotted line in figure 2.4b shows the downward force of  $U_{b,c}$  required for the complete submergence under strong perturbation which is predicted by Eq. 2.19. For the moderate and weak perturbations, however, we can also identify higher values of  $U_{b,c}$  whose range is shown by the brace notation } in figure 2.4b. The above described phenomena will be used to interpret experimental observations.

Compared with the stability of ice particles, Jueyi et al. [45] considered only the general incipient motion of the particles under a fixed floating foam panel. Contrarily, in our study the carpet instability was categorised into two mechanisms, depending on the specific location of the spheres within the floating carpet. This means that the incipient motion considered by Jueyi et al. [45] shows similarities with our definition of erosion instability, which depends on the flow velocity and particle properties, but not on the number of particles in the carpet. Therefore, this shared dependence is reflected in both mathematical expressions of Eq. 2.19 and the Shields criterion  $\rho u_*^2 / (gd_p(\rho - \rho_p))$  defined by Jueyi et al. [45]. However, since we emphasized the erosion of only the leading edge particles in the carpet, Eq. 2.19 considers the flow deflection angle  $\alpha$ , which is not included in Jueyi et al. [45]’s Shields criterion.

## 2.3 Methods

To validate the conceptual model, two different series of experiments were performed in the Hydraulic Engineering Laboratory of Delft University of Technology. The first series of experiments aimed at mapping the stability regime of the plastic carpet by measuring the flow discharge and water depth (to calculate flow velocity  $U_b$ ) at the incipient motion of particles for different carpet lengths  $\lambda$ . The objective of the second series of experiments was to obtain the shear stress acting on the stable carpet formation by measuring the velocity profiles and consequently the cumulative compression force transferred by the upstream neighbouring particles to the downstream particle of the carpet.

Dimensions of the flume are length = 14.30 m  $\times$  width = 0.40 m  $\times$  height = 0.40 m, as shown in figure 2.5. To simulate the gate, a wooden board was installed in the flume so that moving particles were captured at its upstream side causing a carpet formation, as shown in figure 2.5. The thickness of the hydraulic structure is 6 cm, its width is 40 cm (same dimension as flume width), and clearance between the bottom of the flume and the structure is 10

cm. Flow discharge was measured using Proline Prosonic Flow 91W ultrasonic flow meter, and water levels were measured using three Microsonic acoustic displacement meters (model — mic+35/IU/TC), located at 3.0 m and 1.0 m upstream and 1.0 m downstream of the hydraulic structure. The measured values were recorded digitally via DasyLab Data Acquisition System, allowing a good synchronisation between all instruments.

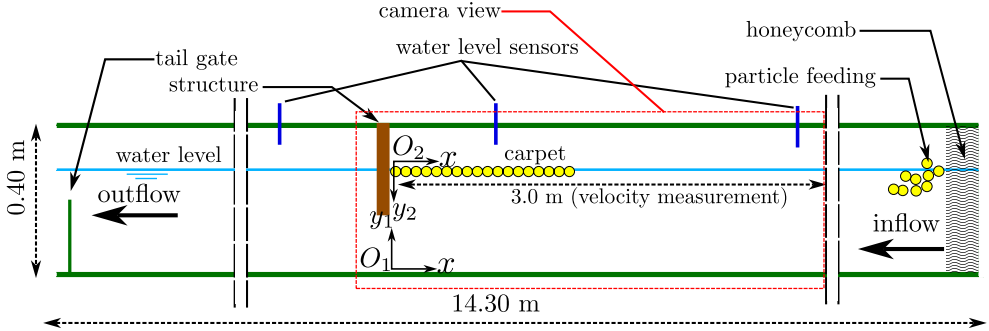


Figure 2.5: Schematic representation of experimental setup for the carpet formation (not to scale). Velocity measurements were performed every 25 cm in a range of 3 m upstream of the structure. Two different coordinate systems were used to analyse velocity profiles:  $O_1$  (from the bottom up) and  $O_2$  (from the surface down).

Two different sizes of buoyant spherical particles were used to simulate the carpet formation of the plastic debris. For the bigger particle class, diameter of the particle is  $d_p = 19.950 \text{ mm} \pm 0.03\%$  as measured by a vernier caliper device, and its mass was measured as  $3.58255 \text{ g} \pm 0.2\%$  using the METTLER AT261 DeltaRange<sup>®</sup> balance. Density of the particle was calculated by dividing its mass by the volume as  $\rho_p = 861.7 \text{ kg/m}^3 \pm 1\%$ . For the smaller particle  $d_p = 6.014 \text{ mm} \pm 0.06\%$  with a mass of  $0.10200 \text{ g} \pm 0.1\%$ , its density is  $\rho_p = 895.0 \text{ kg/m}^3 \pm 1\%$  using the same measurement procedure. The rise velocity of the particle, a property that shows the balance between buoyancy and drag forces, can be estimated by using an empirical formula based on the drag coefficient [51]. Particle's rise velocity reads

$$u_s = (\rho_p - \rho)g \sqrt{\frac{4d_p}{3\rho C_D} \frac{1}{|\rho_p - \rho|g}} \quad (2.20)$$

where  $C_D$  = drag coefficient of the particle computed as

$$C_D = \frac{24}{Re_p} + \frac{6}{1 + \sqrt{Re_p}} + 0.4 \quad (2.21)$$

for a solid sphere at  $Re_p < 2 \times 10^5$  in which  $Re_p$  denotes particle Reynolds number defined as  $Re_p \equiv u_s d_p / \nu$  where  $\nu$  is kinematic viscosity [51]. Using iterative calculation, the rise velocity for the bigger particle was predicted as 0.273 m/s and 0.112 m/s for the smaller ones. In our experiment, theoretical values of rise velocity  $u_s$  of the particles were compared to experimental values measured using a 2 m high water column, detailed in Appendix 2.A. After releasing the particle near the base of the water column, the particle's trajectory was recorded using a video recorder to calculate its rise velocity. This measurement was repeated for 13 times for bigger particles and 19 times for smaller particles. Different particles were used in each test to avoid any bias of manufacturing defects. The rise velocity of the bigger particle was found  $0.211 \pm 0.012$  m/s and the rise velocity of the smaller one was  $0.129 \pm 0.006$  m/s. The measured rise velocities are used in the subsequent analysis of carpet instability.

### 2.3.1 Experimental setup for experiments on carpet stability

This subsection describes the setup for the first series of experiments to investigate the stability of the carpet under different flow conditions. Therefore, for this experiment the motion of individual particles within the carpet was observed. Based on the analysis of carpet instabilities in the ‘‘Conceptual Model for Carpet Stability’’ section, it is expected that the squeezing instability is affected by the flow velocity and carpet length, normalised using the rise velocity and particle diameter, respectively, and the erosion instability is only by the flow velocity normalised by the rise velocity:

$$S = \underbrace{\mathcal{F}\left(\frac{\lambda}{d_p}, \frac{U_b}{u_s}\right)}_{\text{squeezing}} \quad \text{and} \quad S = \underbrace{\mathcal{F}\left(\frac{U_b}{u_s}\right)}_{\text{erosion}} \quad (2.22)$$

where  $S$  is a dimensionless Boolean value that gives True if the particle starts to move, or False if the particle remains its initial position.

Nine carpet lengths  $\lambda/d_p \simeq [25, 37.5, 50, 75, 87.5, 100, 125, 137.5, 150]$  using  $d_p = 19.95$  mm, and six different lengths  $\lambda/d_p \simeq [50, 75, 100, 112, 125, 150]$  for  $d_p = 6.014$  mm were analysed for these experiments. During the tests, plastic particles were inserted in the flume near its upstream inlet and they developed a carpet of the required length under a constant low discharge (figure 2.5). With this discharge the water depth was 12 cm and with such a

low discharge the particles accumulated at the hydraulic structure, creating a stable carpet. Then, the flow rate was gradually increased every 10 minutes. Since the tail gate in the flume was fixed during the experiments, the increase in discharge resulted in an increase in water level in the flume, which decreased the aspect ratio (i.e., flume width/water depth). Such a decrease can induce secondary currents in the flume, as discussed in Appendix 2.B. The process of carpet formation and its changing configuration were captured using a video camera at 25 frames per second with  $3840 \times 2160$  pixels resolution, and the camera view covered the complete length of each carpet as indicated in figure 2.5. The experiment was terminated the moment the particles in the carpet started to erode. Each test was repeated two times, with initial configuration of the carpet formation as similar as possible. Recorded videos were analysed visually to observe the stability of the carpet. Once a particle inside the carpet layer became completely submerged, it was denoted as squeezing. Erosion was defined as the complete detachment of a particle from the upstream edge of the carpet. Bulk flow velocity  $U_b$  was calculated by dividing the measured discharge by the cross-sectional flow area (i.e., flume width times water depth) at the instances of squeezing and erosion for different carpet lengths. After determining the instability thresholds for squeezing and erosion, a second series of experiments was performed in the same flume to measure velocity profiles and turbulent characteristics, including Reynolds stress profiles in the stable flow regime, i.e., with flow velocity smaller than the critical velocity responsible for carpet instability.

### 2.3.2 Experimental setup for velocity measurement under the stable carpet

In the second series of experiments, a stable carpet was generated based on the results of the first series. The flow discharge (Table 2.1) was kept constant throughout each experiment. To obtain information on the flow velocities and turbulence properties, detailed measurements were performed using two-dimensional Laser Doppler Velocimetry (LDV) system (WL-DelftHydraulics). The sensing volume of the LDV system is approximately  $0.1 \text{ mm}^3$  and the laser intensity is 6 mW He-Ne with wavelength of 632.8 nm. The measuring principle of the current LDV system makes use of a reference beam combined with two Bragg-cell shifted signal beams to measure the Doppler shifts of the two components in the vertical plane [52]. The length of the longest carpet examined in the experiment is 2 m and the shortest length is 0.5 m. All flow

conditions are subcritical ( $Fr \ll 1$ ) and turbulent ( $Re \gg 8000$ ). The velocity measurements with the particles of  $d_p = 19.95$  mm are summarized in Table 2.1.

Since the Froude number in this experiment ( $Fr \simeq 0.1$ , Table 2.1) is much smaller than the critical value  $Fr < 1$ , our experimental setup behaves similarly to the waste accumulation at hydraulic structures in the lowland rivers where the flow condition upstream of the structures is subcritical without noticeable free surface variation. This variation can affect the vertical motion of floating particles at the surface, influencing the stability of the carpet. More importantly, Reynolds number  $Re$  in our experiment is sufficiently large to generate a turbulent flow despite higher  $Re$  ( $\sim 10^6$ ) is often found in many rivers. Therefore, the friction coefficients and turbulence properties associated with the logarithmic velocity profile can be confidently applied in the analysis of the experimental data.

Table 2.1: Experimental flow conditions for velocity measurement using LDV system for the bigger particle  $d_p = 19.95$  mm.  $H$  : water depth;  $Q$  : flow rate;  $Re$  : Reynolds number ( $= U_b H / \nu$ );  $Fr$  : Froude number ( $= U_b / \sqrt{gH}$ ),  $U_b$  : bulk flow velocity.

	$H$ [cm]	$Q$ [ $\times 10^{-3}$ m <sup>3</sup> /s]	$\lambda$ [m]	$Re$ [-]	$Fr$ [-]
Case 1	12	4.8	2.00	12000	0.09
Case 2	12	4.8	1.00	12000	0.09
Case 3	20	7.1	1.00	17750	0.06
Case 4	11	3.4	0.75	8250	0.07
Case 5	12	4.8	0.50	12000	0.09

In each experiment, vertical profiles of horizontal and vertical flow velocities were measured every  $x = 25$  cm from the upstream face of the hydraulic structure in the upstream direction, by moving the LDV horizontally on the rail of the flume and vertically with a traversing system. Since the goal was to obtain the flow properties very close to the carpet, the LDV device was installed upside down which implied that the flow could not be sampled closer than 5 mm from the bottom. To check consistency between velocity and discharge measurements, the measured velocity values of Case 4 were averaged over the water depth, and this depth-averaged velocity was compared to the discharge measurement of the acoustic flow meter. The difference was found to be  $0.02 \times 10^{-3}$  m<sup>3</sup>/s, which is less than 1% and therefore considered acceptable.

Instantaneous horizontal and vertical components of the flow velocity were measured with a sampling frequency of 200 Hz to obtain vertical profiles of

mean velocity and Reynolds stresses. Measured profiles of Reynolds stresses can be used to estimate the friction velocity at the carpet and consequently its friction coefficient  $C_f^t$  to calculate the compressive force of the carpet  $F_c$ . Moreover, the friction velocity at the flume bottom can also be determined based on the Reynolds stress profile to estimate the turbulent fluctuation forces  $F'_a$  by means of  $\rho u_*^2$ .

## 2.4 Results & Discussion

This section presents the results from the two series of experiments separately. The result of the first series describes the stability regime for the different lengths of carpet formation under various flow conditions. The second series discusses velocity profiles and turbulent properties under the stable carpet.

### 2.4.1 Stability regime of the carpet formation

As shown in Eq. 2.22, the stability of the carpet depends on two dimensionless parameters —  $\lambda/d_p$  which indicates the number of particles in a carpet length, and  $U_b/u_s$  which reflects the ratio of the fluid force to buoyant force of the particle. Based on these parameters, observations of the carpet stability are summarised in figure 2.6 for different carpet lengths and two particle sizes,  $d_p = 19.95$  mm and  $d_p = 6.014$  mm.

A stable carpet was observed when the average flow velocity  $U_b$  was smaller than the particle's rise velocity (figure 2.6). Once the flow velocity exceeded this threshold value, the carpet became unstable via two instability modes, squeezing and erosion, as explained in “Conceptual Model for Carpet Stability” section, and visualised in Figs. 2.7a and 2.7b. In the experiments with longer carpets, squeezing instability occurred at lower velocities than erosion, whereas with short carpets both instabilities occurred with approximately the same velocity. When the erosion instability was triggered by flow velocity, the carpet configuration gradually transformed from a single-layer to a multi-layer (figure 2.7b). The latter cases were not considered in the present study.

The best-fit lines for each instability mode are shown in figure 2.6, although data points show some scatter most likely due to experimental disturbances by turbulence and surface waves, as well as imperfections in the carpet

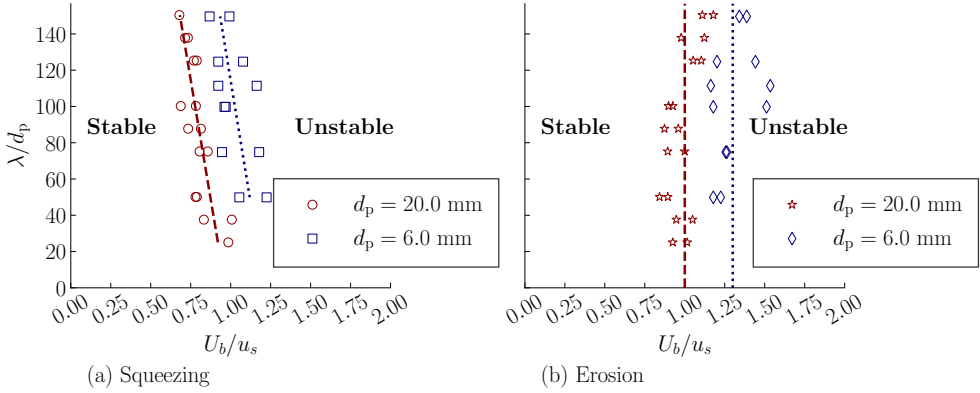
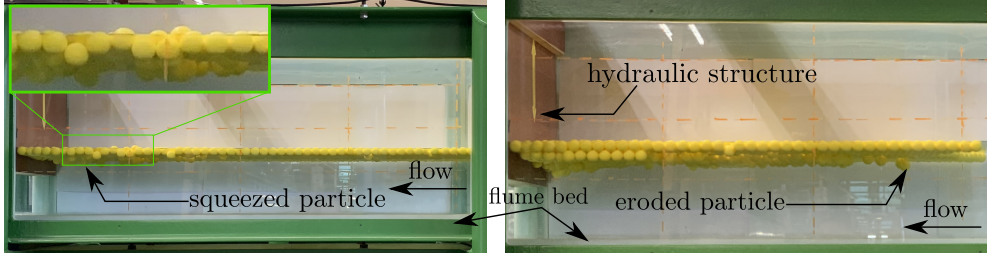


Figure 2.6: Stability regimes of the carpet formation based on  $U_b/u_s$  and  $\lambda/d_p$ . (a) Squeezing instability, and (b) erosion instability. Lines represent best-fit of the experimental data.

formation. Squeezing instability as observed in this experiment (figure 2.7a) is similar to the concept of buckling of linear force-chains in the research field of granular mechanics [17, 18].

Regarding erosion instability, we considered movement of the particles located *only* at the leading edge of the carpet (figure 2.7b). Fitting lines of this instability are also shown in figure 2.6b for both experiments with  $d_p = 19.95$  mm and  $d_p = 6.014$  mm. A good agreement with vertical lines aligns with the theoretical analysis that predicts no dependency on carpet length.

However, the fitting lines for different particle sizes do not collapse on a single line in the non-dimensional plot (figure 2.6). In particular, the stability of the smaller particles could be affected by forces not accounted for, e.g., surface tension. Moreover, secondary current in the flume explained in Appendix 2.B can attribute to this discrepancy of erosion instability. Another observation concerns the unexpected flow pattern upstream of the carpet, where a weak upstream influence of the carpet on the flow at the free-surface was observed during the experiment. Due to these disturbances, the particles at the upstream edge of the carpet might not experience the “full” flow velocity (also shown in Appendix 2.B), complicating the criterion of erosion instability. This unexpected flow behaviour requires further study in dedicated experiments.



(a) Squeezing instability.

(b) Erosion instability.

Figure 2.7: Pictures of two instability modes of the carpet formation. (a) Particles in the carpet are pushed against each other because of excessive force of the particles located in the upstream part of the carpet and hydrodynamic forces. Zig-zag pattern shown in inset is observed as a squeezing instability. (b) Once the flow rate reached a certain threshold, particles start to move from their initial location at the upstream edge to another location to form a multi-layer formation.

## 2.4.2 Flow properties under a stable carpet

This section estimates the shear stress developed under the stable carpet by analysing the velocity measurements under the longest carpet (Case 1 in Table 2.1). Two different coordinate systems were used to analyse the measured velocity profiles of Case 1 (figure 2.5). Lower coordinate system with origin  $O_1$  at the bed with  $y_1$  pointing upwards was applied for the study of flow near the bottom of the flume, whereas opposite-vertical coordinate system  $xO_2y_2$  with the origin at the free surface was used to characterise the flow just below the carpet formation (figure 2.5).

Qualitatively velocity data under the carpet showed an increasing velocity near the bottom and a decreasing velocity toward the free surface with a maximum value around the middle of the water depth (figure 2.9b). For this reason it was decided to split the data into two parts for further analysis. To investigate the flow near the bottom of the flume and just below the carpet separately, the measured velocity profiles were divided based on the location of maximum flow velocity. The mean velocity profiles,  $U(y_1)$  and  $U(y_2)$ , were fitted with the logarithmic laws of the wall (Eq. 2.23 and Eq. 2.24) by using their corresponding length scales for each part of the profile, respectively. To characterise the flow near the smooth bottom of the flume, the viscous length scale was used. On the other hand, a roughness length scale was used to normalize the vertical coordinate of Eq. 2.24, considering the carpet as a

hydraulically rough wall.

Equation of the logarithmic profile for a smooth wall reads

$$U_1^+ = \frac{1}{\kappa} \ln y_1^+ + A \quad (2.23)$$

where  $U_1^+ = U/u_{*b}$ ,  $y_1^+ = y_1 u_{*b}/\nu$ ,  $u_{*b}$  = friction velocity at the bottom,  $\kappa$  = Von Kármán constant (= 0.412),  $A$  = integration constant which is a fitting parameter usually found approximately between 3.45 and 5.5.

For the hydraulically rough wall, the equation for the log-law of the wall reads

$$U_2^+ = \frac{1}{\kappa} \ln \frac{y_2 - y_0}{k} + B \quad (2.24)$$

where  $U_2^+ = U/u_{*t}$ ,  $u_{*t}$  = friction velocity at the top,  $y_2$  is vertical direction of the opposite-vertical coordinate system  $xO_2y_2$ ,  $y_0$  is displacement height,  $k$  is roughness height, and  $B$  is an integration constant [53]. It should be noted that analytical determination of  $y_0$  for a rough boundary is an ongoing research in the community of fundamental fluid mechanics [54].

Figure 2.8a and figure 2.8b present velocity profiles that show the development of the boundary layer in the downstream direction, towards the hydraulic structure. In figure 2.8a, the measured velocity profiles were fitted by using Eq. 2.23 and lower coordinate system  $xO_1y_1$ , to characterise the flow at the bottom of the flume. The fitted logarithmic profile (Eq. 2.23) is indicated by the linear black line in the semi-logarithmic plot (figure 2.8a), proving that the lower part of the velocity profiles follows the classical logarithmic law of the smooth wall.

Analysis of the velocity profiles starts with the most upstream section and ends toward the hydraulic structure through the carpet section, to describe the lower and upper parts of the profiles sequentially. At 2.25 m upstream of the hydraulic structure, the complete velocity profile follows the log-law of the wall, except near the free surface (figure 2.8a). This deviation from the logarithmic law at the free surface is not easily explained. As mentioned earlier, the slight deviation of the mean velocity profile is likely affected by the influence of the carpet near the upstream free surface. Detailed investigation of this subtle phenomenon is yet to be carried out in future research.

At the leading edge of the carpet, i.e., 2 m upstream from the hydraulic structure, the velocity profile near the bed shows a logarithmic part although the integration constant is much larger than in the open channel flow cases. The obvious reason is because the flow is abruptly subjected to a change in boundary condition, i.e., a no slip upper boundary. As soon as the velocity

profiles become developed towards the end of the carpet, i.e., 0.25 m and 0.5 m away from the hydraulic structure, the integration constants were found to be  $A = 3.5$  and  $A = 4.8$ , respectively, implying the smooth bottom of the flume. Nevertheless, all the velocities follow logarithmic profiles (Eq. 2.23) near the bottom of the flume. For the velocity profiles underneath the carpet, the

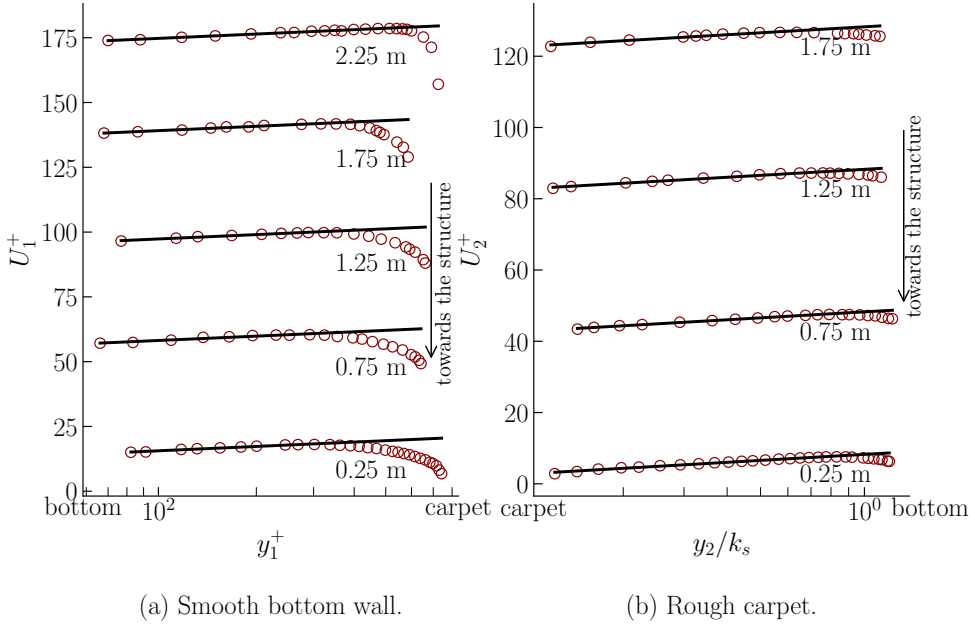


Figure 2.8: Complete velocity profiles in semi-logarithmic scale for Case 1 in Table 2.1. (a) Velocity profiles near the bottom of the flume show a logarithmic profile after scaling with viscous length scale. (b) Velocity profiles beneath the carpet show a logarithmic profile by scaling with roughness length scale. In both plots, the velocity profiles are shifted by  $\Delta U_1^+ = \Delta U_2^+ = 40$  for clear visualization.

upper part of the profile was considered separated by the location of maximum velocity and used the opposite-vertical coordinate system  $xO_2y_2$  to analyse the development of the logarithmic profile.

### Fully developed flow under a stable carpet

This section will assess whether the flow under the carpet attains fully developed condition, or not. For the fully developed flow in a closed or open

channel, total shear stress varies linearly over the water depth according to

$$\frac{\tau_t}{\rho} \equiv -\overline{u'v'} + \nu \frac{\partial U}{\partial y} = u_*^2 \left(1 - \frac{y}{H}\right) \quad (2.25)$$

where  $\tau_t$  is the total shear stress and  $-\overline{\rho u'v'}$  the Reynolds stress [55]. The experimental profiles of the Reynolds stresses changed gradually from the fully developed open channel flow upstream of the carpet (3 m upstream from the hydraulic structure) to the developed closed channel condition at the innermost region of the carpet (0.25 m upstream from the hydraulic structure) in Case 1 (figure 2.9a). This indicates that the flow is transitioning from developed open channel flow to developed closed channel flow through the development of a boundary layer under the carpet. For both developed flows, the Reynolds stress profile showed a linear relation with the water depth, dictated by Eq. 2.25. Between these two locations, the stress profiles depicted a non-linear trend near the upper part of the water depth, typical of the transition region. Figure 2.9b shows the velocity profile and Reynolds shear stress profile measured at 0.25 m upstream of the hydraulic structure, the location with the most developed flow. Data show that the location of zero Reynolds shear stress  $-\overline{\rho u'v'} = 0$  is slightly different from the location of maximum flow velocity  $U_{\max}$ , and is found slightly closer to the smooth wall than the location of  $U_{\max}$ . This is in agreement with experimental observations of [23, 28] who studied asymmetric plane flows between smooth and rough walls.

Even though it was shown in figure 2.8b that the velocity profiles underneath the carpet obey the logarithmic law (Eq. 2.24) qualitatively, the fitting procedure to the measured velocity profile needs to be discussed. One way to obtain  $u_{*t}$  is through fitting the measured velocity data with the log-law of the wall for the inner layer (Eq. 2.24). A second method is via fitting the measured Reynolds stress profile to a linear function (Eq. 2.25), as shown by the straight line in figure 2.9b. Using this linear-fit profile, the friction velocities at the carpet and at the bed can be extrapolated. For consistency, these methods should provide similar values for both friction velocities  $u_{*t}$  and  $u_{*b}$ . After application of an iterative procedure to optimise the fit with Eq. 2.24, a virtual shift  $y_0 = 0.86$  cm and a best-fitting value  $\kappa = 0.35$  are obtained for roughness height  $k = 1$  cm (which is the radius of the sphere). Such a change in  $\kappa$  value was previously reported by Breugem et al. [56] for a flow over a porous surface, which is similar to our case.

Regarding the virtual shift  $y_0 = 0.86$  cm, this was measured from the water surface, or  $y_0 = 0.674$  cm if measured from the bottom of the sphere. Measuring  $y_0$  from the bottom of the sphere in our floating carpet makes

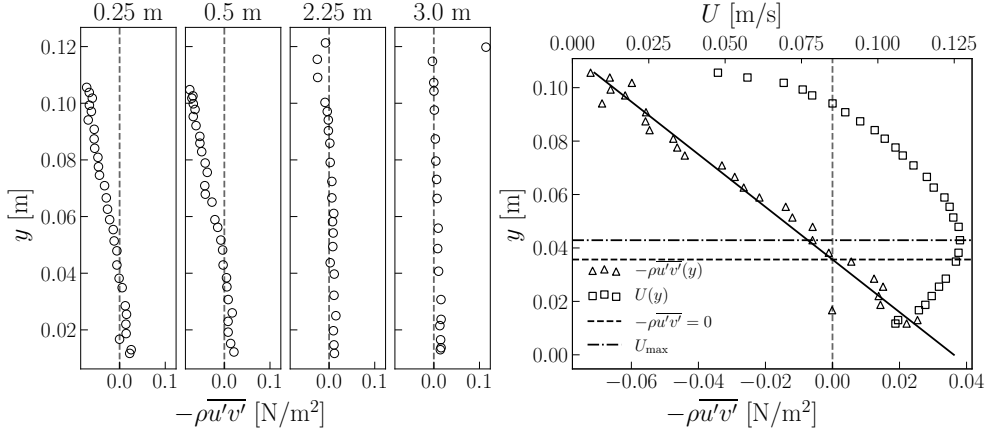


Figure 2.9: Velocity and turbulent properties measured under a 2 m stable carpet. (a) Measured Reynolds stress profiles between 3.0 m and 0.25 m upstream from the structure. (b) Measured velocity and Reynolds stress profiles at 0.25 m location. Position of  $-\overline{\rho u'v'}$  = 0 is slightly closer to the smooth wall than the position of  $U_{\max}$ .

fair comparison of  $y_0/D$  with the literature which measured  $y_0$  from the top of the particle in sediment transport research. In this study, we obtained  $y_0/D = 0.337$ . In the literature, for example, [57, 58, 59], they measured  $y_0$  from the top of the sphere toward the bed, and obtained approximately  $y_0/D = 0.2$  and  $y_0/D = 0.25$ , confirming that our result  $y_0/D = 0.337$  does not deviate much from these values.

The fitting procedure provides the friction velocity at the top  $u_{*t} = 8.6 \times 10^{-3}$  m/s and an integration constant  $B = 8.62$ . The continuous black curve in figure 2.10 shows the resulting best-fitted profile. This best-fitted friction velocity  $u_{*t} = 8.6 \times 10^{-3}$  m/s agrees with the  $u_{*t} = 8.4 \times 10^{-3}$  m/s obtained by fitting the Reynolds stress profile. The latter value is therefore used for the analysis of carpet instabilities.

The velocity profile of the inner layer near the bottom was fitted with the log-law of the smooth wall (Eq. 2.23). The fitted velocity profile is indicated by the black dashed line in figure 2.10. The conventional value of  $\kappa = 0.412$  was used. The friction velocity at the bottom, was found to be  $u_{*b} = 7.38 \times 10^{-3}$  m/s with this method, whilst the method of fitting the Reynolds stress profile provided  $u_{*b} = 6.07 \times 10^{-3}$  m/s. This discrepancy is considered acceptable given the limitations of the experimental approach, especially near the bottom. The value  $u_{*b} = 6.07 \times 10^{-3}$  m/s is used for the analysis of instabilities explained later.

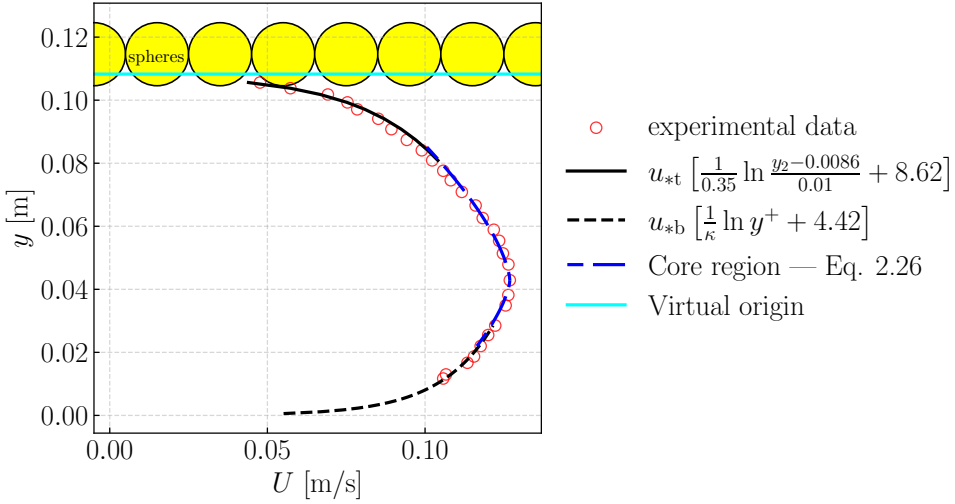


Figure 2.10: Fitting velocity profile with log-laws of the wall. Eq. 2.23 is used for smooth bottom part, and Eq. 2.24 is used for the rough carpet part with  $\kappa = 0.35$ ,  $k = 1$  cm and  $y_0 = 0.86$  cm. The central part of the profile is fitted using power law Eq. 2.26.

The central part of the velocity profile can be approximated by a power law considering each outer layer of the separate profiles as the core region, in line with Nieuwstadt et al. [55]. The power law of the velocity profile reads

$$U_i = U_{\max} - \frac{2 u_{*i}}{3 \beta_i} \left( 1 - \frac{y}{H_i} \right)^{1.5} \quad (2.26)$$

where the index variable  $i$  becomes ‘b’ for the bottom case and ‘t’ for the carpet case,  $\beta$  denotes the experimental parameter ( $\simeq 0.13$ ),  $H_i$  denotes the water depth for each  $i^{\text{th}}$  part up to the location of  $U_{\max}$ . The fitted profiles for each outer part of the velocity profile are shown by the long dashed lines in figure 2.10, providing an excellent agreement with measured data with  $\beta_b = 0.132$  and  $\beta_t = 0.115$ .

### 2.4.3 Analysis of the stability of floating carpets

With the measurements of the flow properties, the squeezing and erosion instabilities of the carpets can now be further investigated using the analytical model developed in “Conceptual Model for Carpet Stability” section. In particular Eq. 2.11 and Eq. 2.19 will be applied. The friction coefficient  $C_f$  needed

for the theoretical model is the squared ratio of friction velocity  $u_*$  and bulk velocity  $U_b$  according to

$$C_f \equiv 2 \left( \frac{u_*}{U_b} \right)^2 \quad (2.27)$$

using the bulk velocity  $U_b$  and the specific friction velocities  $u_*$  as found for the top and bottom, yielding  $C_f^t = 11 \times 10^{-3}$  and  $C_f^b = 6.2 \times 10^{-3}$  using the measured data of Case 1, the fully developed flow under a 2 m carpet.

In order to compare the analytical model with the experimental results for squeezing instability, upper and lower limits of  $U_{b,c}$  were calculated for different carpet lengths. The resulting range of  $U_{b,c}$  is shown in figure 2.11a and figure 2.11c by means of left-slanting hatch for  $d_p = 19.95$  mm and  $d_p = 6.014$  mm, respectively. In these figures, the bulk velocity was normalised with particle's rise velocity  $u_s$ , considering its variability among different particles. Analytical prediction shows good agreement with experimental finding for both cases of  $d_p = 19.95$  mm and  $d_p = 6.014$  mm within the measurement accuracy (figure 2.11a and figure 2.11c), confirming the validity of the theoretical model.

For erosion instability, the force due to turbulent pressure fluctuations  $F'_a$  in Eq. 2.15 was estimated using  $u_*$  obtained in the open channel section of the flume, not affected by the carpet. Fitting the measured Reynolds stress profile provided  $u_* = 4.62 \times 10^{-3}$  m/s and  $C_f = 6.2 \times 10^{-3}$  for the bottom of the flume. As discussed earlier, upper and lower limits of  $U_{b,c}$  can be estimated using the analytical model. The range of resulting  $U_{b,c}$  is shown in figure 2.11b and figure 2.11d with the left-slanting hatch showing variability in particle sizes, respectively. Apparently the analytical model for erosion instability is slightly over-predictive for the case of  $d_p = 19.95$  mm showing that higher flow velocity is required for erosion than the experimental observation (figure 2.11b). However, in case of  $d_p = 6.014$  mm the predicted range of  $U_{b,c}$  lies within the experimental results (figure 2.11d). In both cases, variability of  $u_s$  was also considered when normalising the bulk velocity.

Such a difference in prediction of critical flow velocity for squeezing and erosion can be traced back to (1) imprecise estimation of friction coefficients of the flume, (2) local effect of instantaneous turbulent fluctuations, (3) influence of free surface fluctuations, (4) secondary circulation in the flume as discussed in Appendix 2.B, (5) uncertainties in measurement of the angle of approach flow  $\alpha$  toward the carpet, and (6) variability of the particles. Moreover, the model might not properly consider the effect of the lift force resulting from the streamline curvature around the particle, that causes the particle to be more

unstable. The prediction accuracy could benefit from a more detailed view on the flow around the upstream edge of the carpet, as well as the configuration of the particles inside the carpet. Further experiments are recommended in a longer flume with more space to allow for fully developed conditions both upstream and underneath the carpet.

## 2.5 Conclusions

Understanding the physical processes of plastic waste accumulation in the form of a floating carpet is important to better design waste collection devices and optimise hydraulic structures. This paper investigates the stability of the floating carpet using an analytical model based on physical considerations and laboratory experiments.

Accumulation of plastic particles upstream of hydraulic structures can become unstable via two instability mechanisms: (1) squeezing and (2) erosion. An analytical framework is proposed for these instability mechanisms. Together, the analytical model and experimental data show that squeezing instability of the carpet depends on two dimensionless parameters: (1)  $\lambda/d_p$  which is the number of plastic particles, and (2)  $U_b/u_s$  which is a competition between downward and restoring forces. Erosion instability, however, depends only on the second parameter because the particles at the carpet edge do not experience cumulative compressive force. The carpet's roughness coefficient  $C_f^t$  is necessary to estimate threshold velocity  $U_{b,c}$  of squeezing instability (Eq. 2.11) via estimation of shear stress. The friction coefficient  $C_f^t$  is determined based on the particles' features including their diameter and carpet layout. The bottom friction coefficient of an open channel  $C_f$  and approach angle  $\alpha$  are important parameters to estimate the critical bulk velocity  $U_{b,c}$  of erosion instability (Eq. 2.19).  $C_f$  can be estimated based on the roughness features of the river bed. Determining the approach angle  $\alpha$  requires two-dimensional velocity measurements close to the free surface near the upstream edge of the carpet. Variation of  $u_s$  due to particle's non-uniformity can also change threshold velocity of instabilities.

Moreover, measured velocity data shows that porosity of the carpet reduces Von Kármán constant from 0.412 to 0.35, which changes the slope of velocity profile near the carpet. Therefore, some care is needed to estimate shear stress of the carpet using the conventional logarithmic velocity profile.

2 To elucidate flow structures at the leading edge and near the voids of the carpet, Particle Image Velocimetry (PIV) measurements are recommended that capture spatial high-resolution of the flow. Moreover, compressive force of the carpet should be directly measured using force sensors to compare with indirect estimation of using Reynolds shear stress. Altogether these results provide a better understanding of physical mechanisms of waste accumulation at hydraulic structures. Besides, squeezing and erosion instabilities may be harnessed in certain types of hydraulic structures that extend further in the water to capture a larger amount of debris, avoiding a larger floating surface area in the open channel.

## 2.A Measurement of rise velocity of particles

The rise velocity of the particles were measured using a water column of 2 m length and 15 cm width, as shown in figure 2.12. To release the particle near the base of the water column, the particle was first inserted into the top opening of L-shaped pipe. Particle was pushed down through the pipe using a stick gradually until the particle reached to the bend of pipe. Once the particle passes the bend of the pipe, it exits the pipe instantly and rises due to its buoyancy.

The motion of the particle was recorded using a video camera. To measure the distance travelled by the particle, a ruler was attached on the water column so that the camera records the motion of the particle passed through 30 cm distance as shown in figure 2.12. This 30 cm distance is assumed for the particle to rise with terminal velocity, that is free from initial acceleration. Time taken for this distance,  $\Delta t$ , was also recorded and used to calculate the rise velocity of the particle according to

$$u_s = \frac{0.3 \text{ [m]}}{\Delta t \text{ [s]}}. \quad (2.28)$$

## 2.B Analysis of secondary currents

Existence of secondary currents is assessed and quantified in this appendix for the open channel flow case without particles, and for the 2 m long carpet case. For the latter case, the approach flow angle  $\alpha$  is estimated as well.

Secondary currents can be observed in a turbulent straight channel, especially when the aspect ratio (i.e., flume width/water depth) is smaller than 5, due to anisotropy in the Reynolds stresses [60]. This secondary current induces the downward vertical velocity near the center line of the channel. Such a downward vertical velocity can enhance erosion instability of the particles at the upstream edge of the carpet. The existence of secondary currents was examined in the open channel flow with the hydraulic structure (figure 2.5 without the carpet). figure 2.13 shows the profiles of horizontal and vertical velocities at different measurement locations. The influence of the hydraulic structure is visible even 1.25 m upstream of the structure. The vertical velocity profile at 2.25 m (right in figure 2.13) shows a mean downward vertical velocity of approximately  $0.06U_{\max}$ .

Figure 2.14 shows the profiles of horizontal and vertical velocity along the flume for the 2 m carpet case i.e., Case 1 in Table 2.1. At 3.0 m upstream of the hydraulic structure which is an open channel section (which is 1 m upstream of the carpet), vertical velocity of  $U_y \simeq 0.06U_{\max}$  was also found, implying the influence of secondary currents on the erosion instability even for the case of aspect ratio of 3.3.

To estimate the angle of the approach flow near the upstream edge of the carpet, we applied the following relation to find the velocity angle in the vertical plane as

$$\alpha = \arctan\left(\frac{U_y}{U_x}\right) \quad (2.29)$$

where  $U_y$  and  $U_x$  denotes the vertical and horizontal components of the flow velocity, respectively. Two-dimensional LDV measurements can provide  $U_y$  and  $U_x$  (of the fixed Cartesian coordinate system) along the water depth and consequently angle  $\alpha$  of the velocity vector or streamline can be estimated using Eq. 2.29. Figure 2.14 shows velocity components ( $U_x, U_y$ ) and calculated flow angle  $\alpha$  at 2.00 m upstream of the carpet which is the upstream edge of the 2 m carpet (Case 1 in Table 2.1).

In figure 2.14 the maximum deflection angle is found at the free surface, implying that the streamline bends down near the upstream edge of the carpet. The resulting information can be used in Eq. 2.19 to predict the erosion instability of the particle exposed to the bending streamlines.

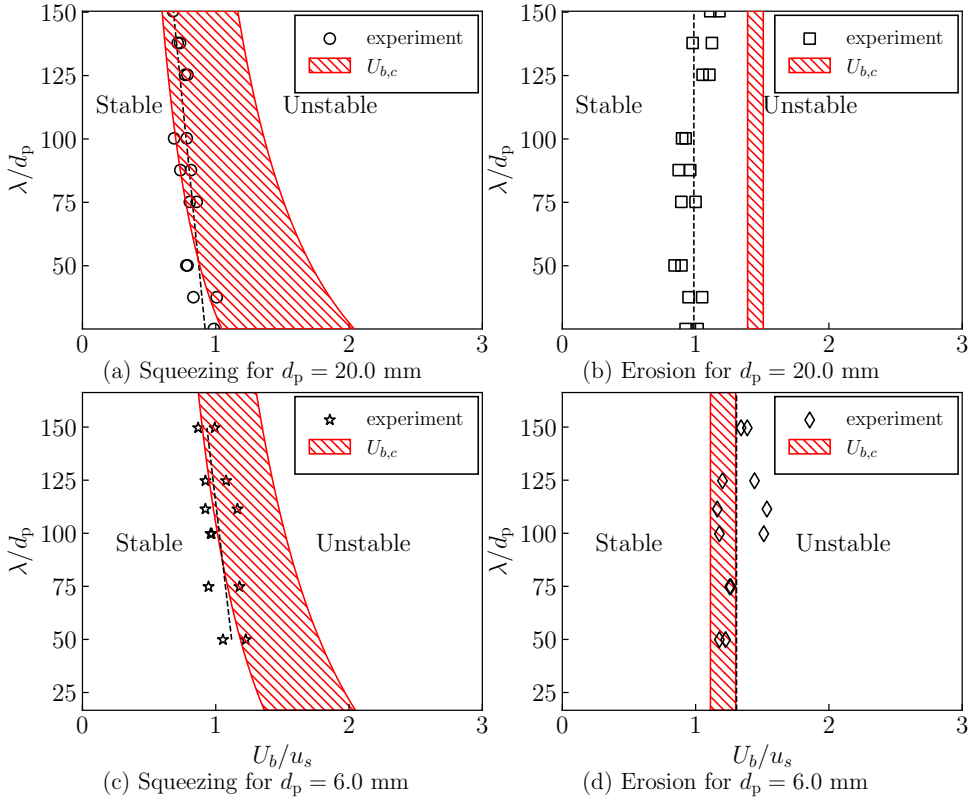


Figure 2.11: Comparison between stability regimes defined by experimental results and analytical model for the particle of (a, b)  $d_p = 19.95$  mm with  $C_f^t = 11 \times 10^{-3}$ , and (c, d)  $d_p = 6.014$  mm with  $C_f^t = 4.59 \times 10^{-3}$ . Hatched regions indicate a range of theoretical predictions of  $U_{b,c}$  for squeezing and erosion.  $U_b$  was normalised by  $u_s \pm$  range, which is the variation of  $u_s$  among the particles.

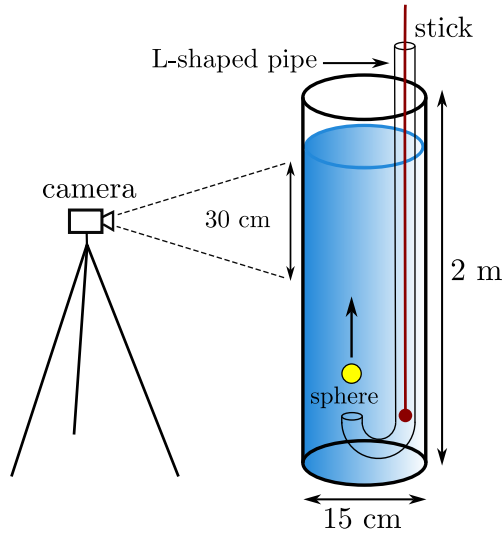


Figure 2.12: Experiment set-up to measure rise velocity of the particles.

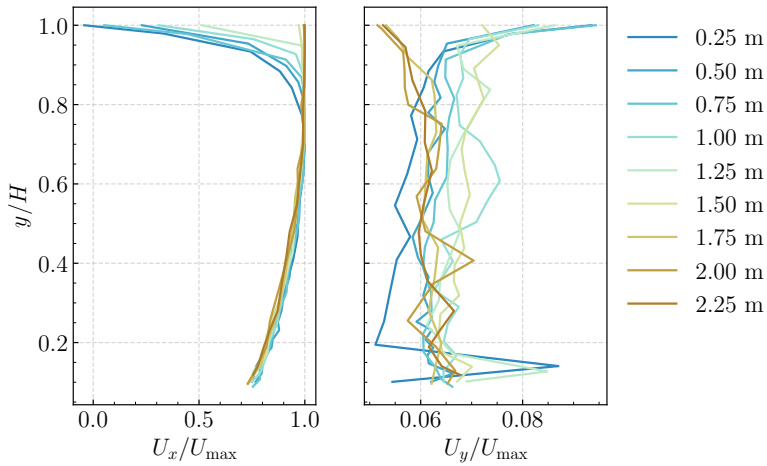


Figure 2.13: Vertical profiles of (left) horizontal and (right) vertical velocity components at different locations in the open channel flow without particles. The location of 0.25 m is the closet location to the hydraulic structure, confirming its influence on the velocity profiles.

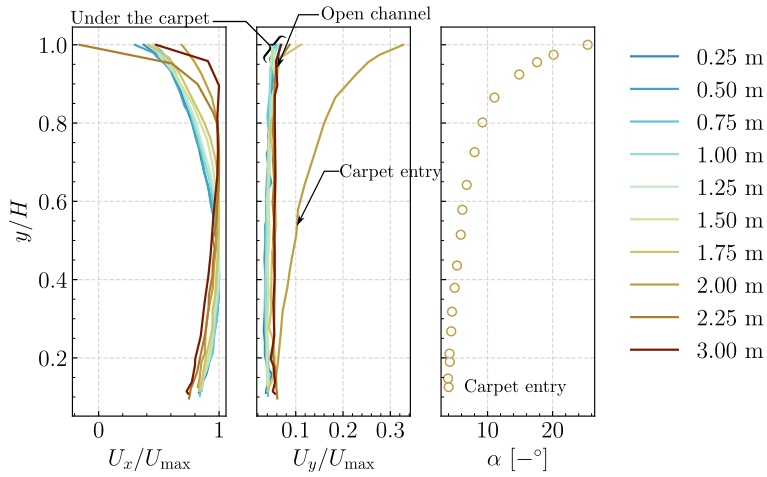


Figure 2.14: Vertical profiles of (left) horizontal and (middle) vertical velocity at the open channel flow, at the carpet entry, and under the 2 m carpet. (right) Flow angle  $\alpha$  along the water column at the carpet entry,  $x = 2.00$  m. The angle represents the deflection of streamlines. The legends in the figure indicate the measurement distance upstream of the hydraulic structure.

# 3

## Numerical Simulation of an Open-to-Closed Channel Transition<sup>◦</sup>

“Life is good for only two things: to do mathematics and to teach it.”

— Siméon Denis Poisson (1781 – 1840)

---

<sup>◦</sup>Published as: **Chit Yan Toe**, Wim Uijttewaal, Baptiste Bardy, Akshay Patil, Pedro Simões Costa, and Davide Wüthrich, *Numerical Analysis of flow and stress redistribution at an open-to-closed channel transition caused by floating debris carpets*, *Journal of Fluid Mechanics* **1027**, A18 (2026). Simulations, analysis and writing are done by Chit Yan Toe, code development by Hardy, Patil and Costa, supervision by Uijttewaal, and Wüthrich. Proofread by everyone.



### 3.1 Introduction

Fluvial systems undergo systematic changes in their hydrodynamic response due to ice-jams, logjams at racks and debris accumulation at waste-collection devices as shown in figure 3.1 (to list a few). In such cases, accumulation of floating materials can induce a transition from free surface flow condition to closed channel-like flow, resulting in complex flow behaviour such as Kelvin–Helmholtz instability [37], and flow separation that depends on the roughness characteristics of the debris at the free surface [37]. Such a change in the boundary condition at the top boundary significantly alters the hydrodynamic response in both the upstream and downstream reaches of the flow domain [61, 62]. Specifically, in the vicinity of the transition, the flow encounters significant changes in the mean velocity profile, shear stress, and acceleration that can lead to increased turbulent transport, erosion at the bottom boundary, and increased instability of the accumulation layer. As a result, understanding the physics of such a flow transition due to the accumulation layer can provide crucial insights to accurately predict its stability and better design hydraulic structures that can efficiently capture floating debris.

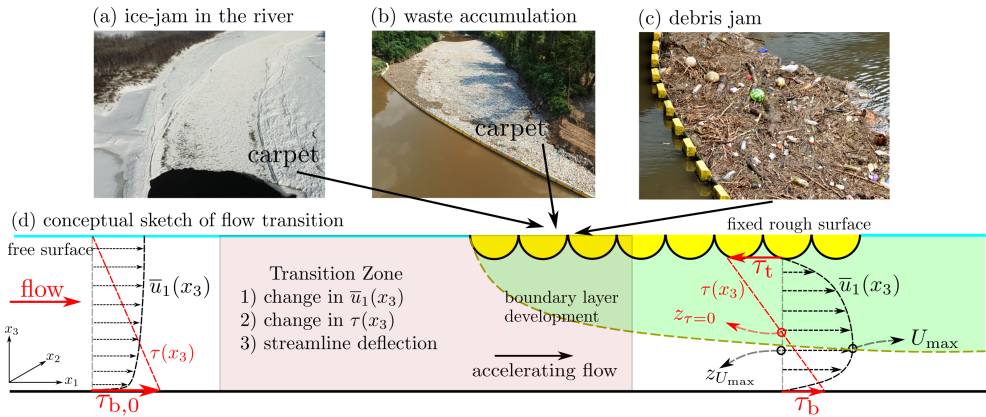


Figure 3.1: Flow transitions from the open channel to the closed channel. (a) Ice-jam in the river (photo: Bryan Hopkins), (b) plastic waste accumulation upstream of waste-collection device (photo: The Ocean Cleanup), (c) debris jam (Copyright Albert Bridge (Image reused under CC Attribution-Sharealike)), and (d) schematic of the flow transition from an open channel to a closed channel (not to scale), based on [63].

Focusing on the formation of a layer of floating material, called *carpet*,

3 its life cycle can be divided into the following stages: (1) initiation of accumulation due to the presence of hydraulic structures, (2) progression due to incoming debris, (3) stabilisation of the carpet, and (4) mechanical breakup or instability due to unbalanced forces. Depending on the type of debris transported by the incoming flow, the carpet formation may consist of one or more layers over the depth of the channel [64, 65, 63]. Additionally, surface roughness characteristics of the carpet can differ greatly from those of the channel bed, leading to an asymmetric shear stress distribution as sketched in the downstream reach of the carpet in figure 3.1. This is typically observed in ice-jams and debris accumulation in the rivers [23, 45, 66]. Moreover, the river morphology is greatly influenced by the surface roughness of the ice-cover, implying that a larger ratio of ice-cover roughness to the bed roughness enhances river bed erosion [66]. Moreover, there is still a debate whether the location of maximum velocity coincides with the location of zero shear stress in the asymmetric channel flows. [28, 24, 23] confirmed through experimental data that the two locations are not identical. In contrast, Shen and Harden [67], Guo et al. [25], Huai et al. [68] assumed these locations to coincide in their analyses, leading to the development of two distinct schools of thought. Thus, the momentum flux across the point of zero mean strain ( $\partial\bar{u}_1/\partial x_3 = 0$ , see figure 3.1) still remains poorly understood for such a hydraulic system. Therefore, the asymmetry in wall roughness conditions imposes further challenges in correctly estimating the friction coefficients of the boundaries of such hydraulic systems, which are also susceptible to destabilising hydrodynamic forces [28, 25, 63].

As for the stability of the carpet, the hydrodynamic forces acting on the debris, and inter-particle forces determine their threshold mobility, and consequently the overall stability of the carpet. For the plastic particles, the hydrodynamic forces affect substantially the global stability of the carpet due to the lack of inter-particle cohesion, thus making them susceptible to various instability mechanisms as detailed in Yan Toe et al. [63]. For the ice-carpet often observed in ice-jams, Beltaos [69], Shen et al. [70], Zufelt and Ettema [71] developed mathematical models to predict the carpet thickness under the static and dynamic flow conditions, assuming a continuum model for ice. Differently from the continuum assumption, Jueyi et al. [45] experimentally investigated incipient motion of individual ice particles under the cover and provided a stability criterion, similar to the Shields criterion used in the sediment transport. Unlike ice-jams, plastic debris does not interact thermally or through mass transfer (i.e., ice melting), but primarily through hydrodynamic

interactions with the carrier phase (i.e., water). Therefore, mechanical properties of the particles and flow conditions are mainly considered in the stability of plastic debris accumulation. Next to the particle transport at the leading edge of the carpet (called *erosion*), particles inside the carpet can be squeezed out vertically due to the cumulative compressive force along the carpet (called *squeezing*), which is similar to the buckling phenomenon observed by Tordesillas and Muthuswamy [18] in the force chains. To that end, Yan Toe et al. [63] developed and validated analytical formulae of these two instability modes, based on the mean flow velocity, particle diameter, and particle density in an idealised single-layer carpet of mono-dispersed spherical plastic particles.

For the squeezing instability, a proper estimate of the cumulative shear stress is required to estimate the destabilising force acting on the particle. Since the flow transitions from an open channel flow to a closed channel with varying hydraulic roughness, estimation of shear stress is non-trivial, especially in the transition region. On this front, Li et al. [36] and Rouhi et al. [33] studied a turbulent boundary layer with roughness transition, and Van Buren et al. [72] studied a turbulent pipe flow with a similar transition, proving that adjustment of turbulent stresses requires a longer downstream fetch than the development length required for the mean flow recovery.

Although there is substantial literature discussing the boundary layer development subject to a rough-smooth transition [35, 72], the hydrodynamics subject to a free-slip (open channel) to no-slip (closed channel) at the top boundary has not been extensively explored. This is particularly interesting as the boundary layers at the smooth bottom and the rough top interact in the downstream fetch of the carpet, leading to a peculiar flow response in the vicinity of the transition. Adding to the complexity, different roughnesses at the top and bottom boundaries further complicate the momentum mixing and consequently it is more challenging to estimate their friction coefficients. These hydrodynamic interactions hinder the prediction of particle instability, irrespective of the material properties of the particle i.e., sediment at the river bed, or plastic particles at the floating carpet. Consequently, in this work, we aim to address the hydrodynamics of an idealised open-to-closed channel transition (figure 3.1), and its implications on the stability of mono-dispersed spherical particles inside a floating carpet.

To this end, three research questions are formulated as follows:

1. How do the shear stresses and the friction coefficients develop along the bottom and top surfaces beyond the carpet transition?
2. What changes in the mean flow are observed near the transition?

3. What are the implications for erosion processes at the bottom boundary, and particle instability of the debris accumulation?

3 By better understanding the boundary layer development at the transition, we aim to further improve the analytical formulations for particle instability, and subsequently better design the waste-collection devices and improve river sediment management. It should be noted that the present study considers only mono-dispersed spherical particles as roughness elements, which differ from realistic debris that is more complex in composition, size, and shape. For example, plastic waste with cylindrical or foil-like shapes is often found mixed with organic materials, complicating the characterization of surface roughness. Similarly, large wood accumulations differ in size and shape from the spherical elements, with their random orientations leading to a complex porosity within the accumulation layer. Therefore, the flow properties and streamlines, particularly the turbulent stresses near and within the accumulation layer, may differ between the simulation results and realistic configurations. Nevertheless, the present DNS study is expected to provide valuable insight about mean flow development and Reynolds stress profiles below a generic carpet of debris, waste or ice, and should serve as a baseline for future studies that would address the complex factors described above.

In the following section, we first present the computational method and various flow configurations to answer the above-mentioned research questions. This is followed by a detailed discussion on the various hydrodynamic parameters of interest in the results and discussions section, and finally, we present the concluding remarks and outline future work to support our analytical model.

## 3.2 Methods

The flow configurations investigated in this work are addressed using Direct Numerical Simulation (DNS) of the Navier-Stokes equations, coupled with a volume penalisation method [73] to represent a rough carpet layer in the computational domain.

### 3.2.1 Governing equations and numerical methods

The differential form of the incompressible Navier-Stokes momentum and mass conservation equations are considered in this work, given by:

$$\frac{\partial u_i}{\partial t} + \frac{\partial u_i u_j}{\partial x_j} = -\frac{1}{\rho} \frac{\partial p}{\partial x_i} + \nu \frac{\partial^2 u_i}{\partial x_j \partial x_j} + F_i + \Pi \delta_{i1}, \quad (3.1a)$$

$$\frac{\partial u_i}{\partial x_i} = 0, \quad (3.1b)$$

where  $t$  is time,  $x_j$  is the coordinate vector,  $u_i$  are the velocity components,  $p$  is pressure,  $\nu$  is the kinematic viscosity,  $\rho$  is the fluid density,  $F_i$  is the penalisation forcing term, added to the momentum transport equation to enforce the no-slip/no-penetration boundary condition on the particle's boundary, and  $\Pi$  is the driving force term used for periodic flow simulations. Kronecker delta  $\delta_{i1}$  indicates the direction of the driving force term. The penalisation forcing term [73] is calculated as

$$F_i = \frac{v_i - u_i}{\Delta t}, \quad (3.2)$$

where  $v_i$  is the velocity imposed at the boundary of the particle (i.e., zero for a stationary object), and  $\Delta t$  is the time step used in the simulation. Here, the index  $i = 1, 2,$  and  $3$  denotes the streamwise, spanwise, and wall-normal directions, respectively, as sketched in figure 3.1.

The governing equations are spatially discretised using a second-order accurate, finite-difference method over a staggered grid, and integrated in time using a third-order accurate, three-step Runge-Kutta method based on the fractional-step algorithm [74, 75, 76]. All the terms in the momentum equation are discretised explicitly and the time-integration is performed such that the Courant–Friedrichs–Lewy (CFL) number does not exceed a value of 0.95. The governing equations are solved using the massively parallel numerical simulation framework CaNS, which has been extensively validated for channel flows at high Reynolds numbers [75]. The computational domain is parallelised using the 2D pencil domain decomposition library developed by [77] and implemented using modern Fortran [78] using the Message-Passing Interface (MPI) for efficient parallel communication over multiple nodes. Additional details on the computational methodology are discussed in [75] and are not repeated here for brevity.

To introduce a floating carpet composed of individual spheres, an MPI-enabled signed-distance-field (SDF) generator is used [79], which is based on a geometry-local distance algorithm. All solid objects introduced within the computational domain are identified by correctly masking the negative SDF values that correspond to the inside of the solid object. As for the initial condition, to guarantee a rapid development of a turbulent boundary layer for the flow transition simulations (figures 3.2(f), 3.2(g) and 3.2(h)), a physical obstacle is placed at the bottom wall to mimic a tripping device traditionally used in experimental facilities. For the simulations with periodic boundary conditions along the streamwise and the spanwise directions, however, a pair of vortices is introduced at the top of the channel that descend downwards to induce turbulence [80, 81]. A no-slip condition is enforced at the bottom boundary and the top (smooth and rough) boundary, and a free-slip condition is imposed for the free surface assuming as the rigid-lid assumption. All data is averaged in time and along the homogeneous directions, respectively, after an initial spin-up time of 10 eddy-turn-overs ( $T_\epsilon \equiv H/u_{*b}$  where  $H$  is the channel height and  $u_{*b}$  is the friction velocity at the smooth bottom boundary) and the results are averaged over a total of  $15T_\epsilon$ .

In this work, the flow quantity  $\theta$  is decomposed as,

$$\theta(x_i, t) = \bar{\theta}(x_i) + \theta'(x_i, t) = \langle \bar{\theta} \rangle(x_3) + \tilde{\theta}(x_i) + \theta'(x_i, t) \quad (3.3)$$

where  $\bar{\theta}$  denotes the time-averaged quantity,  $\theta'$  the temporal (turbulent) fluctuation,  $\langle \bar{\theta} \rangle$  the time- and plane-averaged quantity,  $\tilde{\theta}$  the dispersive or spatial deviations when compared to the time-averaged quantity  $\bar{\theta}$ . For cases where the streamwise and spanwise directions are homogeneous, a periodic boundary condition is applied along these directions (i.e.,  $x_1$  and  $x_2$ ), thus allowing for the (intrinsic) plane-averaging to be performed over these two coordinate directions. For cases where a flow transition is considered, the streamwise direction  $x_1$  is no longer considered homogeneous, and the plane-average is performed only over the spanwise direction  $x_2$ . However, in the streamwise direction the spatial averaging is performed over a diameter of the spheres in such cases, although the same notation  $\langle \theta \rangle$  is used. Detailed explanation of the different simulation scenarios is presented in Sec. 3.2.2 and figure 3.2.

The total force acting on the particles is extracted by integrating the penalisation forcing term over the volume of the roughness layer. The force is in turn used to determine the friction velocity at the rough layer  $u_{*t}$  via  $u_{*t} = \sqrt{\langle \bar{\tau}_t \rangle} / \rho$  [82, 33], where  $\langle \bar{\tau}_t \rangle$  is the time- and space-averaged wall shear stress. Alternatively, the wall shear stress can be obtained from the extrapolation of

the linear shear stress profile to the bed, though this approach is not applicable to flow transition cases where the fully developed flow is not realized yet. Therefore, in such cases the shear stress  $\langle \bar{\tau}_t \rangle$  acting on each row of particles within the carpet (denoted as  $l^{\text{th}}$  row for  $l = 1, 2, 3, \dots$  in figures 3.2(g) and 3.2(h)) is calculated by dividing the horizontal component of the averaged penalisation force  $\langle \bar{F}_1 \rangle_l$  acting on that row by the projected area, i.e., the product of the channel width  $B$  and sphere's diameter  $d_p$ .

### 3.2.2 Simulation scenarios

To investigate the hydrodynamics of floating carpets under various flow conditions, we consider eight flow configurations as detailed in table 3.1 and illustrated in figure 3.2. The first five cases are described as (a) case CS: closed channel flow with both smooth bottom and top boundaries, (b) case OS: open channel flow with a smooth bottom boundary and free surface at the top, (c) case OR: open channel flow with a rough bottom boundary and free surface at the top, (d) case CR2 and (e) case CR3: closed channel with a rough top boundary and a smooth bottom boundary. Case CR2 has a relative roughness given by  $d_p/H = 1/6$ , and case CR3 has  $d_p/H = 1/4$ . The aforementioned five cases are intended as the benchmark cases, while case OR is considered to validate the volume penalisation methodology implemented for this study. Case OR corresponds to the F50 configuration in Chan-Braun et al. [83]. As presented in Appendix 3.A, the comparison between the methodology used in this work and the results in Chan-Braun et al. [83] shows a good agreement, thus validating the current numerical framework. The details about the validation procedure can be consulted in Appendix 3.A. As for cases CS, OS, CR2, and CR3, flow conditions and geometry parameters are identical to the laboratory experiments from [63]. In the cases CS, OS, CR2, and CR3, a constant pressure gradient drives the flow such that the bulk Reynolds number  $Re_{bH} = 13080$  is achieved, where  $Re_{bH} = \frac{U_{bH}H}{\nu}$ ,  $U_{bH} = \frac{1}{H} \int_0^H \langle \bar{u}_1 \rangle dx_3$  is the bulk velocity based on  $H$ .

To examine the impact of the transition, three main simulations are considered in this work, namely case TS, case TR2, and case TR3 and illustrated in figures 3.2(f), 3.2(g), and 3.2(h), respectively. Case TS is the case with a transition from the smooth open channel to the smooth closed channel. Case TR2 denotes the scenario with a transition from a smooth open channel to a closed channel with a rough top boundary characterized by relatively small

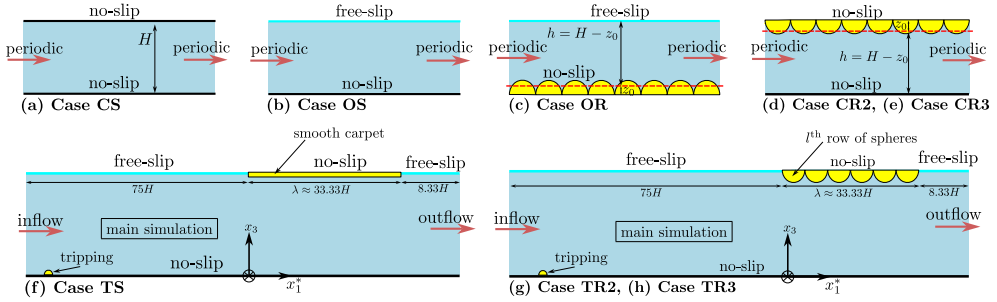


Figure 3.2: Various simulation scenarios considered in this work. Panels (a,b,c,d,e) employ periodic boundary conditions with a constant bulk velocity  $U_{bH}$ , while panels (f,g) use use inflow/outflow conditions with a tripping mechanism for a rapid development of the turbulent boundary layer. Panels (a,b,d,e) are used as auxiliary simulations that are used to compare the flow development of the cases in panels (f,g,h). The latter three simulations consider the flow transition from the free-slip to no-slip condition at the top boundary. In further analysis of transition cases TS, TR2 and TR3,  $x_1^* = x_1 - 75H$  coordinate is used for streamwise direction as shown in panels (f,g,h).

roughness ( $d_p/H = 1/6$ ). Case TR3 considers a similar flow configuration as case TR2 with relatively larger roughness ( $d_p/H = 1/4$ ). In these transition cases TS, TR2, and TR3, a uniform velocity profile is prescribed at the inlet boundary, and the flow develops toward a turbulent boundary layer due to the tripping placed at the bottom wall (see figures 3.2(f), 3.2(g) and 3.2(h)). The tripping used in this study consists of a line of hemispheres of diameter  $d_p = 0.01$  ( $d_p/H \approx 0.08$ ) placed at  $x_1 = 0.10$  m downstream of the inlet plane. The floating carpet is placed at  $x_1/H = 75$  distance away from the inlet boundary to allow a sufficiently long fetch for a fully developed condition. The length of the floating carpet layer  $\lambda$  is set to  $\lambda/H = 100/3$ . At the outlet boundary of the flow domain, a Neumann velocity boundary condition is prescribed, while the pressure at the outlet boundary is set to  $p = 0$ . It is noted that the current method of imposing a Neumann boundary condition on the streamwise velocity component, combined with the prescribed inflow, naturally imposes the net pressure difference that sustains the flow in this spatially developing channel as in the experiments, whereas this particular combination is not suitable for simulations of zero pressure gradient turbulent boundary layer.

For all rough channel cases CR2, CR3, TR2, and TR3, the roughness height  $k$  is defined as the radius of the individual spherical particles ( $0.5d_p$ ) of the floating carpet as assumed by [84]. Therefore, the relative roughness for cases CR2 and TR2 is  $k/H = 0.0833$ , and for cases CR3 and TR3 is

Table 3.1: Numerical simulations corresponding to the illustrations in figure 3.2. For cases CR2 and CR3, the parameters are normalised by the friction velocity at the smooth bottom boundary  $u_{*b}$  specific to each case. For cases TR2 and TR3, however, the mesh parameters are normalised by  $u_{*b}$  from cases CR2 and CR3, respectively. In case TS, the flow parameters are normalised by  $u_{*b}$  from case CR2.

Case	Description	$L/H$	$d_p/H$	$k_{s\infty}/H$	$Re_{bH}$	$Re_{\tau b}$	$Re_{\tau t}$	$\Delta x^+$	$\Delta y^+$	$\Delta z^+$
CS	Closed channel with smooth walls	16.6	—	—	13080	375.83	376.73	12.5	4.18	0.21 → 7.44
OS	Open channel with smooth walls	16.6	—	—	13080	689.51	—	11.5	3.83	0.19 → 6.82
OR	Open channel with rough walls	12.0	0.178	0.113	2880	241.03	—	0.94	0.94	0.94 → 0.96
CR2	Closed channel with small roughness	15.0	0.167	0.036	13080	312.49	701.50	7.00	3.50	0.76 → 4.34
CR3	Closed channel with large roughness	15.0	0.250	0.064	13080	305.73	788.48	7.34	3.58	0.79 → 4.38
TS	Flow transition to smooth top	116.67	—	—	13080	—	—	10.5	7.00	0.76 → 4.34
TR2	Flow transition to small roughness top	116.67	0.167	0.036	13080	—	—	10.5	7.00	0.76 → 4.34
TR3	Flow transition to large roughness top	116.67	0.250	0.064	13080	—	—	11.0	7.15	0.61 → 4.77

$k/H = 0.125$ , respectively. While the roughness height is known a priori, the equivalent sand grain roughness for large Reynolds number  $k_{s\infty}$  and the virtual origin  $z_0$  [85] are derived in Appendix 3.B. For some of the cases listed in table 3.1, the location of the maximum streamwise velocity ( $U_{\max}$ ) is a length scale of interest and therefore, a friction Reynolds number at the bottom boundary is defined as  $Re_{\tau_b} = u_{*b}z_m/\nu$  where  $z_m$  is the location of  $U_{\max}$  normal to the wall, and the friction Reynolds number at the rough top boundary as  $Re_{\tau_t} = u_{*t}(H - z_m)/\nu$ , respectively. In all rough channel simulations, the spheres are placed in a regular uniform arrangement.

### 3.3 Results and Discussions

#### 3.3.1 Streamwise development of global quantities

To analyse the fully developed flow condition as a function of the streamwise distance from the inflow boundary, we discuss the development of the time- and plane-averaged flow parameters i.e., mean velocity and Reynolds shear stress, for cases TR2 and TR3. These quantities are compared with the results from cases CS, OS, CR2 and CR3 that serve as benchmark datasets.

Figure 3.3 compares the development of time- and plane-averaged velocity profiles along the streamwise direction of the channel for cases TS, TR2 and TR3. Here the streamwise coordinate origin is set at the start of the floating carpet such that the negative values for the streamwise direction  $(x_1 - 75H)/H < 0$  corresponds to the flow domain upstream of the carpet, while the positive values for the streamwise direction  $(x_1 - 75H)/H > 0$  the downstream reach of the carpet, respectively. Hereafter,  $(x_1 - 75H)/H$  will be referred to as  $x_1^*/H$  where  $x_1^* = x_1 - 75H$ , denoted by the colourbars in figure 3.3. The time- and plane-averaged streamwise velocity profile  $\langle \bar{u}_1 \rangle(x_3)$  upstream of the transition in cases TS, TR2 and TR3 is observed to compare well with the profile obtained for the statistically stationary flow of case OS within 2% range of accuracy (figure 3.3(a)). At the transition point  $x_1^*/H = 0$  and downstream locations  $x_1^*/H > 0$  as shown in figures 3.3(b), 3.3(c) and 3.3(d), the flow encounters a floating carpet and thus undergoes an adaptation to the no-slip boundary condition. In case TS, the velocity profiles do not reach the fully developed velocity profile when compared to the benchmark

profile of case CS (figure 3.3(b)). In contrast, case TR2 (figure 3.3(c)) and case TR3 (figure 3.3(d)) exhibit a fully developed flow condition at  $x_1^*/H \approx 33$ . The benchmark results from cases CS, CR2 and CR3 are also shown in figures 3.3(b), 3.3(c) and 3.3(d), respectively.

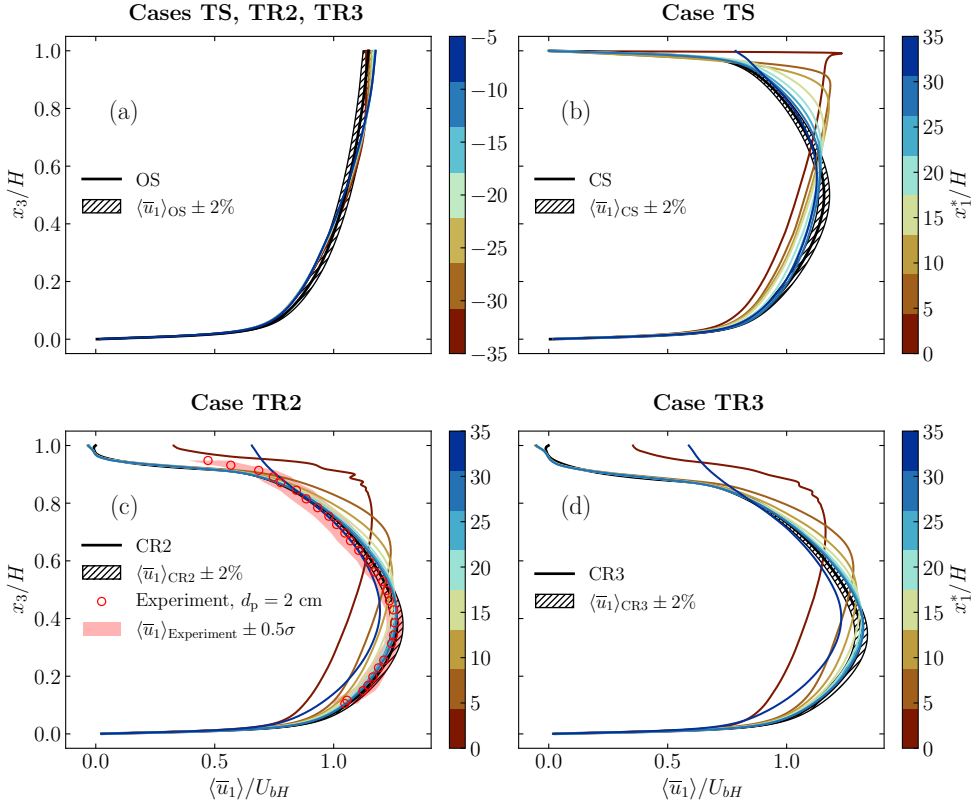


Figure 3.3: Mean velocity profiles (a) upstream of the transition for all transition cases, and (b,c,d) downstream of the transition for case TS, case TR2 and case TR3, respectively. The hatched area on each panel indicates  $\pm 2\%$  of velocity profiles of case OS, case CS, case CR2 and case CR3, respectively. The colourbars mark the positions of the mean velocity profiles along the streamwise direction of the channel with respect to the location of the transition. The red shading in panel (b) marks the  $\pm \sigma/2$  around the experimental data of Yan Toe et al. [63] ( $\sigma$  is the standard deviation). The colorbars indicate the streamwise position with respect to the transition point.

To investigate the flow behaviour in the near wall region, the above-mentioned velocity profiles are plotted again using the viscous length scale or wall unit in figure 3.4. In all subfigures, the velocity profiles are shifted by

$\Delta U^+ = 5$  for clear visualization. Figure 3.4(a) shows the evolution of the flow immediately downstream of the tripping mechanism, and the logarithmic profile is recovered at  $x_1^*/H = -40$ . The development of flow profiles upstream of the transition point is depicted in figure 3.4(b), showing that the approach flow to the carpet compared well against the logarithmic mean velocity profile. To study the velocity profiles in the closed channel region of cases TS and TR2, the profiles are divided based on the location of maximum streamwise velocity, and shown separately in figures 3.4(c), 3.4(d), 3.4(e), and 3.4(f). For the rough channel case TR2, the velocity profiles in the top part need to be shifted for their virtual origins where the logarithmic velocity profile begins, which are more elaborated in Appendix 3.B, in figure 3.4(f). The velocity profiles in all cases are observed to recover at  $x_1^*/H = 30$  and agree with benchmark results. Since the velocity profiles of case TR3 show similar shape as those of case TR2, the results of case TR3 are omitted here.

A rapid recovery of first-order statistics i.e., mean streamwise velocity is observed in the rough transition cases TR2 and TR3 due to the additional momentum mixing induced by the spheres of the rough carpet. However, in the smooth transition case TS, the first-order statistics cannot be recovered immediately downstream of the transition. Moreover, the simulation results of cases CR2 and TR2 show a good comparison with the experimental result from Yan Toe et al. [63] in the fully developed condition, except for a slight deviation near the top rough wall (figure 3.3(c)). It should be noted that the laboratory experiments used spheres with a slightly higher submergence of 87%.

The streamwise evolution of the Reynolds shear stress profile for case TR2 is compared against the benchmark case OS and case CR2 in figures 3.5(a) and 3.5(b), respectively. Upstream of the transition, the Reynolds stress profiles for case TR2 and case OS are observed to be in good agreement (figure 3.5(a)), whereas the profiles under the carpet in figure 3.5(b) fail to recover to the linear stress profile observed for the benchmark case CR2. It is noted that at  $x_1^*/H \approx -1$  which is very close to the transition point, the flow already experiences the step change and consequently the profile near the bottom boundary does not agree exactly with the benchmark velocity profile of case OS (figure 3.5(a)). Similarly, since the streamwise position  $x_1^*/H \approx 36$  represents the location downstream of the end of the carpet, the flow transitions again to the open channel flow (denoted as free-slip boundary condition in figure 3.2(g)) and the stress profile is found to deviate from the benchmark case CR2 in figure 3.5(b). The relatively slow response of the Reynolds stress under the

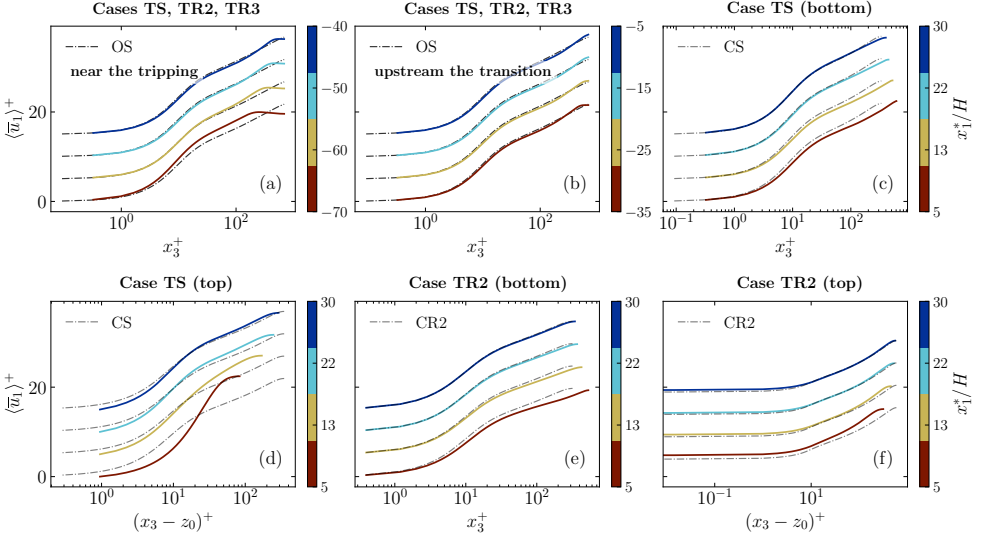


Figure 3.4: Comparison of mean velocity profiles normalized by inner scaling: (a) comparison in the vicinity of the physical tripping, (b) comparison upstream of the transition, (c) comparison in the lower half of the channel for case TS, (d) comparison for the upper half of the channel where the debris accumulates, (e) comparison for the bottom half of the channel for case TR2 after the transition, and (f) comparison for the upper half of the channel for case TR2 after the transition. In cases TS and TR2, the velocity profiles under the carpet are divided based on the location of the maximum streamwise velocity  $z_m$ . Since velocity profiles of case TR3 do not show any significant difference from those of case TR2, results of case TR3 are omitted. Dash-dotted line denotes the velocity profile of reference cases (OS, CS, and CR2), while solid lines denote for transition cases (TS, TR2, and TR3).

carpet follows the previously observed trends by [72] and [33]. A similar trend was seen for case TR3, which is not shown here for brevity. There are, however, some minor differences observed closer to the bottom wall when comparing the numerical and the experimental results, which can be presumably attributed to the experimental measurement limitations and additional side wall effects of the flume. Overall, both the time- and plane-averaged mean flow response and the Reynolds stress profile compare well with the benchmark cases, suggesting that the approach flow conditions upstream of the transition are fully developed in cases TS, TR2 and TR3. Moreover, larger shear stresses are observed near the rough top boundary compared to those near the bottom boundary downstream of the transition point because of roughness-induced turbulence stresses. It is noted that variations in debris size and shape can lead to different observations of the stress distribution.

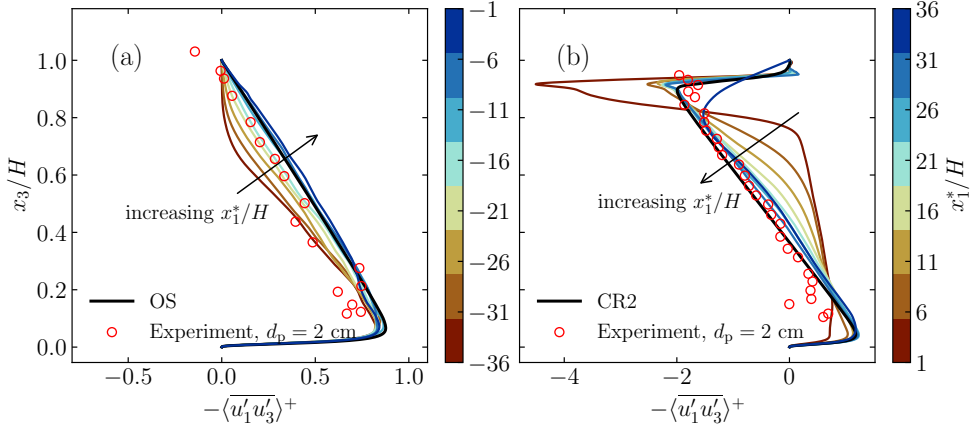


Figure 3.5: Reynolds shear stress profiles for case TR2: (a) upstream of the flow transition, and (b) downstream of the transition. The colourbars mark the positions of the Reynolds shear stress profiles along the streamwise direction of the channel with respect to the location of the transition. Since the streamwise position  $x_1^*/H \approx 36$  is beyond the end of the carpet and the flow transitions to open channel flow again (figure 3.2(g)), the stress profile does not follow the benchmark profile.

Streamwise development of turbulent normal stresses  $\langle \overline{u'_i u'_i} \rangle$  is also investigated using inner-scaling and outer-scaling in figures 3.6(a,b,c) and 3.6(d,e,f), respectively, for case TR2. The profiles are found to approach the benchmark results gradually as expected. As reported by [86], the normal stress profiles also show an asymmetric shape in the rough-smooth closed channel due to the different roughnesses. Detailed study of turbulent normal stresses is presented in Appendix 3.C for cases TS and TR3, including the development of the profiles at the inflow section, downstream of the tripping point.

To study the impact of the floating carpet on the bulk flow, we consider three different metrics that quantify the boundary layer development, viz., the displacement thickness ( $\delta_*^t$ ) given by

$$\delta_*^t = \int_0^{z_m} \left( 1 - \frac{\langle \overline{u_1} \rangle}{U_{\max}} \right) dx_3, \quad (3.4)$$

the momentum thickness ( $\Theta^t$ ) given by

$$\Theta^t = \int_0^{z_m} \frac{\langle \overline{u_1} \rangle}{U_{\max}} \left( 1 - \frac{\langle \overline{u_1} \rangle}{U_{\max}} \right) dx_3, \quad (3.5)$$

and the top boundary layer ( $\delta^t \equiv z_m$ ) defined as the distance from the wall

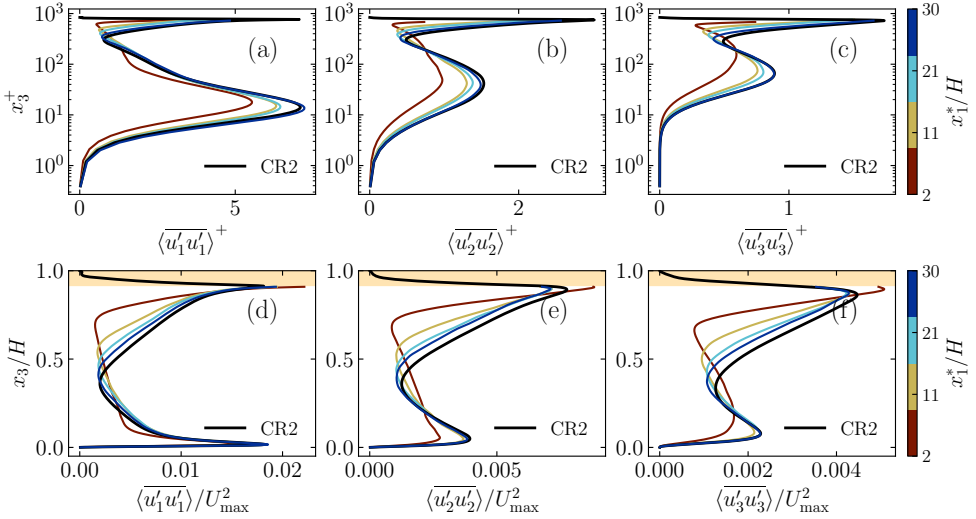


Figure 3.6: Vertical profiles of turbulent normal stresses  $\langle \overline{u_i' u_i'} \rangle$  downstream of the transition point  $x_1^*/H > 0$ : (a,b,c) using inner scaling, and (d,e,f) using outer scaling. Orange-coloured area in figures 3.6(d,e,f) indicate the height of the roughness.

where the streamwise velocity has a maximum value ( $U_{\max}$ ). Figure 3.7 compares the above-mentioned metrics for the boundary layer growth under the floating carpet for cases TS, TR2 and TR3. As the flow approaches the floating carpet, the mean flow is observed to experience the effect of the carpet even in the upstream region as indicated by  $\delta^t$  (figures 3.7(a) , 3.7(c) and 3.7(e)). A more pronounced effect is observed in the case of the rough carpet (figures 3.7(c) and 3.7(e)), whereas a smaller effect is seen in the smooth transition case TS (figure 3.7(a)). Subsequently, the mean flow deflects with a vertically downward flow as shown in figure 3.17. For case TR2, the top boundary layer (red dashed-dot line in figure 3.7(d)) extends from the top wall to the vertical position of  $(H - \delta^t)/H \approx 0.4$  and asymptotes to a constant value along the streamwise direction at  $x_1^*/H \geq 30$ , suggesting a fully developed flow condition underneath the carpet. The momentum thickness  $\Theta^t$  and the displacement thickness  $\delta_*^t$  are observed to be relatively smaller compared to  $\delta^t$  as expected. Comparing the boundary layer growths across the cases TS, TR2, and TR3, the relatively larger roughness height in case TR3 induces a larger boundary layer thickness (figure 3.7(f)), while a smaller boundary layer is observed in the smooth carpet case TS (figure 3.7(b)) for all the metrics discussed above. This is especially true when comparing the asymptotic be-

haviour where case TR2 is observed to attain a value of  $(H - \delta^t)/H \approx 0.4$ , while case TS attains a smaller value of  $(H - \delta^t)/H \approx 0.6$  and case TR3 attains a slightly larger value of  $(H - \delta^t)/H < 0.4$  (here smaller values mean deeper top boundary layer), thus, clearly illustrating the impact of the relative roughness height.

We also quantify the relative development of  $\delta^t$  with respect to the asymptotic value  $\delta_\infty^t$  that is obtained from the corresponding benchmark cases, giving the ratio  $\|\delta^t - \delta_\infty^t\|/\delta_\infty^t$  as shown in figure 3.8. All cases TS, TR2 and TR3 exhibit a similar relative growth of  $\delta^t$  although the shape of case TS differs slightly from that of cases TR2 and TR3, which share an identical shape. Therefore, different roughness heights do not affect the relative growth rate of the boundary layer,  $\|\delta^t - \delta_\infty^t\|/\delta_\infty^t$ .

Similar to a conventional smooth boundary layer, the displacement thickness  $\delta^{*t}$  and the momentum thickness  $\Theta^t$  are smaller than the boundary layer thickness  $\delta^t$  in all transition cases TS, TR2 and TR3. At the location of the fully developed flow in case TR2, their ratios are found to be  $\delta^t/\delta_*^t = 3.8$  and  $\delta^t/\Theta^t = 9.6$ , respectively. The momentum thickness is observed within the roughness layer (figure 3.7(d)), meaning that the loss of momentum in the rough boundary layer occurs mostly inside the roughness elements. In case TR3, the thicknesses of the aforementioned three layers ( $\delta^t$ ,  $\delta_*^t$  and  $\Theta^t$ ) are found larger than those in case TR2 because the larger roughness push the mass and momentum mixing layers further away. Nevertheless, the ratios  $\delta^t/\delta_*^t = 3.3$  and  $\delta^t/\Theta^t = 9.8$  are found in case TR3, which are approximately similar to those observed in case TR2.

In addition to the study of boundary layer thickness, we examined the internal boundary layer (IBL)  $\delta_{\text{IBL}}$  and internal equilibrium layer (IEL)  $\delta_{\text{IEL}}$  which show the immediate response of the flow to the changes in the boundary roughness. The layer to which the effect of the new boundary roughness reaches is defined as IBL, and the lower part of IBL which obtains a new equilibrium with the new surface is called IEL [33]. Previous work of Rouhi et al. [33] is referred for detailed explanation and calculation method of  $\delta_{\text{IBL}}$  that we apply here. In brief, the slope curve  $dU^+/d \ln x_3^+$  is plotted for each  $x_1$  position as shown in figure 3.9, and two successive local extrema of the slope curve are identified. Then, two linear fits are applied to the velocity profile in the semi-log scale corresponding to these extrema, and the intersection point of the two fitted lines is determined. This intersection defines the position of  $\delta_{\text{IBL}}$ .  $\delta_{\text{IEL}}$  is obtained by locating the vertical position corresponding to the *first* logarithmic region in a composite velocity profile consisting of several

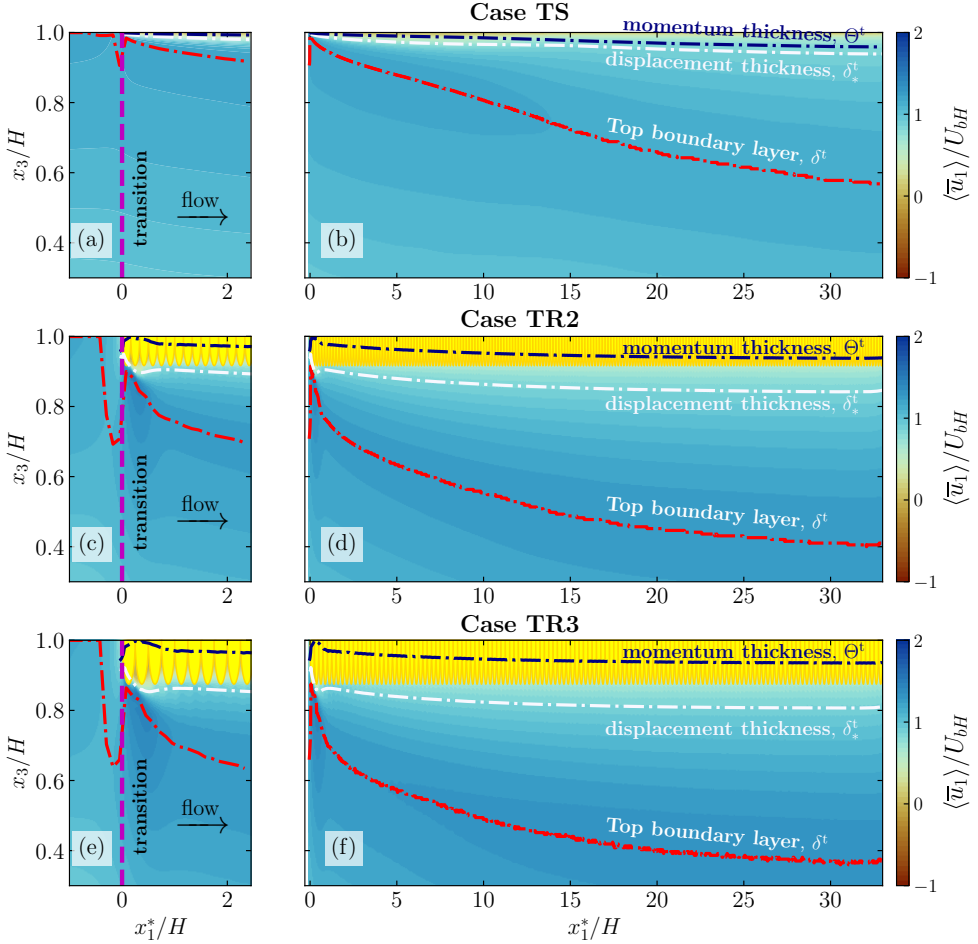


Figure 3.7: Development of top boundary layer  $\delta^t$ , displacement thickness  $\delta_*^t$ , and momentum thickness  $\Theta^t$ : (a,c,e) near the transition (zoom-in view for the horizontal dimension) and (b,d,f) under the carpet for case TS, case TR2 and case TR3, respectively. Yellow regions on all panels represent the floating carpet (not to scale).

individual profiles [87]. Figure 3.9 shows  $\delta_{IBL}$  and  $\delta_{IEL}$  at the rough top surface for case TR2 and case TR3. Both internal layers ( $\delta_{IBL}$  and  $\delta_{IEL}$ ) are found to be almost identical, and inside the external top boundary layer  $\delta^t$  of the rough surface as observed in the work of Rouhi et al. [33]. Some noise is observed in case TR2 which may be attributed to the sensitivity of the slope finding method. The green line in figure 3.9 denotes a power-law fitted line,

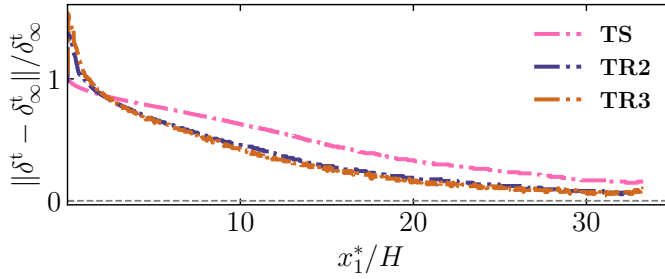


Figure 3.8: Relative development of top boundary layer  $\delta^t$  with respect to its asymptotic value  $\delta_\infty^t$ . The asymptotic value is obtained from the corresponding periodic benchmark cases.

$\delta_{\text{IBL}} \propto (x_1^*)^\alpha$  as suggested by Li et al. [88], for  $\delta_{\text{IBL}}$  to estimate its growth rate, and it is found that  $\delta_{\text{IBL}}$  varies as  $(x_1^*)^{0.67}$  in case TR2 and varies with  $(x_1^*)^{0.38}$  in case TR3. The observed  $\alpha$  values lie within 0.22 and 0.886 as reported by Rouhi et al. [33]. It should be noted that previous studies on step changes [35, 36, 33] did not consider the influence of the bottom boundary, but here the presence of the smooth bottom boundary is incorporated in the DNS study of rough boundary layer development, creating a closed and asymmetric flow geometry.

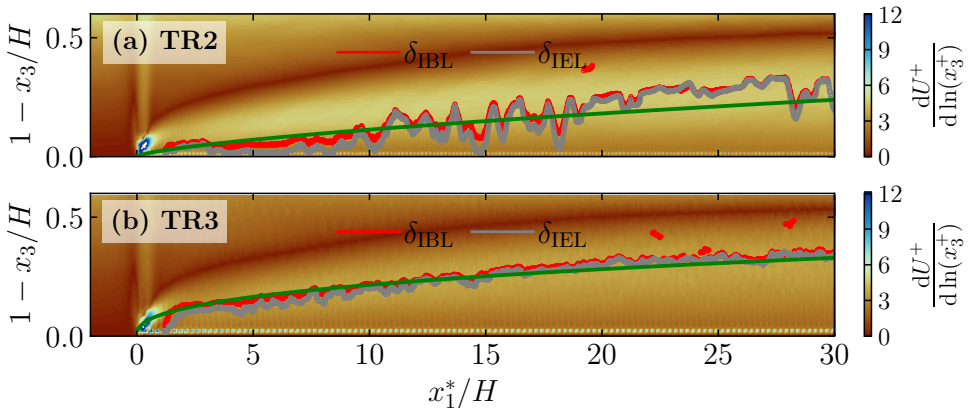


Figure 3.9: Internal boundary layer  $\delta_{\text{IBL}}$  and internal equilibrium layer  $\delta_{\text{IEL}}$  at the top rough surface for (a) case TR2 and (b) case TR3. The vertical coordinate in the figures is the inverted coordinate such that  $1 - x_3/H = 0$  is the top surface. The green line is a power-law fit.

Time- and spanwise-averaged momentum balance in the streamwise direction is assessed for case TR2 in figure 3.10 and for case TR3 in figure 3.11. The streamwise momentum equation for the developing flow condition can be expressed as

$$\frac{d}{dx_1} \int_0^H \langle \overline{u_1^2} \rangle dx_3 = -\frac{1}{\rho} \frac{d\langle \overline{p} \rangle}{dx_1} H + \frac{\tau_t}{\rho} - \frac{\tau_b}{\rho} + \nu \frac{d^2}{dx_1^2} \int_0^H \langle \overline{u_1} \rangle dx_3 \quad (3.6)$$

where the LHS term is the advective acceleration term, the first term in RHS is the pressure gradient, and the last term is streamwise gradient of the diffusive force. For the fully developed flow, the force balance equation reads after simplification

$$\frac{d\langle \overline{p} \rangle}{dx_1} H = \tau_t - \tau_b \quad (3.7)$$

implying that the pressure drop (LHS) is balanced by the sum of the wall shear stresses (RHS) at the top and the bottom walls of the closed channel region. Here,  $\tau_t$  is the stress at the top boundary, and  $\tau_b$  is the stress at the bottom boundary where only the viscous stress is present, respectively. For the open channel flow upstream of the carpet i.e.,  $x_1^*/H < 0$ , the driving pressure gradient  $d\langle \overline{p} \rangle/dx_1$  is balanced by the shear stress only at the bottom wall  $\tau_b$  as shown in figure 3.10(b). In the vicinity of the transition, the momentum balance Eq. 3.7 is not valid since the flow is developing toward the new equilibrium. In this region, the local acceleration term  $\frac{d}{dx_1} \int_0^H \langle \overline{u_1^2} \rangle dx_3$  also plays an important role to balance with the pressure gradient force. Afterwards, the flow approaches the fully developed condition at  $x_1^*/H \approx 30$  where the total wall shear stress ( $\tau_t - \tau_b$ ) is equal to the pressure gradient force. The acceleration term vanishes in the fully developed flow region as expected, and the contribution of the streamwise diffusive term  $\nu \frac{d^2}{dx_1^2} \int_0^H \langle \overline{u_1} \rangle dx_3$  is found to be insignificant (figures 3.10 and 3.11). A similar stress balance is also observed in case TR3 as shown in figure 3.11, however exhibiting a larger pressure drop due to the rougher surface at the top boundary. Moreover, the flow recovery is observed faster in case TR3 than in case TR2 due to additional turbulent mixing.

A remarkable increase in the bottom shear stress  $\tau_b$  is noticed upstream of the rough transition in cases TR2 and TR3 around  $x_1^*/H \approx 0$ , compared to the bottom shear stress  $\tau_{bS}$  of the smooth transition case TS as seen in figures 3.10(b) and 3.11(b). In fact, the roughness condition of the carpet (in

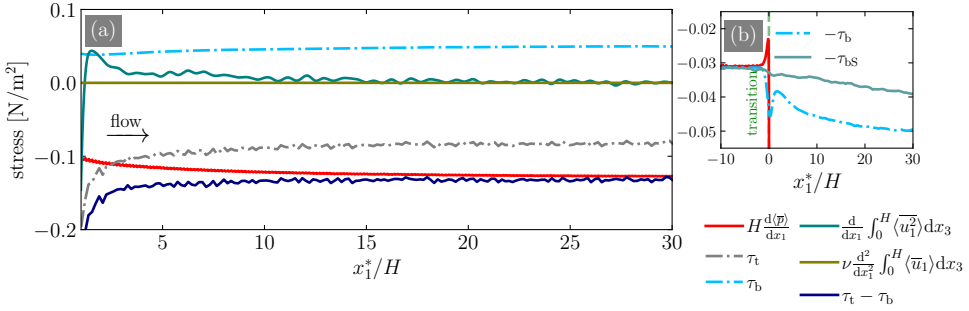


Figure 3.10: Different terms in the streamwise momentum balance for the fully developed flow in the closed section of case TR2. (a) Overall development along the streamwise direction after the transition, and (b) Change in bottom shear stress  $\tau_b$  (of case TR2) and  $\tau_{bS}$  (of case TS) in the vicinity of the transition. Throughout the transition region, the momentum balance is not complete without including momentum flux term.

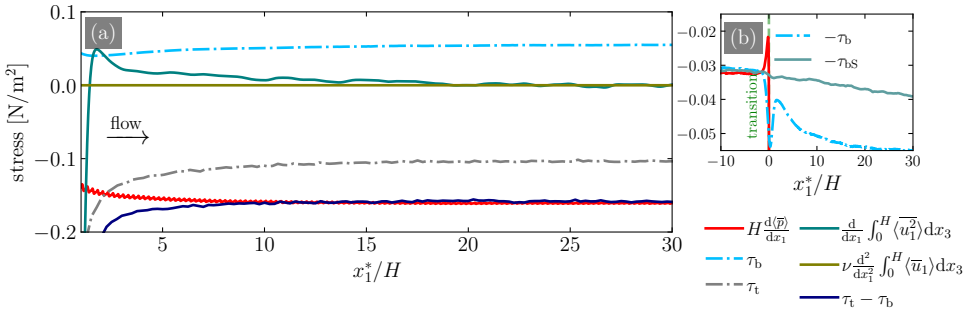


Figure 3.11: Same as in figure 3.10 for case TR3. Contrary to case TR2, the flow is observed to approach the fully developed condition faster in case TR3.

cases TR2 and TR3) enhances the bottom shear stress by two mechanisms: (1) the additional mixing or higher Reynolds shear stress near the rough wall pushes the position of maximum velocity further towards the smooth bottom wall, thus increasing the velocity gradient near the bottom wall, and (2) the presence of rough top boundary increases flow blockage, which leads to a slightly higher effective bulk velocity, resulting in a higher shear stress at the bottom boundary. The second mechanism is associated with streamlines convergence and flow acceleration, inducing a downward mean flow in the vicinity of the carpet. Therefore, the presence of the rough carpet, which alters the open channel flow into the closed channel, is mainly responsible for this increase in  $\tau_b$ , and consequently may enhance possibly the bed erosion in

the river. Such observations were reported in the study of ice-jams in the river by Luo et al. [66].

The above described phenomena are also reflected in the development of the turbulent kinetic energy ( $K = \langle u'_i u'_i \rangle / 2$ ) shown in figure 3.12 for case TR2. Near the transition (figure 3.12(a)), high values of  $K$  are observed due to intense turbulent fluctuations or normal Reynolds stresses. In the closed channel section (figure 3.12(b))  $K$  is generally higher near the rough top wall than near the smooth bottom wall because turbulent fluctuations are more intense due to the rough surface. The rougher top surface of case TR3 causes higher  $K$  and smooth top surface of case TS produces lesser  $K$  level, compared to case TR2. Moreover, the roughness of the top surface promotes  $K$  level near the bottom boundary as well, implying that in case of a mobile bed more erosion can be expected.

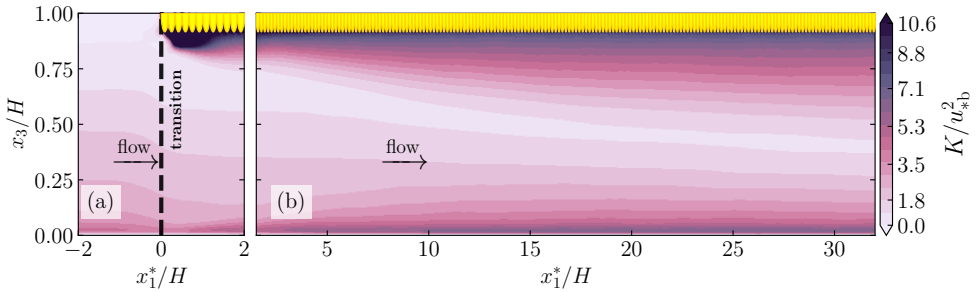


Figure 3.12: Turbulent kinetic energy  $K = \langle u'_i u'_i \rangle / 2$  (a) upstream of the transition, and (b) downstream of the transition of case TR2, normalised by the friction velocity of smooth open channel flow, case OS. Due to the transition, higher  $K$  level is observed not only near the top boundary but also close to the bottom boundary, which in turn enhances the mixing processes and potentially increases sediment erosion. The effect of the transition on the bottom boundary is via the convection of vortex shedding from the top shown in figure 3.22.

### 3.3.2 Skin friction

The friction coefficient for the carpet surface  $C_f^t$  is required to estimate the cumulative shear force acting on the carpet which is responsible for the squeezing instability, as discussed by Yan Toe et al. [63]. Though that study assumed fully developed flow conditions along the whole carpet, the flow transition from free-slip to no-slip in the presence of the carpet introduces non-negligible variation of friction coefficient along the streamwise direction, affecting the

accurate estimation of the compressive force. Similarly, the friction coefficient at the bottom  $C_f^b$  determines the bed shear stress and the associated turbulence level present in the water column at the transition as explained in Subsec. 3.3.1.

In this section, we discuss the local friction coefficients varying with the local Reynolds number  $Re^* = x_1^* U_{\max} / \nu$ . Unlike the common definition, the local skin friction coefficient  $C_f$  is defined here as  $2\tau_w / (\rho U_{\max}^2)$  where  $\tau_w$  denotes the wall shear stress for any type of surface, and  $U_{\max}$  the maximum streamwise velocity of the fully developed flow of the corresponding cases. First, simulations with periodic streamwise and spanwise boundary conditions (i.e., cases CS, OS, CR2, and CR3) provide benchmark values for the friction coefficient at the smooth bottom  $C_f^b$  and at the rough top  $C_f^t$ , indicated by the dashed different-coloured lines in figure 3.13. Since the flow conditions in the cases CS, OS, CR2, and CR3 are fully developed flow, their friction coefficients do not vary with respect to  $x_1^*$ . Moreover, the friction coefficients of smooth surfaces are found to be identical in the fully developed flow condition, regardless of any surface type at the other side of the channel, provided that the Reynolds numbers are the same. A small difference can be expected in the comparison if the maximum velocity is slightly different and its location is slightly displaced. This is observed in our results as well in figure 3.13(a), showing that three dashed lines for  $C_f^b$  (cases CR2 and CR3) and  $C_f^{t,b}$  (case CS) are almost identical.

Secondly, the results of simulations with flow transition (i.e., cases TS, TR2, and TR3) are shown in figure 3.13 with the solid different-coloured lines. Figure 3.13(b) shows the streamwise development of bottom friction coefficient  $C_f^b$  upstream of the flow transition, i.e., the open channel region for cases TS, TR2 and TR3. A constant friction coefficient is found till  $Re^* \leq -0.25 \times 10^5$  where the presence of the top boundary starts to interfere with the bottom boundary layer (figure 3.13(b)). It should be noted that, since the  $C_f^b$  is defined using  $U_{\max}$  of the fully developed flow in the open channel region instead of the local  $U_{\max}$  within the range of  $-0.25 \times 10^5 < Re^* \leq 0$ , the increase in  $C_f^b$  is observed locally due to the accelerating flow and higher bulk velocity. This is reflected in the shear stress development as previously shown in figure 3.10.

Downstream development of  $C_f^b$  after the transition is shown in figure 3.13(a) for cases TS, TR2, and TR3. Adjacent to the transition, the development of  $C_f^b$  undergoes a transitional stage until it approaches the benchmark results of periodic cases CS, CR2 and CR3 at the fully developed condition ( $Re^* = 5 \times 10^5$ ), which all provide the same  $C_f^b$  value (figure 3.13(a)). Compared to the value

of  $C_f^b$  upstream of the transition,  $C_f^b$  is found larger downstream of the transition, which is also consistent with the rise of turbulent kinetic energy level  $K$  near the bottom boundary after the transition, as shown in figure 3.12. Experimental result of  $C_f^b$  is observed slightly larger than the numerical result of case TR2 at the same Reynolds number  $Re^*$  because of additional sidewalls in the experimental set-ups (figure 3.13). It is noted that in the laboratory experiments,  $C_f^b$  and  $C_f^t$  are indirectly estimated by a linear extrapolation of the measured Reynolds shear stress profile assuming a linear stress profile of the fully developed condition.

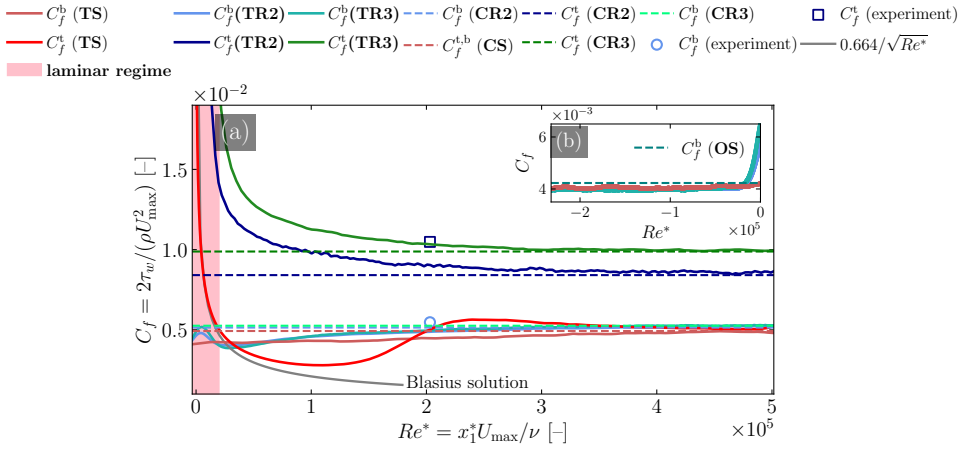


Figure 3.13: Friction coefficients for smooth carpet (case TS) and rough carpet (cases TR2 and TR3): (a) downstream of the transition, and (b) upstream of the transition, based on the local Reynolds number  $Re^*$ . Benchmark results from simulations using periodic boundary conditions are also shown in dashed lines. It should be noted that extreme values of  $C_f^t$ (TR2) and  $C_f^t$ (TR3), which correspond to the leading edge of the carpet, are excluded here for the sake of clarity, but discussed in Subsec. 3.3.4.

Now, the development of friction coefficient at the top boundary  $C_f^t$  is studied for cases TS, TR2 and TR3. In the smooth transition case TS, the initial part of the developing  $C_f^t$  follows the Blasius solution  $0.664/\sqrt{Re^*}$ , followed by the transitional stage to the turbulent region as shown in figure 3.13(a). This behaviour is consistent with the observations reported by [31]. Detailed comparison of current DNS results with Blasius profile is discussed in Appendix 3.D, showing the excellent agreement until the point of transition ( $x_1^*/H \approx 1.2$  or  $Re^* \approx 20 \times 10^3$ ) before the turbulent boundary layer. Thereafter, the friction coefficient approaches the benchmark  $C_f^b$  value of the smooth surface. Therefore, these observations collectively suggest that despite

the flow transition due to the presence of the smooth carpet, the friction coefficient approaches the statistically stationary values observed for the periodic cases at the location of fully developed flow i.e.,  $Re^* = 5 \times 10^5$  (figure 3.13(a)).

Similarly, in cases TR2 and TR3, the development of  $C_f^t$  follows a similar trend of the rough boundary layer development as discussed earlier in figure 3.7. After the transition stage, their local friction coefficients  $C_f^t$  are found almost identical to the benchmark values of cases CR2 and CR3 in fully developed conditions, respectively. Having observed the development of  $C_f^t$  along the streamwise direction in case TR2, it can be concluded that  $C_f^t$  attains the fully developed value ( $\simeq 8.64 \times 10^{-3}$ ) at  $Re^* = 3 \times 10^5$ . Experimental result of  $C_f^t$  is found to be larger than the simulation result of case TR2 at the same  $Re^*$  (figure 3.13) due to additional shear stress of the sidewalls than in the numerical simulations without the sidewalls.

### 3.3.3 Eddy viscosity and $z_m$ versus $z_{\tau=0}$

This subsection discusses the eddy viscosity  $\nu_t$  for cases TS, TR2, and TR3, which is an indication of momentum mixing and also an important parameter for the turbulence closure models such as  $k - \varepsilon$  model. The eddy viscosity  $\nu_t$  can be calculated using (1) the definition of Reynolds shear stress  $-\langle u'_1 u'_3 \rangle = \nu_t dU/dx_3$  where  $U = \langle \bar{u}_1 \rangle$ , and (2) the definition as used in the  $k - \varepsilon$  model ( $\nu_t = C_\mu K^2/\varepsilon$  where  $C_\mu$  is an empirical coefficient typically taken as 0.09) using the relations  $K = \langle \overline{u'_i u'_i} \rangle/2$  and  $\varepsilon = \nu \langle \frac{\partial u'_i}{\partial x_j} \frac{\partial u'_i}{\partial x_j} \rangle$  [89]. This was proven valid for the log-law region of boundary layer [89]. It is noted that this constant 0.09 fails for the near-wall region where the turbulence is highly anisotropic, which is not considered here.

Ideally, these two aforementioned approaches should provide similar results of  $\nu_t$  for the region away from the wall or middle part of the closed channel. In figure 3.14, which shows the  $\nu_t$  profiles for cases CS, CR2, and CR3 along with experimental data, a distinct discontinuity is observed only in cases CR2 and CR3 when the first approach is used. This discontinuity is located at the position of  $z_m$  (i.e.,  $dU/dx_3 = 0$ ) for these two asymmetric cases, denoted by the horizontal blue and black dotted lines, respectively (figure 3.14). This behaviour is not observed, however, in case CS which is a simply closed smooth channel flow, indicated by the red dotted line. Applying the second approach does not show any discontinuity in  $\nu_t$  profiles for all of cases, as denoted by the dashed lines in figure 3.14.

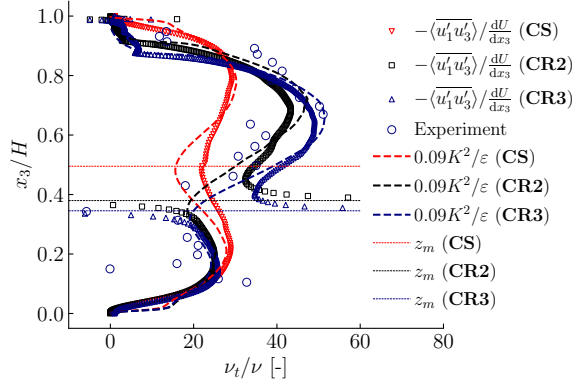


Figure 3.14: Eddy viscosity profiles using two different calculation approaches: (1)  $\nu_t = -\langle u'_1 u'_3 \rangle / \frac{dU}{dx_3}$ , and (2)  $\nu_t = C_\mu K^2 / \varepsilon$  where  $C_\mu = 0.09$ . The first approach leads to a discontinuity for asymmetric roughness cases (case CR2 and case CR3) while the second approach results in the continuous profile for all cases. Nevertheless, both approaches demonstrate overall similarity.

Therefore, the second approach, which calculates  $\nu_t$  using  $K$  and  $\varepsilon$ , is adopted in this work, as it avoids the discontinuity and shows overall good agreement with the first approach,  $\nu_t = -\langle u'_1 u'_3 \rangle / \frac{dU}{dx_3}$ , in the outer wall region for all cases. Figure 3.15 shows the streamwise development of  $\nu_t$ , normalised by the molecular viscosity  $\nu$ , for case TR2 by using the second approach for calculating  $\nu_t$ . Just upstream of the transition, a zone of high turbulent mixing is observed from  $x_3/H \approx 0.25$  to  $x_3/H \approx 0.65$  shown by the red rectangle in figure 3.15(a). This in turn can influence the transported material such as plastic and sediment particles. Above this energetic mixing zone, turbulent mixing decreases again because of downward inclined accelerated flow at the leading-edge of the carpet. After the flow transition,  $\nu_t$  develops toward the benchmark profile, which resembles a double quadratic profile in figure 3.14. For case TR3, a similar behaviour is observed with the energetic mixing zone ranging from  $x_3/H = 0.15$  to  $x_3/H = 0.5$  (figure not shown here), which shifts downwards slightly. The wavy pattern indicated by the box in figure 3.15(b) arises from insufficient temporal averaging of the higher-order statistics used in  $k - \varepsilon$  model, without affecting the overall results here.

Figure 3.16 compares the vertical profiles of the viscous stress and the Reynolds shear stress for the periodic cases CS, CR2 and CR3, normalised by the total bottom shear stress  $\rho u_{*b}^2$  of the corresponding case. In case CS, the location of maximum velocity  $z_m$  coincides with the location of zero Reynolds

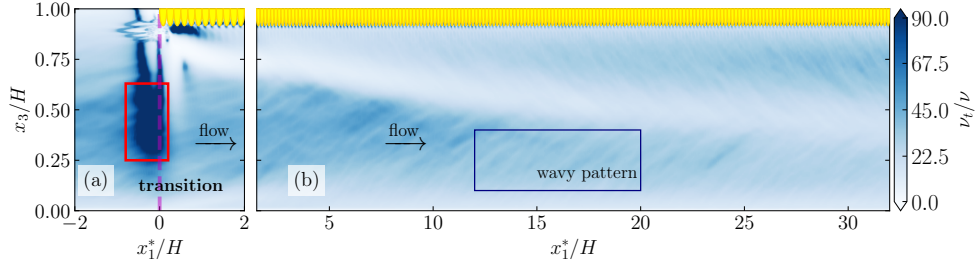


Figure 3.15: Development of eddy viscosity  $\nu_t$ , normalised by the molecular viscosity  $\nu$ , for case TR2 (a) upstream of the transition, and (b) downstream of the transition. Before the transition, energetic turbulent mixing is observed in the middle part of water column while the lower mixing zone is near the free surface due to the downward accelerated flow. After the transition,  $\nu_t$  approaches the benchmark profile shown in figure 3.14.

shear stress  $z_{\tau=0}$ , which is a necessity resulting from the symmetry of the flow configuration (figure 3.16(a)). In case CR2 (figure 3.16(b)) and case CR3 (figure 3.16(c)), however,  $z_m$  is observed above  $z_{\tau=0}$  i.e., the location of zero shear stress is closer to the smoother boundary compared to the location of maximum velocity. Therefore, the absolute value of shear stress is found large ( $|\tau| > 0$ ) at the location of  $z_m$ , indicated by the gap in the figures 3.16(b) and 3.16(c). Consequently, dividing a larger numerator by a smaller denominator leads to an extreme value and discontinuity in their  $\nu_t$  profiles. Such a discrepancy between  $z_m$  and  $z_{\tau=0}$  was reported in the experimental study of [28], and later approved by [23] who used the simple turbulence closure model of [1], elaborated in Appendix 3.E.

Following the model of [1], the shear stress at  $z_m$ , denoted as  $\tau_m$ , is estimated for cases CR2 and CR3 indicated by the filled triangle symbols in figures 3.16(b) and 3.16(c). Therefore, our numerical results for asymmetric roughness channels underpin the observation of the  $z_m > z_{\tau=0}$ , showing a good agreement with the prediction of [1]’s turbulence model. However, more importantly, the fact that the location of zero shear stress does not coincide with the location of zero velocity gradient questions the validity of the eddy viscosity modelling approach in these asymmetric flows.

### 3.3.4 Streamlines near the transition and flow separation

When the flow approaches an obstacle or undergoes the new physical boundary, streamlines can deflect and separate based on the submergence-depth

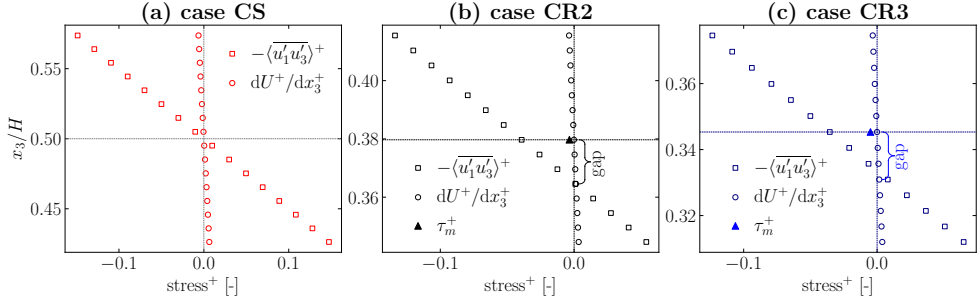


Figure 3.16: Shift between the position of zero Reynolds shear stress ( $\tau_{13}^+ = -\langle u'_1 u'_3 \rangle^+ = 0$ ) and the position of maximum streamwise velocity  $U_{\max}$ . The analysis is performed using the data from (a) case CS, (b) case CR2, and (c) case CR3.  $\blacktriangle$  and  $\blacktriangleleft$  denote the estimated  $\tau_{13}^+$  at the positions of  $U_{\max}$  using the turbulence model of [1] for case CR2 (figure 3.16(b)) and case CR3 (figure 3.16(c)), respectively.

Reynolds number  $Re_k = kU_{\text{FS}}/\nu$  [37] defined using the incoming free-stream velocity  $U_{\text{FS}}$  equivalent to the maximum velocity  $U_{\max}$  in the open channel region, and submergence height which is equal to the roughness height  $k$  in our case. Using the simulation input parameters (table 3.1),  $Re_k$  is calculated as 1140 for case TR2 and 1925 for case TR3, respectively. For both cases, flow separation can still occur at the transition point in the lower range of Reynolds number [37, 90]. In this section, we will discuss flow separation and its consequence on the force on the particles near the transition.

The streamlines in wall-normal  $(x_1, x_3)$  plane are shown for two different spanwise positions of the sphere,  $x_2/d_p = 0.00$ , and  $x_2/d_p = 0.50$  of case TR2 in figure 3.17, and for case TR3 in figure 3.18. Here,  $x_2/d_p = 0.00$  corresponds to the locations between adjacent spheres, while  $x_2/d_p = 0.50$  indicates the position of middle plane of a single sphere. To this end, the streamlines are averaged in the  $x_2$  direction only at their corresponding  $x_2/d_p$  positions. Flow separation was observed in between the adjacent spheres (figures 3.17(a) and 3.18(a)) whereas streamline deflection occurs under the spheres, i.e.,  $x_2/d_p = 0.5$  (figures 3.17(b) and 3.18(b)). Their net effect can be obtained by averaging the streamlines over the whole spanwise direction similar to the concept of phase averaging where the phase is the spanwise position over one sphere, resulting in the net flow reversal as indicated in figure 3.19(b). In case TR3, the streamlines show a stronger downward deflection due to the larger roughness elements, followed by a larger flow separation zone, while the overall flow behaviour is qualitatively similar to that in case TR2. Therefore,

the magnitude of streamlines deflection is specific to the size of the spheres.

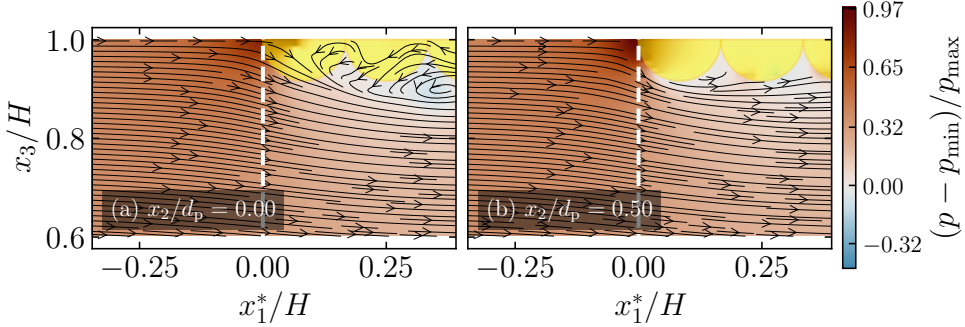


Figure 3.17: Streamlines near the transition for each sphere's spanwise direction (case TR2): (a)  $x_2/d_p = 0.00$ , the position between two adjacent spheres, and (b)  $x_2/d_p = 0.50$ , the middle position underneath the single sphere.

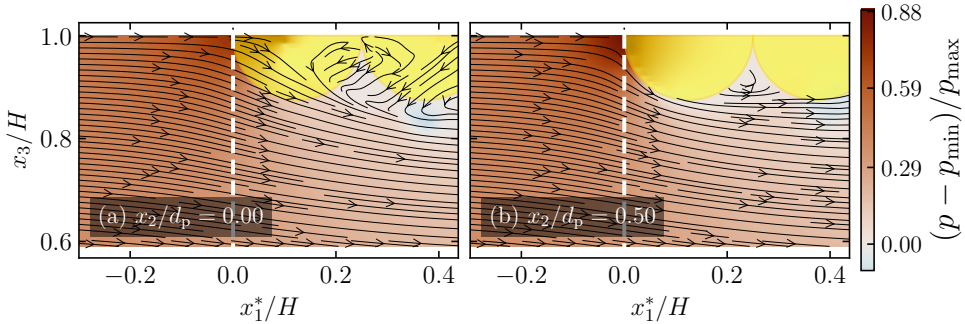


Figure 3.18: Same caption as in figure 3.17 for case TR3. Compared to case TR2, the larger spheres in case TR3 result in a larger downward deflection of the streamlines at the transition.

The net flow separation occurs within the streamwise distance of approximately  $0.2 < x_1^*/H < 0.7$ , which consequently affects the force direction on the spheres in the carpet. As shown in figure 3.19(a), the mean shear stress on the third and fourth rows of spheres is acting along the negative  $x_1$  direction (i.e., upstream direction) because of the flow reversal underneath the carpet. Therefore, these particular spheres seem to be pushed in the opposite direction to the mean flow, therefore interacting with the spheres at the leading edge of the carpet which senses a force in the positive direction (i.e., downstream direction). Such a dynamic balance of forces between the adjacent spheres

can disturb the position of the spheres, leading to the erosion instability of the carpet. Due to the relatively large stagnation force on the leading-edge row of the spheres shown in figure 3.19, the particle erosion occurs eventually in the positive  $x_1$  direction.

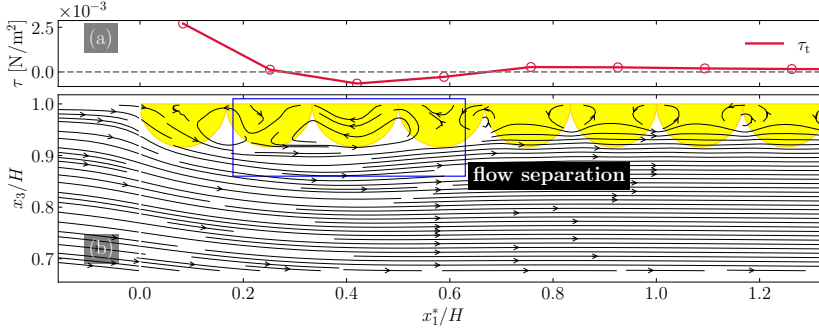


Figure 3.19: Flow separation under the carpet at  $Re_k = 1140$  using spanwise-averaged velocity data for case TR2: (a) Shear stress variation along the carpet of which the third and fourth rows of spheres experienced by the negative  $x_1$  direction stress, and (b) flow reversal under the carpet, disappearing after  $x_1^*/H \approx 0.7$ .

Spanwise spatial variation due to the spheres also creates a secondary circulation in-between the roughness elements [91], leading to the formation of helical flow structures. We emphasize the flow pattern in the vicinity of the transition point i.e., underneath the first two rows of spheres in the spanwise plane as illustrated in figure 3.20 for case TR2. Each panel of the figure 3.20 shows the  $x_2 - x_3$  plane view of the streamlines under the sphere in the increasing streamwise  $x_1$  position. Panels (a,b,c,d,e and f) show the streamline pattern under the first row of spheres where the strong downward deflected flow occurs. Near the second row of spheres, secondary circulation cells are observed in-between the spheres as shown in panels (g,h and i), accompanied by higher turbulent shear stress also due to streamwise flow separation. A combination of streamwise flow separation and spanwise circulation will form a complex three-dimensional flow structure near the roughness elements.

### 3.3.5 Principal-strain and vorticity

To investigate the effect of deflected flow on the fluid deformation, an analysis of maximum principal-strain axis  $\beta'_{\max}$  (the direction of maximum rate of strain [89]) and the magnitude of strain rate  $\epsilon'_{\max}$  is performed for cases TR2

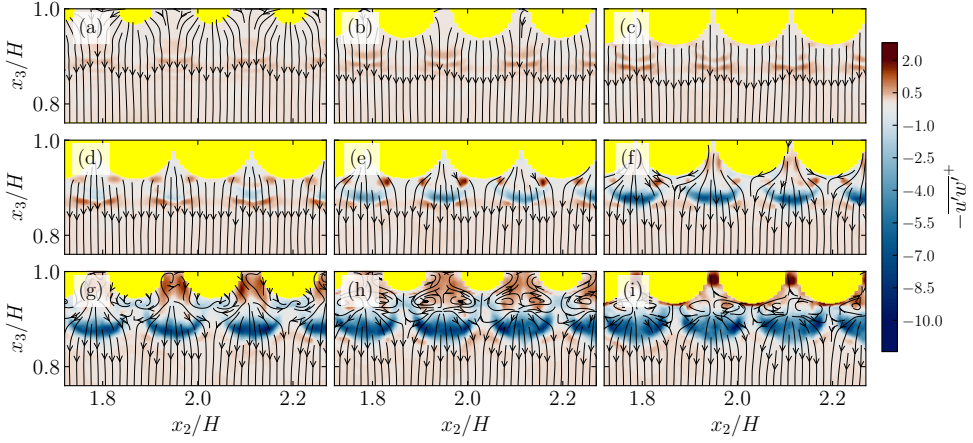


Figure 3.20: Streamlines near the transition point i.e., under the first two rows of spheres) in the spanwise  $x_2 - x_3$  plane for case TR2. Each panel shows streamlines of each plane under the sphere in the increasing  $x_1$  position. Panels (a,b,c,d,e,f) denote the first row that experiences the strong downward deflected flow. Nearby the second row of spheres shown in panels (g,h,i), the secondary circulation is observed in-between the spheres, accompanied by higher turbulent shear stress.

and TR3, assuming a two-dimensional flow problem in wall-normal ( $x_1, x_3$ ) plane. This phenomenon can cause the plastic waste fibers or other pollution agents to orient with this strain axis. In general, for canonical closed channel flow the angle  $\beta'_{\max}$  is directed at  $\pm 45^\circ$  from the  $x_1$  direction, showing the alignment of vortices, especially near the surface boundary. Besides, the strain rate magnitude  $\epsilon'_{\max}$  is strongest within the viscous sublayer or high shear layer and is weakest in the channel center.  $\epsilon'_{\max}$  can be calculated as the largest eigenvalue of mean strain rate tensor or using the following expression

$$\epsilon'_{\max} = \frac{\epsilon_{11} + \epsilon_{33}}{2} + \sqrt{\left(\frac{\epsilon_{11} - \epsilon_{33}}{2}\right)^2 + \epsilon_{13}^2} \quad (3.8)$$

where  $\epsilon_{11} = \frac{\partial u_1}{\partial x_1}$ ,  $\epsilon_{33} = \frac{\partial u_3}{\partial x_3}$ , and  $\epsilon_{13} = \frac{1}{2} \left( \frac{\partial u_1}{\partial x_3} + \frac{\partial u_3}{\partial x_1} \right)$ , all averaged over time and spanwise direction. The averaging operators are dropped here for clarity. Similarly,  $\beta'_{\max}$  can be found as the eigenvector in the  $x_1 - x_3$  plane corresponding to the largest eigenvalue of mean strain rate tensor or as below

$$\tan(2\beta'_{\max}) = \frac{2\epsilon_{13}}{\epsilon_{11} - \epsilon_{33}} \quad (3.9)$$

Figures 3.21(a) and 3.21(b) show the maximum principal-strain axis and its magnitude for case TR2, respectively. Due to the flow deflection at the transition point, the principal-strain axis changes from a positive direction to a negative direction near the free surface, as indicated by the brown blob in figure 3.21(a). After the transition, two different principal-strain axes are observed with positive direction (blue zone) and negative direction (brown area) near each side of the wall boundaries (figure 3.21(a)). This means that the maximum strain is directed in the positive direction near the bottom boundary and changes to a negative direction in the rough top boundary.

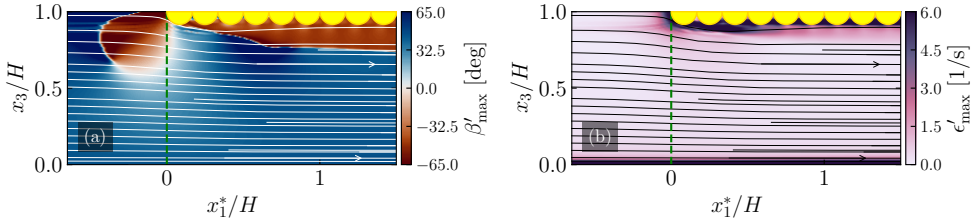


Figure 3.21: Principle-strain axis orientation and magnitude of maximum principle-strain for CR2.

Regarding the principal-strain rate magnitude  $\epsilon'_{\max}$  at the flow transition (figure 3.21(b)), its magnitude seems not very strong near the free surface, compared to the vicinity of the bottom, though its axis direction does strongly change (figure 3.21(a)). Nevertheless, the strain still occurs near the free surface at the transition point because of the flow deflection.

Figure 3.22 shows the mean spanwise vorticity  $\omega_2$  and streamwise vorticity  $\omega_1$ , both temporal- and spanwise-averaged, and normalised by  $u_{*b}^2/\nu$ . At the point of flow transition, highly intense counterclockwise vortices  $\omega_2$  are observed, which can cause particle erosion at the leading edge of the carpet, as shown in figure 3.22(a). Afterwards, the intensity of  $\omega_2$  diffuses in the downstream direction while keeping its counterclockwise orientation. Figure 3.22(b) exhibits the streamwise vorticity  $\omega_1$  in the wall normal ( $x_2, x_3$ ) plane for the transition point. Alternating streamwise vortices are observed near the carpet layer, of which magnitudes are significantly higher than those near the bed. The region where these alternating vortices occur are confined close to the carpet, not throughout the whole water column.

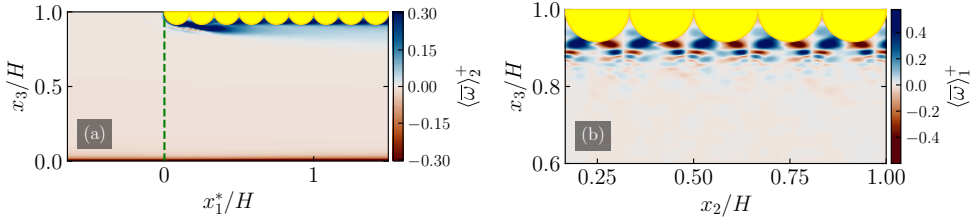


Figure 3.22: (a) Mean spanwise vorticity  $\omega_2$ , and (b) mean streamwise vorticity  $\omega_1$ , normalised by  $u_{*b}^2/\nu$ , for case TR2. The top rough boundary generates strong spanwise vorticity at the transition point, which is subsequently convected toward the bottom boundary, enhancing mixing processes and potentially increasing riverbed erosion. Alternating patterns of streamwise vortices are observed around the particles near the top boundary.

### 3.3.6 Statistics of the forces on the particles

Having discussed the hydrodynamics at the flow transition, we now discuss the forces acting on the spheres of the carpet. Spanwise-averaged forces acting on each  $l^{\text{th}}$  row of the spheres  $\langle F_i \rangle_l$  are discussed with their temporal-mean values and standard deviations along the carpet. Figure 3.23 shows the mean values of streamwise directed force  $\langle \bar{F}_1 \rangle_l$  and wall-normal directed force  $\langle \bar{F}_3 \rangle_l$  acting on each row of spheres along the carpet until the first 15 rows for cases TR2 and TR3. The mean values are obtained by averaging in time and spanwise direction. Figure 3.23 also shows the streamwise variation of their standard deviation values  $\sigma_{F_1}$  and  $\sigma_{F_3}$  along the carpet, multiplied by 4 for the sake of clear visualization. The results are normalised by  $\frac{1}{2}\rho U_{\max}^2 \frac{1}{2}A_p$  where  $U_{\max}$  is the maximum velocity of the open channel flow and  $\frac{1}{2}A_p$  is the exposed half area of the particle. Force fluctuation is relatively small at the 1<sup>st</sup> row of spheres while more important fluctuations in the hydrodynamic force are observed between 2<sup>nd</sup> and 5<sup>th</sup> row, which coincide with flow separation zone as illustrated in figure 3.19. Afterwards, the force fluctuations do not vary much along the carpet and are therefore omitted here for brevity (figure 3.23).

As reported by [63], the squeezing instability occurs to the particles inside the carpet, especially near the downstream edge or trailing edge rather than at the leading edge, because of the cumulative shear force of the upstream particles. By definition of the squeezing instability, the mean force is considered a more important contribution compared to the instantaneous force events that result from turbulent fluctuations. Moreover, significant force fluctuations are not observed after the 11<sup>th</sup> row of the particles in both cases TR2 and TR3

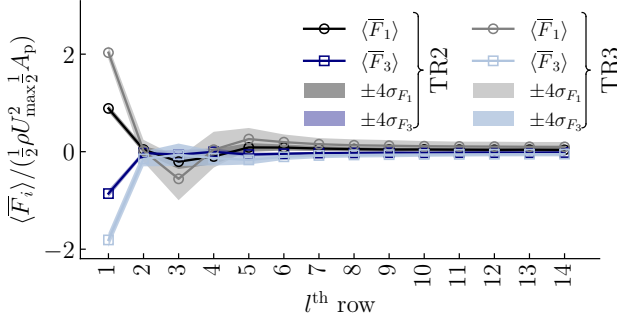


Figure 3.23: Mean and standard deviation of streamwise direction and wall-normal direction forces,  $F_1$  and  $F_3$ , respectively acting on each  $l^{\text{th}}$  row of the particles in the carpet for cases TR2 and TR3. The results are normalised by  $\frac{1}{2}\rho U_{\max}^2 \frac{1}{2}A_p$  where  $U_{\max}$  is the maximum velocity of the open channel flow.

(figure 3.23). The mean force acting on the first row is found to be relatively larger than the force on the following rows of the spheres in the carpet (figure 3.23). Therefore, the cumulative force  $\langle \bar{F}_1 \rangle$  acting on the particle inside the carpet can be estimated by integrating the *developing* force distribution along the carpet up to that particular particle's position more accurately than by just using the fully developed flow's  $C_f^{\text{t}}$  result as discussed in Subsec. 3.3.2.

In contrast to the squeezing instability, the erosion instability is triggered by a combined effect of the drag force and turbulent fluctuation forces near the transition. As shown in figure 3.23, the standard deviations of the forces  $\sigma_{F_1}$  and  $\sigma_{F_3}$  at the 1<sup>st</sup> row are not as significant as at 2<sup>nd</sup>, 3<sup>th</sup> and 4<sup>th</sup> rows where flow separation dominates. However, the mean force acting on these rows of spheres are much smaller than the mean force acting on the first row (figure 3.23), and therefore the first row is highly vulnerable to erosion. It should be noted that the previously discussed results are based on the spanwise-averaged force values, therefore the extreme force events are smeared out due to averaging.

Therefore, using the data collected on a single particle in the first row, we analyze the probability density function (p.d.f) of the horizontal and vertical forces acting on it to understand the extreme force events. Figures 3.24(a) and 3.24(b) show the p.d.f of turbulent fluctuation forces  $F'_1$  and  $F'_3$  for cases TR2 and TR3, normalised by their standard deviations  $\sigma_{F_1}$  and  $\sigma_{F_3}$ . For both cases TR2 and TR3, the tail of the  $F'_1$  p.d.f. is right-skewed, while that of  $F'_3$  is left-skewed, compared to the Gaussian distribution. This skewness is attributed to the flow transition, where the horizontal impact force  $F'_1$  prevails

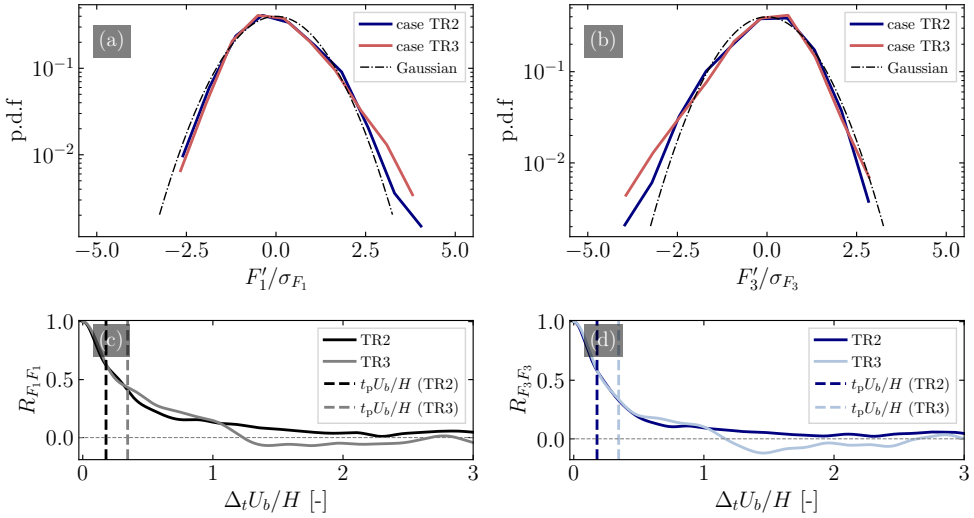


Figure 3.24: Normalised probability density function (p.d.f) of the forces acting on a single particle in the first row of the carpet: (a)  $F'_1$ , (b)  $F'_3$  for cases TR2 and TR3, (c) auto-correlation function  $R_{F_1 F_1}$  for  $F_1$ , and (d)  $R_{F_3 F_3}$  for cases TR2 and TR3. The particle response times  $t_p$  for  $d_p = 2$  cm and  $d_p = 3$  cm are shown using  $\rho_p = 500.0$  kg/m<sup>3</sup>.

in contrast with a uniform flow for which the skewness is not observed.

Though the shape of the p.d.f is skewed, the question of whether these extreme events can contribute to triggering the erosion instability or not, is not obvious. Indeed, particle erosion or dislodgement is determined not only by the magnitude of the force but also by whether the duration of the force is sufficient for the particle to respond. Therefore, we relate the particle's response time  $t_p$  and temporal auto-correlation functions for horizontal and vertical force components,  $R_{F_1 F_1}$  and  $R_{F_3 F_3}$ , respectively, to investigate the temporal scale of fluid-particle interaction. The particle's response time  $t_p$  is estimated using

$$t_p = \frac{\rho_p d_p^2}{18\mu(1 + 0.15Re^{0.687})} \quad (3.10)$$

where  $\rho_p$  is the density of the particle (taken as 500.0 kg/m<sup>3</sup>, since half of the sphere is submerged in the computational domain) and  $\mu$  is the dynamic viscosity of the fluid (10<sup>-3</sup> kg/m/s) [92].

Figures 3.24(c) and 3.24(d) show the temporal auto-correlation functions  $R_{F_1 F_1}$  and  $R_{F_3 F_3}$  for cases TR2 and TR3, and the particle response time  $t_p$

are also shown for  $d_p = 2$  cm and  $d_p = 3$  cm. The temporal correlation of forces with durations shorter than the particle's response time (to the left of the vertical lines in figure 3.24) occurs on a time scale too brief to contribute significantly to particle erosion. Therefore, the force fluctuations corresponding to these time scales should be reduced accordingly in the analysis. This consideration is similar to the impulse-base criterion of [93]. Larger particles require longer duration of extreme events to erode than the smaller particles (figures 3.24(c) and 3.24(d)), consistent with the findings of [94].

While it is not directly shown here, figures 3.24(c) and 3.24(d) should not be interpreted to suggest that the equilibrium conditions forced in the static carpet simulation cannot occur, since the stability of the carpet relies not only on the characteristic time scale of the force but the impulse i.e., force times the duration over which the force acts, that determines the stability the individual particle. Inspired by laboratory experiments of [63], the imposed bulk velocity  $U_{bH}$  in the numerical simulation is set well below the threshold velocity for particle erosion. It is therefore justified to assume that the simulated carpet remains undeformed and static during the flow development. Increasing the bulk velocity in the simulation would induce particle erosion, necessitating a dynamic particle simulation, which is computationally expensive for this particular  $Re_{bH}$  and domain size.

The downward destabilizing force ( $F_\downarrow$ ) acting on a sphere in the first row of the carpet was estimated by Yan Toe et al. [63], based on the definition of erosion as the complete dislodgement of the sphere from the carpet. The reader is referred to that work for further details. Here, we briefly revisit the explanation for clarity. The downward destabilizing force sketched in figure 3.25 is estimated as

$$F_\downarrow = F_{DH} \tan \theta + F_{DA} + F'_a \quad (3.11)$$

where  $F_{DH}$  denotes the horizontal component of the drag force directing along the curved streamline (or) the contact force with the adjacent particle,  $\theta$  the misalignment angle between the centre of the eroded sphere and the undisturbed sphere,  $F_{DA}$  downward component of the drag force of the deflected streamline  $F_D$ , and  $F'_a$  the turbulent pressure fluctuation force emerged from the fully developed open channel flow upstream of this point and estimated by  $\rho C_f^b U_{bH}^2$  where  $C_f^b$  is the friction velocity of the open channel flow. To estimate  $F_{DH}$  and  $F_{DA}$ , the deflection angle of the approached streamline in the undisturbed condition ( $\alpha$ ) is required and it is found  $19^\circ$  using  $\arctan(\langle \bar{u} \rangle_y / \langle \bar{u} \rangle_x)$  for case TR2. In the present configuration, since the spheres are fixed in the com-

putational domain without any vertical movement, the misalignment angle  $\theta$  between two particles is zero, resulting in the destabilizing force  $F_{\downarrow} = F_{DA} + F'_a$  where  $F_{DA} = F_D \sin \alpha$ . The drag force acting on the particle due to the deflected streamline  $F_D$  is calculated as  $0.5\rho C_D U_{bH}^2 A_p$  where  $C_D$  denotes the drag coefficient of the sphere, taken to be 0.5 [63].

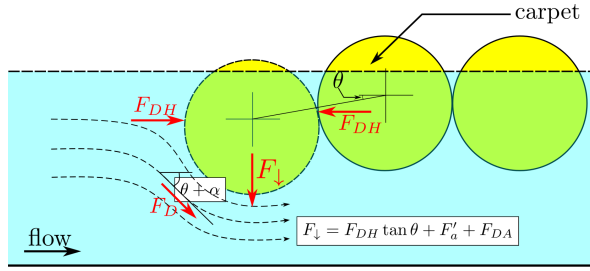


Figure 3.25: Sketch for force definitions in Eq. 3.11:  $F_D$  denotes fluid drag force acting along the deflected streamline,  $F_{DH}$  horizontal component of  $F_D$ ,  $F_{DA}$  vertical component of  $F_D$  (i.e.,  $F_{DA} = F_D \sin(\alpha + \theta)$ ),  $F'_a$  turbulent fluctuation force,  $\alpha$  the angle of streamline deflection in the undisturbed condition where the particle does not mobilise, and  $\theta$  the misalignment angle between the particles (based on [63]).

The mean downward force for case TR2 is calculated to be 0.0003 N, which is significantly lower than the numerical simulation result of 0.0011 N. Similarly, for case TR3, the numerical simulation provides 0.0022 N while the analytical equation predicts 0.0007 N with the streamline deflection angle  $\alpha \approx 20^\circ$ . This discrepancy may be attributed to the lower drag coefficient of the sphere  $C_D$  assumed in the formulation of  $F_D$ . In fact, the drag coefficient needs to be accurately determined for a sphere situated in the flow transition region and packed among adjacent spheres, as this configuration significantly differs from that of an isolated sphere in a uniform flow.

### 3.4 Conclusions

This study examined the hydrodynamics associated with the transition from open-channel to closed-channel conditions, drawing motivation from practical challenges such as ice cover in rivers, plastic debris accumulation at hydraulic structures, and log jams at bridges. In such scenarios, the flow undergoes a redevelopment of the boundary layer at the newly formed top surface. Simultaneously, the flow near the bottom boundary must adjust to the evolving

hydrodynamic conditions induced by the transition.

To better understand the flow physics in such a transition, we employed Direct Numerical Simulation (DNS) coupled with the volume penalization technique to answer the following questions:

1. How do the shear stresses and the friction coefficients develop along the bottom and top boundaries beyond the carpet transition?

At the transition, the bottom shear stress forms a hump-shaped profile, in contrast to the relatively uniform stress observed in the open channel section, and gradually approaches a constant value at the fully developed flow condition of the closed channel section. This hump-shaped shear stress profile is attributed to flow acceleration caused by the cross-sectional contraction, as well as the downward streamline deflection induced by the carpet geometry. As for the top carpet boundary, the shear stress at the transition is significantly large compared to the stress along the whole carpet, and it decreases to the constant value of fully developed flow condition. Due to the flow separation under the carpet, especially near the transition, the shear stress opposite to the mean flow occurs there. As the shear stress is significantly large near the transition, evaluating the accurate cumulative compressive force should include the complete stress development as  $\int_0^\lambda \tau_t(x_1) B dx_1$ , rather than just considering the constant shear stress of fully developed condition as  $\tau_t \lambda B$ .

Analysis of the friction coefficients  $C_f^t$  and  $C_f^b$  for the flow transition cases show that their developing behaviour is similar to what is observed in a developing pipe flow. Once the flow in the transition cases reaches the fully developed condition, their  $C_f^t$  and  $C_f^b$  values are also found to be similar with those in the benchmark cases.

2. What changes in the mean flow are observed near the transition?

Analysis of the force balance indicates that significant flow acceleration occurs at the transition because of the abrupt change in the boundary condition from a free-slip to a no-slip. In the transition region, the local acceleration force is balanced predominantly by the pressure gradient force until the flow approaches the new fully developed region. Moreover, streamlines are observed to be deflected around the leading-edge of the top boundary, followed by a short region of flow separation. The streamline deflection turns the angle of the fluid's principal-strain

to the negative direction, even *before* the transition point. This means that the flow is already affected upstream of the transition. The negative principal-strain direction can cause fiber-like plastic wastes to align with it during their transport trajectory.

3. What are the implications for the river bed scouring, and particle instability of the debris accumulation?

Due to the asymmetric roughnesses at the top and bottom boundaries, the location of streamwise maximum velocity  $z_m$  is found to be different from the location of zero shear stress  $z_{\tau=0}$ , supporting the experimental observation of [28, 23] who observed that  $z_{\tau=0}$  is closer to the smooth wall than  $z_m$ . Moreover, the asymmetric roughness causes  $z_m$  and  $z_{\tau=0}$  shift further toward the smoother surface. Therefore, the practical consequence of the rough top boundary can be seen in the river bed erosion under the debris accumulation or ice-jams. Besides, in the above-mentioned flow separation region, the particles experience a force acting in the opposite direction to the mean flow, thus counteracting with the preceding particles experiencing a force in the mean flow direction. This leads to the particles being more vulnerable to erosion instability. Eventually, the stagnation force acting on a preceding particle is relatively larger than this opposite force, therefore the mean resultant erosive force will be in the positive  $x_1$  direction.

Although this study employs a fixed top rough surface to model the geometric transition without incorporating significant vertical motion, the results demonstrate a good agreement with experimental observations from similar configurations. Future research should incorporate the dynamic motion of the accumulation layer, including the movement of individual particles, to more accurately capture the temporal dynamics of particle squeezing and erosion.

### 3.A Validation of volume penalisation method in CaNS

To validate the volume penalisation functionality of CaNS, we performed a benchmark test as a similar setup of Chan-Braun et al. [83], which is an open-channel flow over the rough bed. That study included the additional sublayer under a top layer of spheres and spacing  $2\Delta x$  between the spheres ( $\Delta x$  is the mesh spacing), whereas our simulation set-up does not consider the sublayer and the extra spacing (details in table 3.2).

Table 3.2: Simulation set-ups for benchmark test (from Chan-Braun et al. [83]) and current method (case OR).  $N_1, N_2$ , and  $N_3$  denote the number of meshes in streamwise, spanwise and wall-normal directions, respectively.

Case	$L/H$	$B/H$	$d_p/H$	$Re_{bH}$	$N_1 \times N_2 \times N_3$	Extra layer	Spacing
Chan-Braun et al. [83]	12.0	3.0	0.178	2880	$3072 \times 768 \times 256$	Yes	$2\Delta x$
Current Method	12.0	3.0	0.178	2880	$3072 \times 768 \times 256$	No	0

Figure 3.26(a) and 3.26(b) show the streamwise mean velocity  $U$  shifted by the virtual origin  $z_0$  in the linear scale and in the semi-log scale, respectively. In figure 3.26(b), a negligibly small deviation is observed near the rough bed, which can be due to the lack of extra layer under the main layer in our current simulation. Similarly, a small difference is found near the bottom in the Reynolds stresses between the benchmark results and our current results as shown in figure 3.26(c). The overall good comparison between these two results validate the quality of CaNS's volume penalisation implementation.

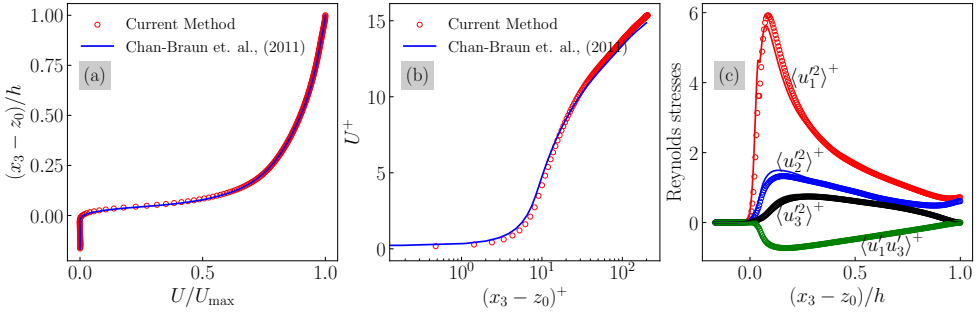


Figure 3.26: Validation of volume penalisation method in CaNS: (a) mean velocity profile in the outer unit, (b) mean velocity profile in the wall unit, and (c) Reynolds stresses. Discrete circles indicate the current method's results while the continuous lines the benchmark test results.

### 3.B Determination of virtual origin and $k_{s\infty}$

In the periodic rough-smooth channel flows (case CR2 and case CR3), the virtual origin  $z_0$  needs to be determined to further define the effective flow depth  $h = H - z_0$ , the bulk velocity based on effective depth  $U_{bh} = (1/h) \int_{z_0}^H \langle \bar{u}_1 \rangle dx_3$ ,

and the friction velocity at the rough wall  $u_{*t}$ . Here  $\langle \bar{u}_1 \rangle$  denotes the time- and horizontal-averaged velocity profile, which is a function of only the wall-normal coordinate  $x_3$ .

For the simplicity, we will assume the rough carpet lies at the origin  $x_3 = 0$ , and the smooth surface at the top  $x_3 = 0.12$ , i.e., the flipped geometry of cases CR2 and CR3. In any case,  $z_0$  is measured from the base surface of the roughness elements, therefore assuming the flipped geometry cannot make any deviation for further analysis. Moreover, we separate the vertical extent into two parts, based on the location of maximum streamwise velocity  $U_{\max}$ , and we can consider only the lower part which includes the spheres.

The virtual origin is found iteratively by fitting the shifted log-profile as shown in figure 3.27(a), resulting in the velocity shift  $\Delta U$ . The resulting  $\Delta U$  can be used to estimate the equivalent sand roughness height  $k_{s\infty}$  for high Reynolds number by applying Colebrook-type formula or fully rough regime formula [83]. Both formulae give the conclusion for case CR2 which lies near the upper limit of the transitionally rough regime, and for case CR3 which is in the fully rough regime (figure 3.27(b)).

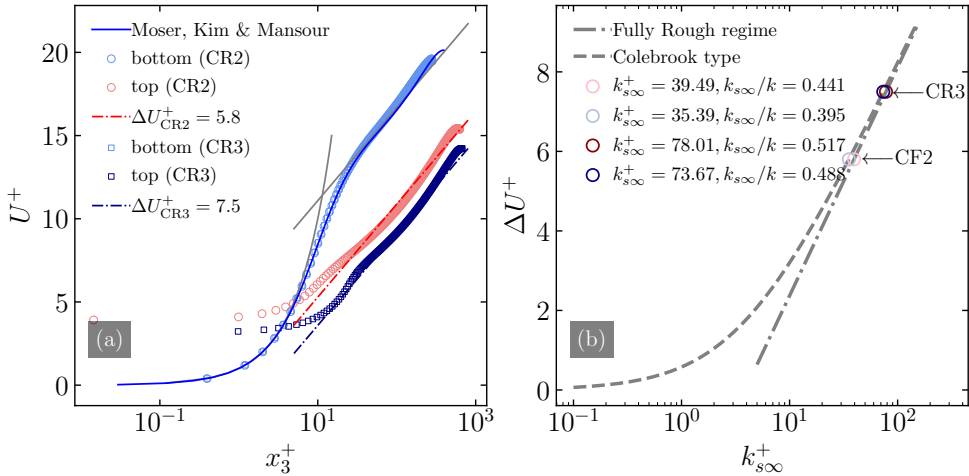


Figure 3.27: (a) Determination of virtual origin for cases CR2 and CR3 by fitting the shifted log-law profile, and (b) estimation of equivalent sand roughness for high Reynolds number using the Colebrook formula and fully rough regime formula.

### 3.C Streamwise development of turbulent normal stresses

In this appendix, we address the streamwise development of turbulent normal stresses using the inner scaling and outer scaling. The inner scaling is performed by the viscous length scale at the smooth boundary and the outer scaling is performed by the total depth and the maximum velocity of the corresponding case. Figure 3.28 illustrates the development of stress profiles immediately downstream of the tripping point and the flow is still developing at  $x_1^*/H = -40$ , compared to the benchmark result of case OS. However, when the flow approaches the transition point, the stress profiles attain the benchmark profiles of the canonical open channel flow as shown in figure 3.29.

Figures 3.30 and 3.31 show the evolution of normal stress profiles for case TS and case TR3, respectively. The flow is found still evolving toward the fully developed condition in case TS whereas the flow is observed faster to be approaching the fully developed state in case TR3. The latter case induces stronger turbulent mixing due to the larger roughness.

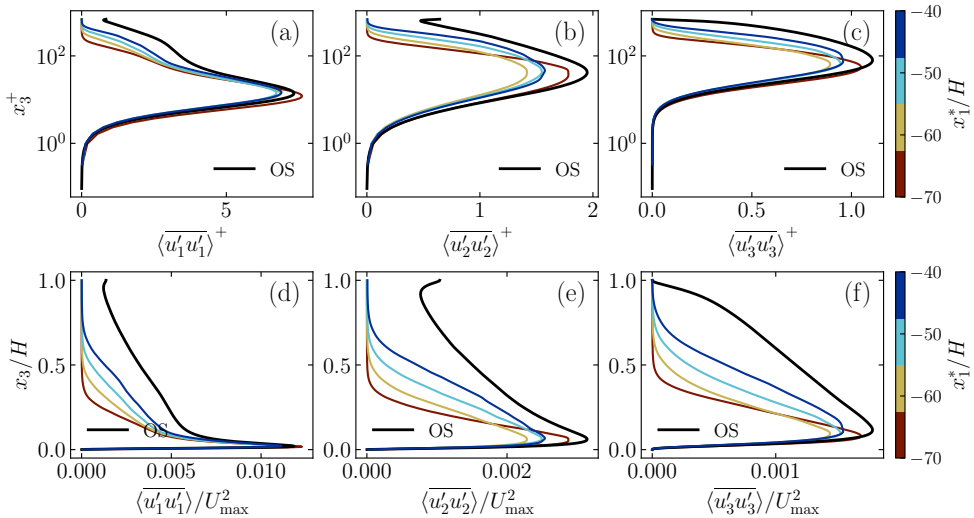


Figure 3.28: Streamwise development of turbulent normal stresses  $\langle u_i' u_i' \rangle$  immediately downstream of the tripping point for all transition cases TS, TR2 and TR3: (a,b,c) using the inner scaling, and (d,e,f) the outer scaling. The flow is observed to be developing at  $x_1^*/H = -40$ .

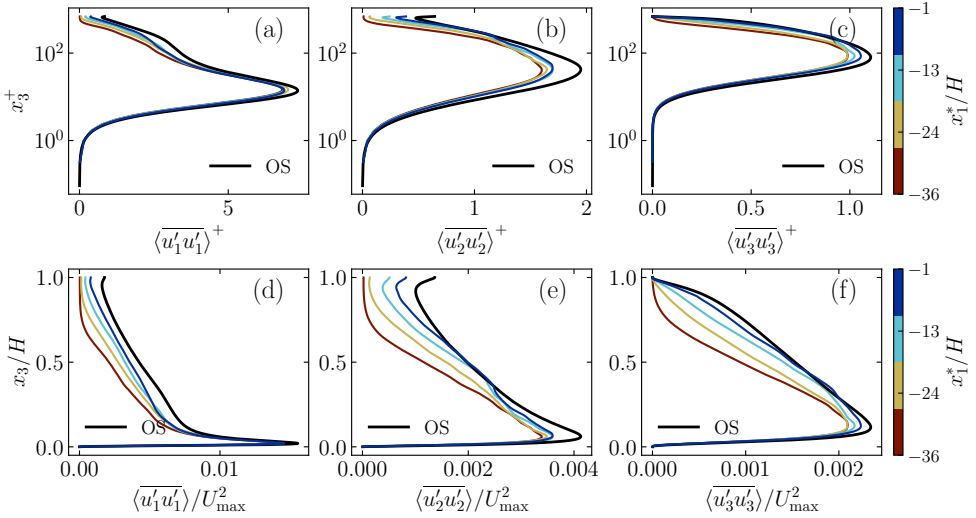


Figure 3.29: Streamwise development of turbulent normal stresses  $\langle u'_i u'_i \rangle$  immediately upstream of the flow transition for case TR2: (a,b,c) using the inner scaling, and (d,e,f) the outer scaling. The flow is observed to follow the benchmark results of case OS in the vicinity of the transition.

### 3.D Validation of case TS with Blasius profile

In case TS where a smooth carpet is introduced at the transition point, the flow encounters a hydrodynamic regime change from the open channel flow to the closed channel flow. Consequently, the flow near the free surface experiences a no-slip boundary condition of the smooth carpet, and the resulting velocity profile is found to be similar with the Blasius profile. Figure 3.32 compares the current DNS simulation result of the velocity profile and numerical integration result of Blasius profile governed by

$$2 \frac{d^3 f}{d\eta^3} + f \frac{d^2 f}{d\eta^2} = 0 \quad (3.12)$$

where  $f$  is an unknown function of  $\eta$ , and  $\eta$  denotes a transformation variable defined as  $\sqrt{U/(\nu x_1)} x_3$ . In figure 3.32, the velocity profiles are shown for the vicinity of the top boundary by using the inverted vertical coordinate system  $(H - x_3)$ , normalised by  $H$ . Development of the velocity profiles along the streamwise position  $x_1^*/H$  are shown in the subfigures of figure 3.32 and they

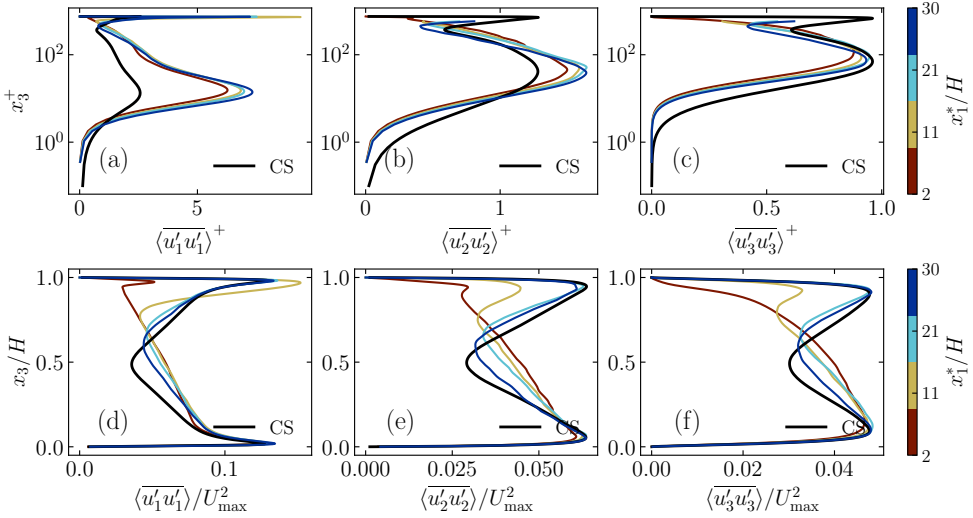


Figure 3.30: Streamwise development of turbulent normal stresses  $\langle u_i' u_i' \rangle$  downstream of the flow transition for case TS: (a,b,c) using the inner scaling, and (d,e,f) the outer scaling. The flow does not fully recover toward the benchmark closed channel case.

are observed to agree with the laminar boundary layer of Blasius profile<sup>⊙</sup>. This observation was also reflected in the discussion of  $C_f^t$  in Subsec. 3.3.2, showing that the new boundary layer developed at the smooth transition point is similar to the laminar boundary layer until the streamwise position of  $x_1^*/H = 1.2$ .

### 3.E Turbulence model of Donaldson et al. [1]

A simplified version of turbulence model developed by Donaldson et al. [1] is presented briefly to estimate the shear stress at the location of streamwise maximum velocity,  $z_m$ . Transport equation of the Reynolds shear stress  $\overline{u_1' u_3'}$  is the starting point of this turbulence model,

<sup>⊙</sup>Dr. Roshan Samuel is gratefully acknowledged for sharing the numerical code used to solve the Blasius velocity profile.

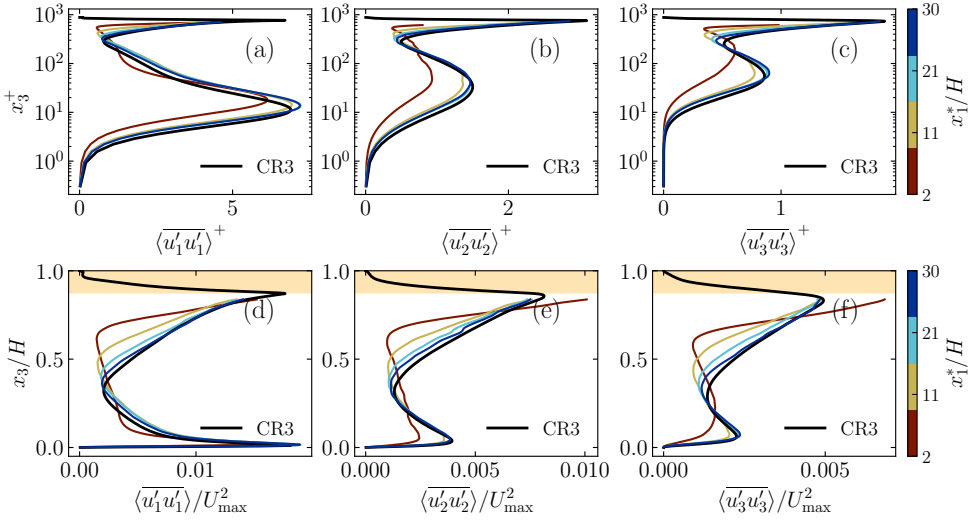


Figure 3.31: Streamwise development of turbulent normal stresses  $\langle u'_i u'_i \rangle$  downstream of the flow transition for case TR3, (a,b,c) using the inner scaling, and (d,e,f) the outer scaling. The flow recovers the profiles of benchmark case CR3 at  $x_1^*/H = 30$ . Orange-coloured area indicates the height of the roughness.

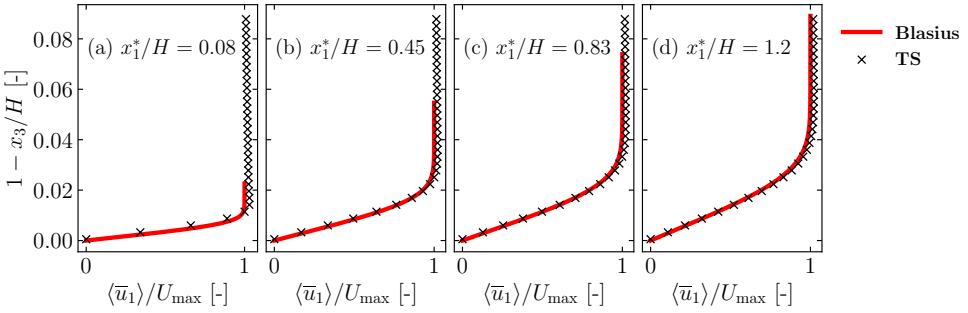


Figure 3.32: Comparison of mean streamwise velocity profile of case TS near the top boundary in the vicinity of the transition point ( $x_1^*/H = 0.58$ ) against Blasius profile. The velocity profile is shown using the inverted vertical coordinate ( $H - x_3$ ), normalised by  $H$ , such that  $1 - x_3/H = 0$  denotes the origin of the top boundary.

$$\begin{aligned} \frac{D\overline{u'_1 u'_3}}{Dt} = & -\overline{u'_3 u'_3} \frac{\partial U}{\partial x_3} + 2\Lambda_2 \frac{\partial}{\partial x_3} \left( K \frac{\partial \overline{u'_1 u'_3}}{\partial x_3} \right) + \Lambda_3 \frac{\partial}{\partial x_3} \left( K \frac{\partial \overline{u'_3 u'_1}}{\partial x_3} \right) \\ & - \frac{K}{\Lambda_1} \overline{u'_1 u'_3} + \nu \frac{\partial^2 \overline{u'_1 u'_3}}{\partial x_3^2} - 2\nu \frac{\overline{u'_1 u'_3}}{\Lambda_4^2} \end{aligned} \quad (3.13)$$

where  $\Lambda_i$  ( $i = 1, \dots, 4$ ) denote the length scales to be estimated. For the steady flow (which is similar to our periodic simulation cases CR2 and CR3), LHS of Eq. 3.13 becomes zero. The shear stress at the location of maximum velocity  $z_m$  can be calculated from the following equation

$$0 = \left[ (2\Lambda_2 + \Lambda_3) \frac{\partial K}{\partial x_3} \frac{\partial \overline{u'_1 u'_3}}{\partial x_3} - \frac{K}{\Lambda_1} \overline{u'_1 u'_3} - 2\nu \frac{\overline{u'_1 u'_3}}{\Lambda_4^2} \right]_{z_m} \quad (3.14a)$$

$$\tau_m = -\rho \overline{u'_1 u'_3} \Big|_{z_m} = \left[ -\rho \frac{2\Lambda_2 + \Lambda_3}{c} \frac{\partial K}{\partial x_3} \frac{\partial \overline{u'_1 u'_3}}{\partial x_3} \right]_{z_m} \quad (3.14b)$$

where  $c = \frac{K}{\Lambda_1} + \frac{2\nu}{\Lambda_4^2}$ , since the velocity gradient  $\frac{\partial U}{\partial x_3}$  is zero, the viscous stress is negligible at  $z_m$ , and the second derivative of the linear stress function is zero.

The model parameters of  $\Lambda_i$  ( $i = 1, \dots, 4$ ) for application to boundary layers are as follows:  $\Lambda_1 = 0.15\delta_{0.99}$ ,  $\Lambda_2 = 0.1\Lambda_1$ ,  $\Lambda_3 = 0.1\Lambda_1$ ,  $\Lambda_4 = \Lambda_1/(2.5 + 0.125Re_{\Lambda_1})^{0.5}$  where  $\delta_{0.99}$  is the thickness of the layer in which the velocity reaches 99% of free stream velocity, and  $Re_{\Lambda_1} = K\Lambda_1/\nu$  [1]. It is noted that these parameters were derived for the atmospheric boundary layer. Therefore, we applied  $\delta_{0.99} = H$  the total depth in our case.

Moreover, we can deduce the mismatch between the location of zero shear stress  $z_{\tau=0}$  and location of maximum velocity  $z_m$  by observing the signs of each term in Eq. 3.14 according to [23]. The constant term  $\rho(2\Lambda_2 + \Lambda_3)/c$  is positive by definition, and the gradient terms  $\partial K/\partial x_3$  and  $\partial \overline{u'_1 u'_3}/\partial x_3$  are also found to be positive in the location of maximum velocity  $z_m$ . Therefore, the value of  $\tau_m$  becomes negative (non-zero), and consequently,  $z_{\tau=0}$  is lower than  $z_m$ .



# 4

## Drag and lift forces on a particle in different configurations with respect to a floating carpet

“Suffering is caused by desire and grasping. There is a way out of suffering.”

— The Buddha (480 – 400 BCE)



## 4.1 Introduction

Having discussed the hydrodynamic forces acting on the spheres both at the leading edge and inside the carpet in Chapter 3, this chapter focuses on the forces acting on the individual particle located in different horizontal and vertical positions along the flume, where the flow field is modified by the presence of a floating carpet. Flow responses to the carpet, specifically flow acceleration at the transition point, flow separation underneath the carpet and additional boundary layer development at the carpet, were also investigated in Chapter 3. The complex flow response significantly will alter the forces on the particles, thereby determining whether they remain stable or become unstable to form a carpet.

The physical mechanism of particle erosion was examined in Chapter 2 using laboratory experiments and analytical considerations. Figure 4.1 presents snapshots of the erosion trajectory of the particle in the experiments of Chapter 2; panels (a) through (d) of the figure 4.1 illustrate the temporal sequence of the erosion event and particle trajectory. In this chapter, the hydrodynamic forces acting on the particle along its trajectory have yet to be determined. Based on the experimental observations (figure 4.1), a conceptual trajectory of the particle is constructed here for further analysis of hydrodynamic forces on the particle.

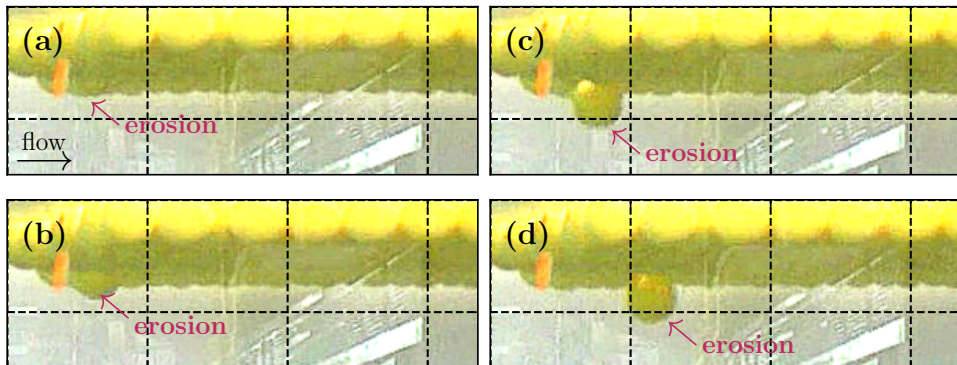


Figure 4.1: Experimental observation of the particle erosion instability and its trajectory from Chapter 2: panels (a), (b), (c), and (d) illustrate the snapshots of the particle trajectory.

Figure 4.2 illustrates the plausible trajectory of the particle along the up-

stream and downstream of the carpet. At position ① in figure 4.2, the particle is floating initially at the free surface with half of its total volume submerged. The particle is assumed to advect in the streamwise direction due to the drag force. The predicted trajectory of the particle is shown in a sequence of positions ② → ③ → ④ → ⑤ in figure 4.2. Understanding and quantifying the hydrodynamic forces acting on the particle in these different positions is still lacking, despite its importance for particle motion in the transition flow due to the carpet. As a result, the quantification of the particle forces will provide better insights in the stability of the particle, and subsequently the ultimate stability of the carpet.

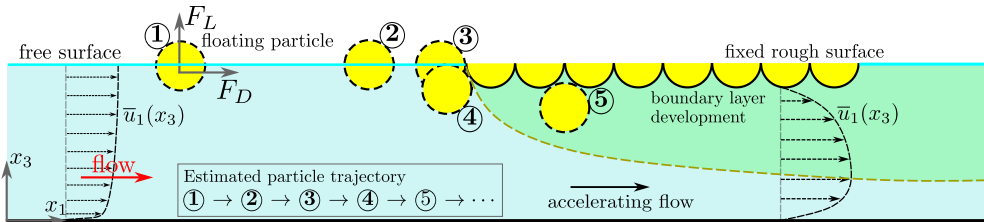


Figure 4.2: Conceptual sketch for a particle at different positions with respect to a floating carpet. A floating particle is considered to advect in the mean flow direction from position ① to ⑤ through encountering a flow transition from the open to closed channel.

The motion of a particle in a flow, or the flow past a sphere, has been a classical problem in the field of fluid mechanics and was studied analytically for small Reynolds numbers [95], experimentally [96], and numerically [96]. Adding to the complexity, the flow around a sphere located in the turbulent boundary layer differs from the flow around a sphere in a uniform flow field [39, 97], thus complicating the drag and lift forces on the sphere due to the presence of a velocity gradient of the boundary layer. Actually, the lift force on a sphere is influenced not only by the fluid shear rate but also by the rotation of the particle [98]. In our study, the flow around a fully immersed particle is studied both in the open channel and closed channel, denoted by ④ and ⑤, respectively.

As a half-immersed spherical particle is assumed in this study, the floating sphere in the open channel can be approximated as a hemisphere in the flow, as indicated by ①, ②, and ③ in Figure 4.2. Hence, it is necessary to understand the motion of a half-immersed sphere or hemisphere as well. Contrary to the shape of a sphere, a hemisphere possesses a significantly asymmetric shape, therefore complicating the prediction of its drag and lift coefficients. Kamoliddinov et al. [99] studied the drag and lift force on the half-immersed

particle by towing it in the open channel. Due to the existence of the free-surface of the flow, the free surface variation also enhances the drag coefficient due to the additional energy dissipation from the surface waves [99].

To the best of our knowledge, the quantification of drag and lift coefficients of particles affected by complex background flows, such as the transition flow induced by the floating carpet of this study, has yet to be explored, despite a vast literature on the simplified geometry and configuration such as particles in the uniform flow and particles in the turbulent boundary layer. This study therefore focuses on the hydrodynamic forces acting on a sphere located at various horizontal and vertical positions upstream and downstream of the floating carpet as detailed in figure 4.3. The research question of this chapter is three-fold:

1. How do drag and lift forces acting on the particle vary at different positions in the presence of the carpet?
2. What are the drag and lift coefficients of the sphere in the above-mentioned cases?
3. What are the implications for the stability and evolution of the carpet configuration?

Moreover, the study is expected to contribute to closing the knowledge gap in understanding the development of forces on particles in both open and closed rough channels including the flow transition. A better understanding of the evolution of hydrodynamic forces on the particle due to the carpet allows for a better informed assessment of the plastic debris capturing mechanism by the waste-collecting device, as extreme forces can dislodge and erode debris from the carpet.

## 4.2 Methods

To calculate the forces acting on the particles in the presence of the carpet as shown in figure 4.2, a floating carpet composed of half-immersed spheres is constructed in the open channel flow using the numerical method as outlined in Chapter 3. The sphere of interest is placed fixed in the computational domain at various positions such that it is found initially at the free surface with the mean streamwise velocity relative to the floating carpet as demonstrated

in figure 4.2. Due to technical limitations of our computational tool which is designed only for static particles and fast computation, the sphere does not move in real time with the flow. Instead, it is manually repositioned, which means for each new location, a corresponding mesh is generated and a new simulation is run until sufficient statistical convergence of the result is achieved. The sphere is then assumed to interact with the carpet and gradually submerge in a quasi-static manner. The realised configurations, therefore, provide insight in the forces acting on the spheres in different positions and help understanding the motion of particles and stability of the carpet.

### 4.2.1 Flow configurations

Figure 4.3 illustrates different simulation setups, showing a sphere positioned at various horizontal and vertical locations relative to the leading edge of the floating carpet, as summarized in table 4.1. The background configuration of the floating carpet and the numerical settings are consistent with those described in Chapter 3. However, the coordinate system differs from that used in the previous chapters: here, the  $x_1$ -coordinate originates at the flow transition,  $x_2 = 0$  corresponds to the middle plane of the channel, i.e., at  $0.5B$  where  $B$  is the channel width, and  $x_3 = 0$  is located at the channel bottom as shown in figures 4.3(a) and 4.3(g). The contact point between the particle and the carpet is analysed for two most likely positions: (1) an in-between position, in which the sphere is positioned between two spheres of the carpet as shown in figure 4.3(c), and (2) a head-on position, in which the sphere is in full contact with only one sphere of the carpet as shown in figure 4.3(g).

All simulations are performed using a fully developed open channel flow; therefore, they are initialized as hot-start simulations. As summarised in table 4.1, case 111 represents a floating sphere located at  $x_1 = -12d_p$  from the leading edge of the carpet. The first digit in the case number ### denotes the streamwise position of the sphere,  $x_{1p}$ , with increasing values indicating downstream locations. The second digit specifies the lateral position: a value of ‘1’ corresponds to the channel midplane ( $x_{2p} = 0$ ), while a value of ‘2’ corresponds to  $x_{2p} = -0.5d_p$  where  $d_p$  is the diameter of the sphere. The third digit denotes the wall-normal position of the sphere,  $x_{3p}$ . Case 211 corresponds to a sphere located at the streamwise position of  $x_{1p} = -6d_p$ , case 311 to a sphere at  $x_{1p} = -2d_p$ , and case 411 to a sphere at  $x_{1p} = -d_p$ . In case 511, the sphere is positioned at  $0.5d_p$  upstream of the carpet’s leading edge i.e.,  $x_{1p} = -0.5d_p$ ,

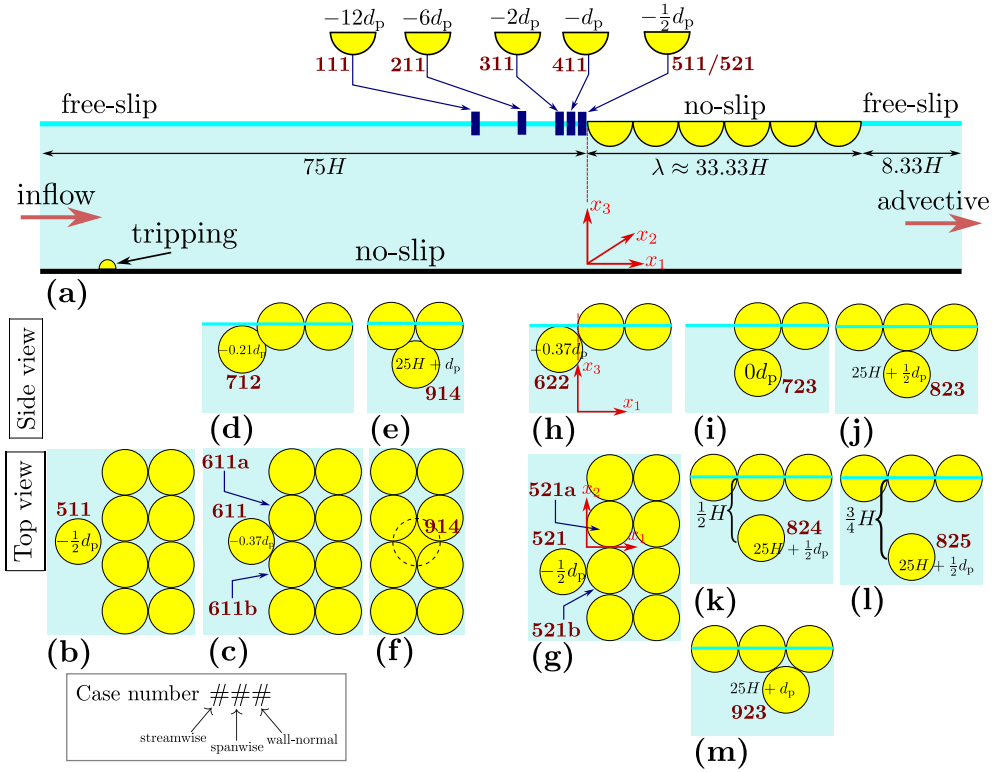


Figure 4.3: Simulation set-ups of different horizontal and vertical positions of a sphere with respect to the floating carpet. Case numbers and the coordinates of the sphere are explained in table 4.1.

leaving a small gap between the sphere and the edge. In case 611, the sphere is in contact with the first row of spheres of the carpet, positioned between two adjacent spheres at  $x_{1p} = -\left(\sqrt{3 \times 10^{-4}} - 0.01\right) / 0.02d_p \simeq -0.37d_p$  as shown in figure 4.3(c). In all aforementioned cases, the sphere is half-immersed, with its vertical position given by  $x_{3p} = H$  above the flume bottom, where  $H$  is the height of the computational domain.

Cases 611a and 611b correspond to configurations where the hydrodynamic forces are measured on the spheres located to the left and right of the case 611's sphere, respectively. These two cases investigate the influence of the case 611's sphere on the forces acting on its neighbouring spheres inside the carpet, by comparison with a reference case in which no sphere is present in front of the carpet. The sphere of case 611 is then assumed to be fully

Table 4.1: Coordinates of particle positions in emerged and submerged configurations.

Case	Emerged			Submerged			Remark
	$x_{1p}$	$x_{2p}$	$x_{3p}$	$x_{1p}$	$x_{2p}$	$x_{3p}$	
111	$-12d_p$	0	$H$	$-0.21d_p$	0	$H - 0.5d_p$	in-between figs. 4.3(e,f) submerged after <b>521</b>
211	$-6d_p$	0	$H$	$25H + d_p$	0	$H - 0.71d_p$	
311	$-2d_p$	0	$H$	$-0.37d_p$	$-0.5d_p$	$H - 0.5d_p$	
411	$-d_p$	0	$H$	0	$-0.5d_p$	$H - d_p$	
511	$-0.5d_p$	0	$H$	$25H + 0.5d_p$	$-0.5d_p$	$H - d_p$	
611	$-0.37d_p$	0	$H$	$25H + 0.5d_p$	$-0.5d_p$	0.50H	
611a	0	0.5d <sub>p</sub>	$H$	$25H + 0.5d_p$	$-0.5d_p$	0.25H	
611b	0	$-0.5d_p$	$H$	$25H + d_p$	$-0.5d_p$	$H - 0.87d_p$	
521	$-0.5d_p$	$-0.5d_p$	$H$	—	—	—	
521a	0	0.5d <sub>p</sub>	$H$	—	—	—	
521b	0	$-0.5d_p$	$H$	—	—	—	

immersed, yielding case 712 (figure 4.3(d)), where its horizontal position is slightly shifted to  $x_{1p} = -\left(\sqrt{2 \times 10^{-4}} - 0.01\right)/0.02d_p \simeq -0.21d_p$  because the sphere is in-between two spheres. The sphere was then moved to the position under the carpet where the closed channel flow is almost fully developed at  $x_{1p} = 25H + d_p$ , which results in case 914. In that case, the fully immersed sphere is in contact with four spheres of the carpet as illustrated in figure 4.3(f) and its vertical position is  $x_{3p} = H - \sqrt{2 \times 10^{-4}}/0.02d_p \simeq H - 0.71d_p$ .

We now consider the sphere of interest at the spanwise position  $x_{2p} = -0.5d_p$ , corresponding to a half-sphere diameter offset from the channel mid-plane. Case 521 denotes a case where a half-immersed sphere is in contact with only one sphere of the carpet (figure 4.3(g)). In this configuration, the sphere blocks completely one sphere of the carpet as indicated in case 521b, and its wake is thus not expected to affect the hydrodynamic force acting on the neighbouring sphere as indicated by case 521a. The sphere becomes then fully submerged in case 622 at  $x_{1p} = -\left(\sqrt{3 \times 10^{-4}} - 0.01\right)/0.02d_p \simeq -0.37d_p$  as shown in figure 4.3(h). Case 723 represents a submerged sphere that moves slightly downstream under the carpet as illustrated in figure 4.3(i), therefore its position is  $x_{1p} = 0$  and  $x_{3p} = H - d_p$ .

To further understand the hydrodynamic forces acting on the sphere in the fully developed closed channel flow under the carpet, in case 823 the sphere is positioned at  $x_{1p} = 25H + 0.5d_p$  and  $x_{3p} = H - d_p$  such that the sphere is located under the sphere of the carpet as shown in figure 4.3(j). The sphere is then positioned vertically downwards to  $x_{3p} = 0.50H$  in case 824, and to  $x_{3p} = 0.25H$  in case 825, respectively to study the effect of different velocity gradients on the hydrodynamic force. Moreover, the sphere of case 823 is moved slightly in streamwise direction to  $x_{1p} = 25H + d_p$  for case 923 which is in-between the spheres of the carpet as shown in figure 4.3(m).

## 4.2.2 Numerical methods

To implement the flow configurations as discussed in Subsec. 4.2.1, a set of numerical simulations is performed using Direct Numerical Simulations (DNS). Incompressible Navier-Stokes equations are solved numerically using CaNS solver [75] coupled with volume penalisation method for rough surface boundary condition as mentioned in the previous chapter. A complete set of gov-

governing equation reads

$$\frac{\partial u_i}{\partial t} + \frac{\partial u_i u_j}{\partial x_j} = -\frac{1}{\rho} \frac{\partial p}{\partial x_i} + \nu \frac{\partial^2 u_i}{\partial x_j \partial x_j} + F_i, \quad (4.1a)$$

$$\frac{\partial u_i}{\partial x_i} = 0, \quad (4.1b)$$

where  $u_i$  denotes the  $i^{\text{th}}$  component of the velocity vector,  $p$  the kinematic pressure,  $\nu$  the kinematic viscosity of the fluid, and  $F_i$  the volume penalisation force arising from the enforcement of velocity boundary condition on the surface of the particle. An advantage of the volume penalisation method is to obtain directly the fluid-particle interaction force via the volume penalisation force  $F_i = (v_i - u_i)/\Delta t$  where  $v_i$  is the velocity at the particle boundary ( $v_i = 0$  for the stationary particle). Therefore, the drag force  $F_D$  acting on the particle is calculated as

$$F_D = \int_{V_p} F_1(\mathbf{x}) dV \quad (4.2)$$

where  $V_p$  denotes the volume of the particle,  $\mathbf{x}$  the position vector,  $dV$  is the differential volume and  $F_1$  denotes the streamwise component of the volume penalisation force. Similarly, the lift force  $F_L$  acting on the particle is calculated as

$$F_L = \int_{V_p} F_3(\mathbf{x}) dV \quad (4.3)$$

where  $F_3$  is the wall-normal component of volume penalisation force. In the present simulation, since the particles are fixed in the computational domain, the velocity is set to zero at the boundary of and inside the particle.

In all numerical simulations of this study, a uniform velocity profile is imposed at the inlet of the computational domain and the turbulence is triggered using the tripping mechanism as shown in figure 4.3(a) as in Chapter 3. A floating carpet with a no-slip boundary condition is introduced at  $x_1 = 75H$ , after providing sufficient space for the development of fully turbulent open-channel flow. A free-slip condition is imposed at the free surface under the rigid-lid assumption. At the outlet of the channel, a Neumann boundary condition is applied, while periodic boundary conditions are imposed at both of the channel sides.

Averaging of the particle forces such as  $F_D$  and  $F_L$  is performed in time and denoted by the overline above the quantity such as  $\overline{F_D}$  and  $\overline{F_L}$ , respectively. However, the flow quantities such as the mean flow velocity  $\langle \bar{u}_i \rangle$  and

Reynolds stresses  $\overline{\langle u'_i u'_j \rangle}$  are obtained by averaging the primitive quantities in time and spanwise direction where periodic boundary conditions apply, as performed in Chapter 3.

## 4.3 Results and Discussion

In this section, we present the hydrodynamic forces i.e., streamwise-directed drag force, lateral force, and vertical-directed lift force on the particle in different positions in table 4.1 and figure 4.3. Drag coefficients  $C_D$  and lift coefficients  $C_L$  for these different configurations are discussed and compared with literature study. Moreover, probability density functions (pdf) of the forces are presented, discussing the occurrence of the extreme values depending on the particle's position. Finally, the power density spectrum of the forces are explored to study vortex shedding phenomena around the spheres.

### 4.3.1 Drag and lift forces

#### Particles at $x_2 = 0$

Drag force  $F_D$  is the horizontal component of the hydrodynamic force acting on the particle, and lift force  $F_L$  is the vertical component of the hydrodynamic force on the particle. The forces are calculated by integrating the volume penalisation forcing over the volume of the particle as explained in Eq. 4.2 and Eq. 4.3. Figure 4.4(a) shows the drag force and figure 4.4(b) the lift force acting on the particle located in the midplane of the channel  $x_2 = 0$ , respectively. Large fluctuations are found in  $F_D$  for the fully-submerged sphere of case 712 and case 914, but not in the emerged cases as indicated in figure 4.4(a). This is because in case 712, the sphere is affected by the flow transition where separation occurs under the carpet, and in case 914, the sphere is located under the rough carpet where large horizontal fluid motions can occur. It should be noted that the mean drag force on the particle of case 712 is much larger than that of case 914 although both cases are fully-submerged situations, because case 712 represents the flow acceleration at the transition, whereas case 914 represents a fully developed flow condition under the carpet. It is noted that the accelerating flow in case 712 is associated with a pressure gradient. The force is therefore composed of drag and pressure gradient contributions. As

there is less acceleration further downstream in case 914, the particle mainly experiences a drag force.

Regarding the lift force  $F_L$  on the particle in figure 4.4(b), larger fluctuations and a larger mean force are observed in case 712 where the flow separation and downward vertical flow occur at the transition point. Therefore, in all cases except case 712, the fluctuations of  $F_L$  are negligible, as the particle is located in the positions where vertical flow and flow separation are not significant. Moreover, as the particle in case 712 is affected by downward acceleration at the flow transition, the particle experiences a significant downward lift force as shown in figure 4.4(b).

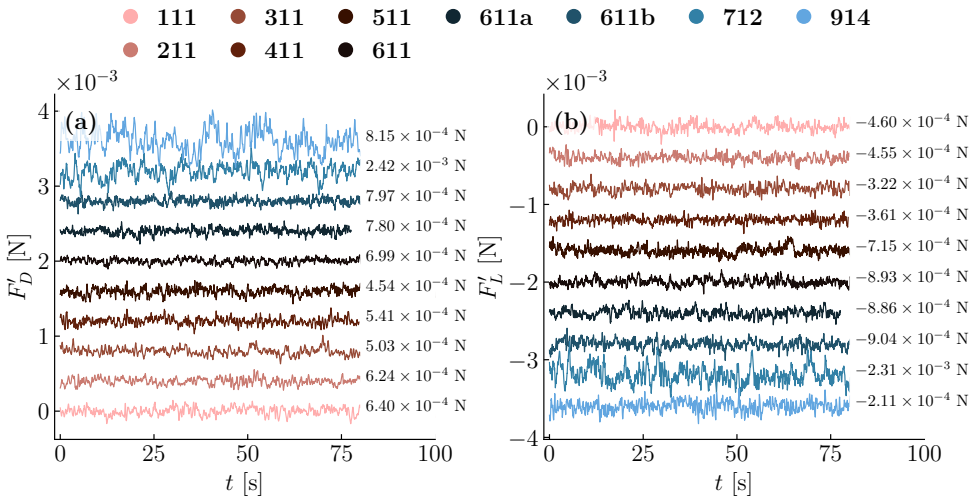


Figure 4.4: Hydrodynamic forces acting on the particle at the midplane of the channel  $x_2 = 0$ : (a) drag force and (b) lift force (negative sign in the vertical axis denotes the downward direction of the force.).

Figure 4.5 summarises the observations of hydrodynamic forces, including spanwise-directed force  $F_S$ , acting on the particle, where the marker denotes the mean force and the whiskers indicate five times the standard deviation as obtained from the time series. The benchmark data, which is obtained from case TR2 of Chapter 3 that does not consist of any additional isolated particle other than a floating carpet, is also added in figure 4.5 to compare with the forces of case 611a and case 611b. Cases 611a and 611b correspond to the configurations in which half of the sphere is blocked upstream by the sphere in case 611. In figures 4.5(a), 4.5(b) and 4.5(c), the mean forces on the

half-submerged particle is nearly identical for cases 111, 211, 311, 411, 511, and 611. As a result of the partial blockage in cases 611a and 611b, their mean drag and lift forces are slightly smaller than that in the benchmark case without upstream blockage as shown in figures 4.5(a) and 4.5(c). This partial blockage also affects the spanwise force  $F_S$  on the particle in cases 611a and 611b where the negative and positive mean forces are observed, respectively, while the benchmark case is zero as shown in figure 4.5(b).

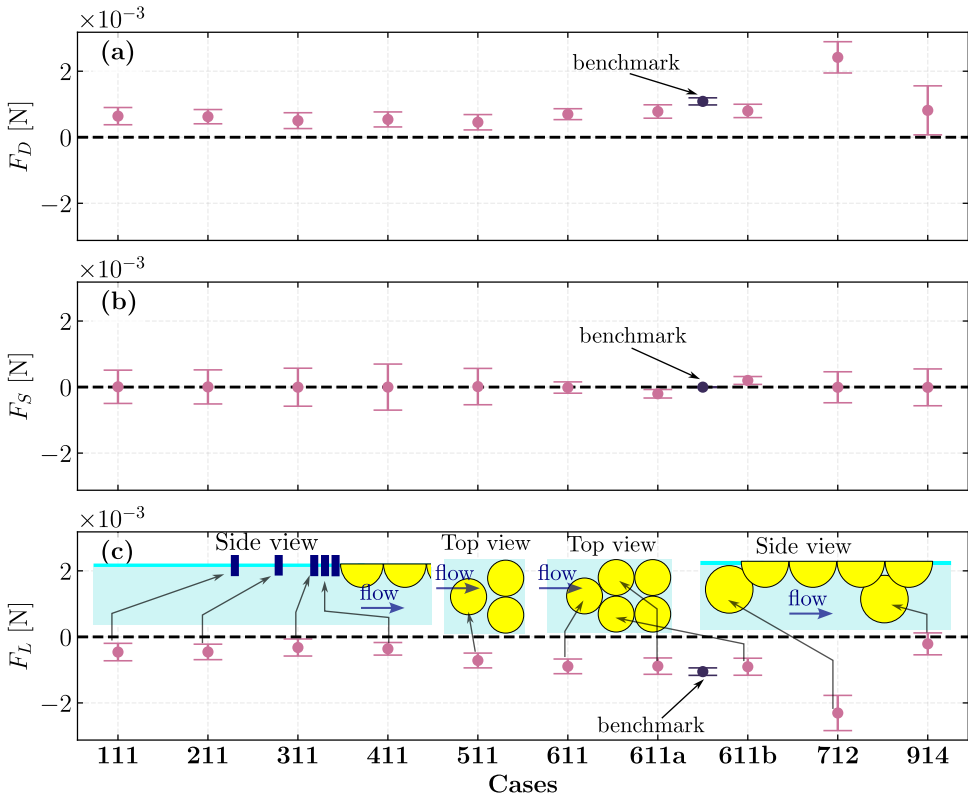


Figure 4.5: Hydrodynamic forces acting on a particle in the midplane of the channel  $x_2 = 0$ : (a) drag force  $F_D$ , (b) spanwise-directed force  $F_S$ , and (c) lift force  $F_L$ . In each panel, the circle denotes the mean value of the force, and the horizontal lines denote five times the standard deviation force.

For the submerged case 712, relatively higher mean drag and lift forces are found to act on the particle with larger fluctuations because of flow separation and flow acceleration at the transition. In case 914, the mean drag on the particle is slightly larger than the force in cases 611a and 611b as indicated in

figure 4.5(a). It is also noted that the lift force in case 914 is relatively small compared to other cases because of its particular location which is shielded by two spheres of the carpet as shown in figures 4.3(e) and 4.3(f). This means that the particle trapped inside the void of the carpet experiences weaker hydrodynamic forces, resulting in a more stable condition, compared to the sphere of case 712 at the transition.

Figures 4.6 presents p.d.f.'s of the fluctuating drag force  $F'_D$  and lift force  $F'_L$  components, together with the mean drag force  $\mu$ , the standard deviation  $\sigma$ , and the skewness parameter  $\gamma$ , shown in each panel for the corresponding cases. The solid line in each panel of figure 4.6 shows a standard Gaussian curve with  $\mu = 0, \sigma = 1$ , and  $\gamma = 0$ . As expected, case 712 exhibits larger skewness for drag and lift forces because of its asymmetry in configuration, while most cases do not show significant skewness in their p.d.f.'s (figure 4.6). Note that case 914 shows the opposite skewness in  $F'_D$  from other cases 111, 511, 611, and 712 which have the same order of magnitude of  $\gamma$ . This can be attributed to its particular position where a flow separation occurs inside the void of the carpet, thus leading to more frequent occurrence of the negative  $x_1$ -direction force on the particle of interest.

We proceed the force analysis with the auto-correlation function to better understand the temporal relation between the particle response time and fluid motions. Auto-correlation functions for the general quantity  $\theta$ ,  $R_{\theta\theta}(k)$ , are calculated as follows,

$$R_{\theta\theta}(k) = \overline{\theta'(t)\theta'(t+k)} \quad (4.4)$$

where  $k$  is the time shift. Figure 4.7 describes the auto-correlation function for fluctuating components of hydrodynamic forces  $F'_D, F'_S$  and  $F'_L$  acting on the particle at  $x_2 = 0$  using the non-dimensional shift parameter  $\psi = kU_b/d_p$ . It is noted that in figure 4.7, Eq. 4.4 is normalised by the values at zero shift  $R_{\theta\theta}(0)$ . Periodic patterns are observed in spanwise force  $F'_S$  for cases 111, 211, 311, and 411 in figure 4.7(b), which suggests vortex shedding around the sphere. The solid vertical lines in figure 4.7(c) denote the non-dimensional period of the oscillation  $\psi = 5.4$  and  $\psi = 5.8$ , which is the inverse of Strouhal number  $St = fd_p/U_b$  where  $f$  is the frequency of the vortex shedding, yielding  $St = 0.185$  and  $St = 0.172$ , respectively.

Moreover, power density spectrum analyses of the force signals also confirm this observation through the peaks in accordance with corresponding Strouhal numbers,  $St = 0.185$  and  $St = 0.172$ , as indicated in figure 4.8(b). This observation was also reported by Zeng et al. [39] who studied the turbulent flow around a sphere for  $St = 0.11$  and  $St = 0.203$ . It is noted that such a

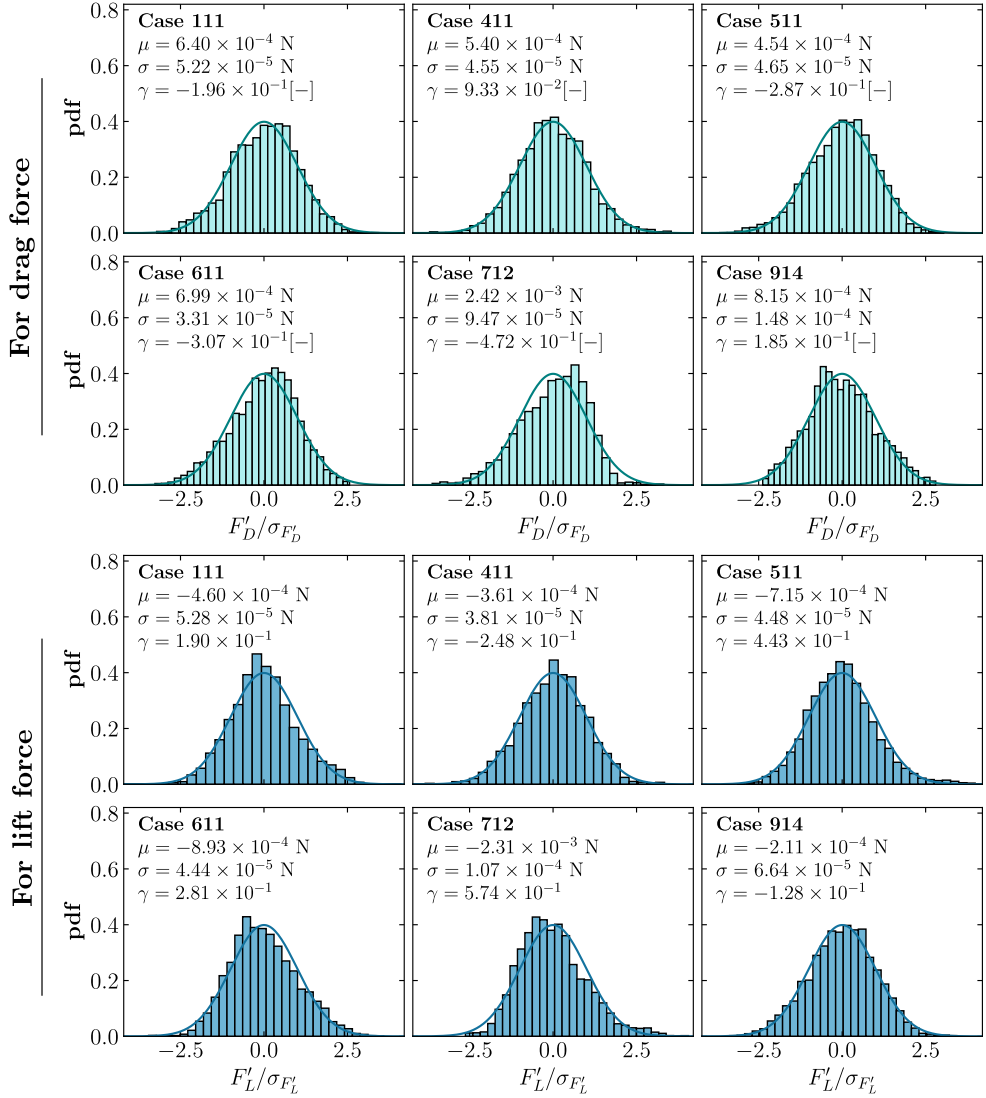


Figure 4.6: Probability density functions (p.d.f.'s) of drag force fluctuations  $F'_D$  and lift force fluctuations  $F'_L$  acting on the particle located at the midplane of the channel  $x_2 = 0$ . In each panel of the figure, the mean drag force  $\mu$ , the standard deviation of the drag force  $\sigma$ , and the skewness parameter  $\gamma$  are presented for each corresponding case. The solid line in each panel shows the Gaussian curve.

vortex shedding is not observed in the streamwise and wall-normal directions

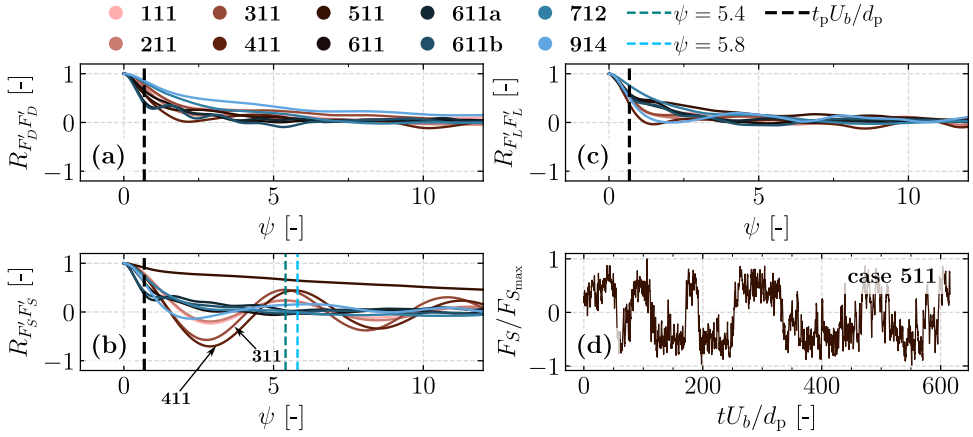


Figure 4.7: Auto-correlation functions for fluctuating components of (a) drag force  $F'_D$ , (b) spanwise-directed force  $F'_S$ , and (c) lift force  $F'_L$ , for the particle at  $x_2 = 0$ , and (d) time series of spanwise force  $F_S$  signals exhibiting a very low frequency flapping motion of case 511. The vertical solid lines represent the non-dimensionalised period of the oscillation, which is the inverse of Strouhal number  $St$ . The vertical dashed line shows the particle response time  $t_p$  normalised by bulk velocity  $U_b$  and particle diameter  $d_p$ . In panel (d) the force signals are normalised by the maximum force signal of  $F_S$ .

because of the lack of the symmetry. Even in the spanwise direction, some cases do not show the vortex shedding phenomenon, especially in the vicinity of the carpet, since the presence of the carpet affects the wake and breaks down the vortex shedding. Remarkably, the sphere in case 511 shows a very large auto-correlation time of the spanwise force  $R_{F'_S F'_S}$  in figure 4.7(b), which is due to a very low frequency mode observed in the time series of the force signals as shown in figure 4.7(d). In fact, the sphere wake in case 511, which is located very close to the carpet but still separated by a small gap, exhibits a low frequency flapping motion in the spanwise direction. This behavior arises from its particular position, where the influence of the carpet is predominant and the downward flow also plays an important role.

#### Particles at $x_2 = -0.5d_p$

This section focuses on hydrodynamic forces acting on the particle in the vertical plane parallel to  $x_1$ -direction, which is located half a diameter away from the midplane, i.e., at  $x_2 = -0.5d_p$ . Figures 4.9(a), 4.9(b) and 4.9(c) show the hydrodynamic forces  $F_D$ ,  $F_S$  and  $F_L$ , acting on the particle, respectively.

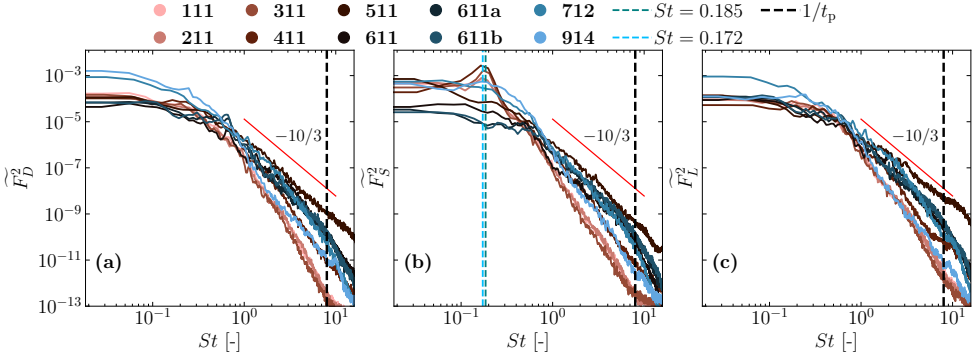


Figure 4.8: Power density spectra (PSDs) for (a) drag force  $F_D$ , (b) spanwise-directed force  $F_S$ , and (c) lift force  $F_L$  using Welch's method. The vertical axis is non-dimensionalised by  $(0.5\rho U_b^2 A_p)^2$ . Peaks in the spectrum indicate the frequency of vortex shedding in the spanwise direction.

The mean values of the forces are indicated by markers, while the whiskers represent five times the standard deviation in figure 4.9. The drag and lift forces on the particle in case 521 is slightly smaller than in cases 521a and 521b, in which the particles are located within the carpet because the spheres inside the carpet do not have the lateral space for the flow to pass and effectively form, together with neighbouring particles, a sort of cylindrical leading edge (figures 4.9(a) and 4.9(c)). Absence of lateral spacing pushes the flow to pass only beneath the carpet sphere, unlike the case of an isolated sphere.

The force fluctuations in case 521a are found to be larger than the fluctuations of case 521b which is shielded completely by the particle in case 521 as shown in figures 4.9(a) and 4.9(c). Blockage by the upstream particle influences the particle in case 521b, resulting in the reduction of the lift force  $F_L$ , compared to the case 521a (figure 4.9(c)) where the streamlines can reach the sphere directly. The submerged sphere in case 622 and case 723 experiences larger drag and lift forces because of flow acceleration at the transition point. It is noted that the submerged sphere in case 712 has a configuration almost identical to case 622, except the lateral position of the particle. However, the forces acting on the particle in case 712 (figure 4.5) are slightly larger than in case 622 (figure 4.9) because the particle in case 712 is located inside the gap between two spheres of the carpet as shown in figure 4.3(d), where higher flow velocity can occur.

The analysis proceeds with the sphere in the position of the fully developed closed flow at  $x_1 = 25H + 0.5d_p$ . The sphere directly under the carpet

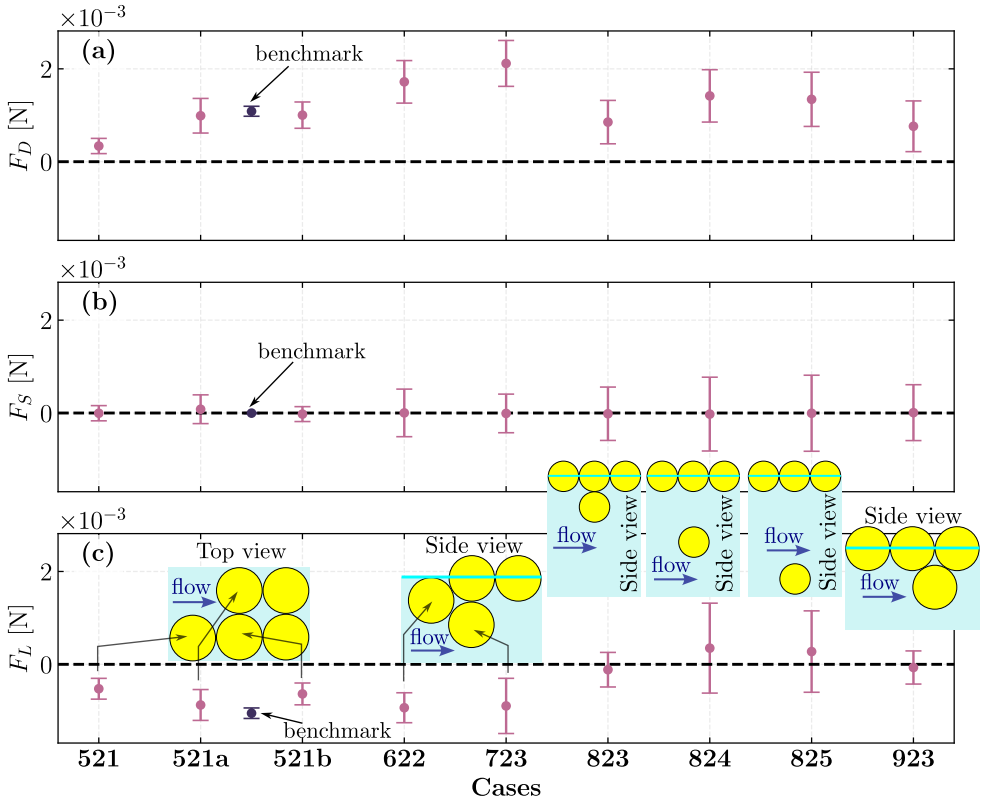


Figure 4.9: Hydrodynamic forces acting on a particle in the plane of  $x_2 = -0.5d_p$ : (a) drag force  $F_D$ , (b) spanwise-directed force  $F_S$ , and (c) lift force  $F_L$ . In each panel, the marker denotes the mean value of the force, and the whiskers denote five times the standard deviation as obtained from the force time series.

in case 823 shows relatively smaller hydrodynamic forces  $F_D$  and  $F_L$  than the spheres located at  $x_3 = 0.50H$  in case 824 and  $x_3 = 0.25H$ , which are located near the point of maximum velocity (figures 4.3(k) and 4.3(l)), respectively. As expected, the drag and lift forces are larger in cases 824 and 825 than those in case 823. It is also noted that lift forces in cases 824 and 825 act upward, in contrast to other cases in which the sphere is subjected to a negative velocity gradient near the carpet [98].

Figure 4.10 shows the p.d.f.'s of the fluctuations of drag and lift forces acting on the particle at  $x_2 = 0.5d_p$ , respectively, for cases 622, 723, and 923. As expected, the force signals show large skewness for cases 622 and

723, where the particle is located at the transition, where the flow pattern is asymmetrical. For case 923 in the fully developed closed channel flow, the acting force signals show a Gaussian distribution for the lift force (lower panel of figure 4.10) whereas a slightly positive-skewed distribution is observed in the drag force (upper panel of figure 4.10).

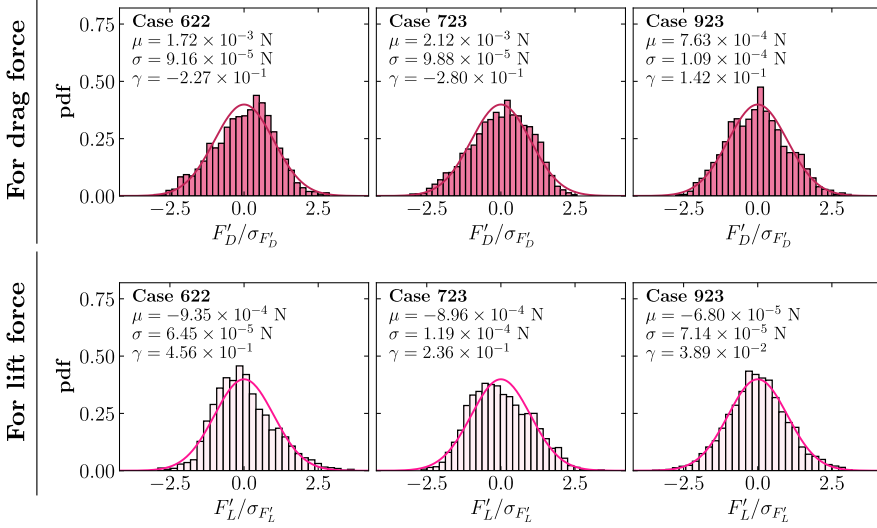


Figure 4.10: P.d.fs of drag force fluctuations  $F'_D$  and  $F'_L$  on the particle located at  $x_2 = -0.5d_p$  for cases 622, 723, and 923. In each panel of the figure, the mean drag force  $\mu$ , the standard deviation of the drag force  $\sigma$ , and the skewness parameter  $\gamma$  are presented for each corresponding case. The solid line in each panel shows the Gaussian curve.

### 4.3.2 Drag and lift coefficients

This section will discuss the drag and lift coefficients calculated as

$$C_D = \frac{F_D}{0.5\rho U_b^2 A_{\text{corr}}} \quad (4.5)$$

and

$$C_L = \frac{|F_L|}{0.5\rho U_b^2 A_p}, \quad (4.6)$$

respectively, where  $U_b$  denotes the bulk velocity and  $A_{\text{corr}}$  the corresponding projected area of the particle such that  $A_{\text{corr}} = A_p$  for the fully submerged

particle, and  $A_{\text{corr}} = 0.5A_p$  for the half-submerged particle. Noted that  $A_p$  is used for both emerged and submerged cases in Eq. 4.6 because the lift force is acting the particle vertically and the projected area becomes the complete cross-sectional area of the particle. Numerical results are compared with analytical predictions of Yan Toe et al. [63] (Chapter 3) and the literature results. Yan Toe et al. [63] developed an analytical framework (Eq. 3.11) to predict forces responsible for particle erosion at the leading edge of the carpet. Figure 4.11 shows the force coefficients along the streamwise  $x_1$  direction in terms of particle diameter  $d_p$  for all simulated cases.

Results for different configurations (figure 4.11) are represented by the different colours such that ( $\bullet$  **E**, **M**) for ‘**E**merged and **M**id-plane position’ cases, ( $\color{magenta}\bullet$  **E**, **O**) for ‘**E**merged and **O**ff-plane  $x_2 = -0.5d_p$  position’ cases, ( $\color{cyan}\bullet$  **S**, **M**) for ‘**S**ubmerged and **M**id-plane position’ cases, and ( $\color{magenta}\bullet$  **S**, **O**) for ‘**S**ubmerged and **O**ff-plane position’ cases. Drag coefficients of the emerged spheres far upstream of the carpet can be considered as the hemi-sphere at the free surface as in the experiment of Kamoliddinov et al. [99], and the numerical result of  $C_D$  agrees with the experimental result denoted by (— FK2021) for the **E**, **M** cases as shown in figure 4.11(a). For the emerged sphere touching with the carpet ( $\color{magenta}\bullet$ ), its drag coefficient is observed to be smaller than the drag coefficient of isolated emerged spheres ( $\bullet$ ). As for the lift coefficient, Kamoliddinov et al. [99] derived  $C_L = 11/16$  assuming the validity of the potential flow theory, and it is found to be much higher than the numerical results (figure 4.11(b)). Once the emerged sphere approaches the carpet at  $x_1 = -0.5d_p$ , it experiences a larger vertical force, resulting in a larger lift coefficient  $C_L$  in figure 4.11(b), compared to cases upstream of this position.

Near the leading edge of the carpet at  $x_1 = -0.37d_p$ , the submerged sphere with  $x_2 = -0.5d_p$  ( $\color{magenta}\bullet$ ) experiences a relatively larger drag than emerged sphere ( $\bullet$ ), both of which are different from Yan Toe et al. [63]’s analytical predictions of  $C_D$  denoted by — and - - - (figure 4.11(a)). As for the lift force coefficient (figure 4.11(b)), numerical results  $C_L$  of both submerged spheres ( $\color{magenta}\bullet$ ) and emerged spheres ( $\bullet$ ) agree with analytical result of submerged cases (—). The analytical value  $C_L$  for the emerged sphere (- - -) is found lower than the numerical result  $C_L$  ( $\bullet$ ). For the submerged particle near the leading edge at  $x_1 = -0.21d_p$  with  $x_2 = 0$  ( $\bullet$ ), the numerical results of  $C_D$  and  $C_L$  are observed to be different from the analytical predictions. These observations suggest that the analytical formula of Yan Toe et al. [63] can predict only the *lift force* acting on the *submerged* particle at the leading edge with  $x_2 = -0.5d_p$ , thus necessitating modifications for more general cases. For instance, it was simply

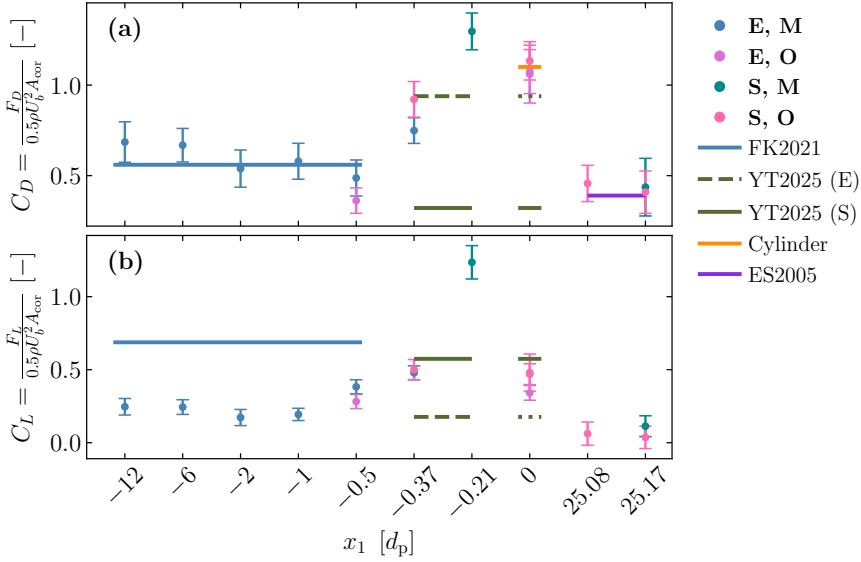


Figure 4.11: Variation of (a) drag coefficient  $C_D$  and (b) lift coefficient  $C_L$  with the stream-wise direction  $x_1$  in terms of particle diameter  $d_p$ . ● for ‘emerged and mid-plane’ cases, ● for ‘emerged and off-plane  $x_2 = -0.5d_p$ ’ cases, ● for ‘submerged and mid-plane’ cases, and ● for ‘submerged and off-plane’ cases.

assumed  $C_D = 0.5$  in the calculation of the analytical force  $F_L$  (Eq. 3.11) whereas  $C_D$  is found to be larger than 0.5 for these particle positions  $x_1 = -0.21d_p$ , and  $-0.37d_p$  as shown in figure 4.11(a).

At the leading edge of the carpet  $x_1 = 0$ ,  $C_D$  of the emerged sphere inside the carpet (●) agrees with  $C_D$  of a cylinder as found in [34] because the sphere inside the carpet mimics together with neighbouring particles, effectively a cylindrical obstacle to the flow. Analytical prediction of its  $C_D$  does not agree with the numerical result whereas in comparison of  $C_L$  these two results agree reasonably (figure 4.11(b)).

For the spheres submerged at the fully developed condition of the closed channel at  $x_1 = 25.08d_p$  and  $x_1 = 25.17d_p$  (● and ●), the numerical result of  $C_D$  is found to be equivalent to the literature result of  $C_D$  of the sphere (— ES2005 [34]). The lift coefficient  $C_L$  for these orientations is found to be relatively small, compared to the aforementioned cases such as the particle upstream of the carpet and at the transition point. Literature results for these configurations are not available for the comparison.

## 4.4 Conclusions

This chapter explores to better understand the variation of hydrodynamic forces acting on the particle at different configurations with respect to the floating carpet. The results are compared to literature results and analytical prediction of Yan Toe et al. [63] for the particle located at the leading edge of the carpet.

A half-immersed sphere which is far upstream or downstream of the carpet shows a constant mean drag force and lift force, being independent of the horizontal position. A particle near the leading edge of the carpet experiences a relatively large downward force (or negative lift force) due to flow contraction at the transition point, therefore being very vulnerable to particle erosion. Moreover, due to flow separation at this location, the particle also experiences extreme fluctuation forces, which can also trigger the erosion. Vortex shedding, commonly occurring in flows past a sphere, is also observed around the emerged sphere far upstream of the carpet. However, the vortex shedding no longer occurs for the particle in the vicinity of the carpet, which leads to more unpredictable irregular force fluctuations.

Numerical results of drag coefficients for half-immersed spheres and fully submerged spheres, which are far upstream and downstream of the carpet, show a good agreement with experimental results of Kamoliddinov et al. [99] and literature [34], respectively. In the vicinity of the edge of the carpet, numerical results are compared to the prediction of Yan Toe et al. [63], which shows a reasonable agreement for one case which is the result of  $C_L$  for the submerged sphere at  $x_2 = -0.5d_p$ . To improve the predictability of analytical formula of Yan Toe et al. [63] for cases near the carpet's leading edge i.e.,  $x_1 = 0$  or  $x_1 = -0.21d_p$ , the drag coefficient of the sphere should be increased instead of the common value of 0.5 in Eq. 3.11 since the carpet influences the flow behaviour around the particle. Moreover, the contribution of pressure fluctuation forces in Eq. 3.11 should also be increased since the standard deviation of forces from numerical simulations is found approximately five times larger than the fluctuation force suggested based on analytical consideration.

Spheres located in the position of a fully developed flow underneath the carpet show smaller drag and lift forces, where the spheres of interest are shielded around the spheres of the carpet. Therefore, these shielded particles are less vulnerable to particle erosion compared to the particles at the flow transition. However, it should be noted that the squeezing (cumulative com-

pressive) force on the particle at the fully developed position (case 914) can enhance the erodibility of the shielded particle because a squeezed particle can push the particle below it further downward. Therefore, obtaining a better estimate of the squeezing force also requires accurately quantifying the drag force or drag coefficient acting on the particles in the upstream region. Obviously, a simulation with freely moving particles can provide this information.



# 5

## Conclusion and Outlook

“I was taught at school that you should never start a sentence without knowing the end of it.”

— Paul Adrien Maurice Dirac (1902 – 1984)



## 5.1 Conclusion

Plastic debris pollution has negative impact on ecology, health and the environment, as presented in Chapter 1. Hence, removal of plastic debris from rivers is an essential step to prevent them from reaching the ocean and to limit marine pollution. Plastic debris can be removed from rivers by installing waste-collection devices that capture the floating debris through accumulation formation. If not captured by these devices, floating debris can reach hydraulic structures such as flood gates and culverts where clogging occurs, enhancing urban flooding and structural damage of the infrastructures. Therefore, understanding of the physical processes that govern debris accumulation plays a key role in waste-collection campaigns and in the design of more efficient infrastructures. In this context, this research endeavours to obtain a fundamental insight in (1) stability of the single-layer accumulation, (2) hydrodynamic responses in the channel due to the accumulation layer, and (3) impacts of the accumulation on the hydrodynamic forces acting on single particles.

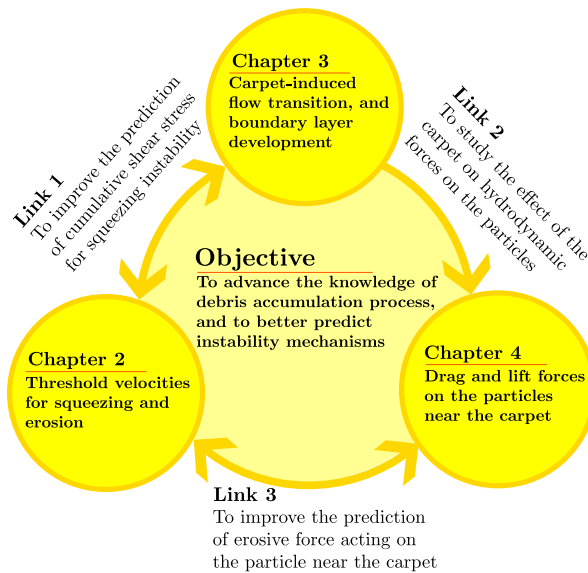


Figure 5.1: Summary of the thesis illustrating the main topic of Chapter (2), Chapter (3) and Chapter (4), and their linkages.

Chapter 2 addressed the physical mechanisms of debris accumulation at hydraulic structures using laboratory experiments, and developed an analyt-

ical framework to predict the threshold flow velocities that trigger two instability modes: (1) squeezing in figure 5.2(b), and (2) erosion (Eq. 2.19) in figure 5.2(a). Squeezing instability of the carpet was defined as the particles pushed out of the carpet due to the cumulative compressive force of the fluid shear force, and the threshold flow velocity was estimated analytically by Eq. 2.11. Squeezing instability affects a particle inside the carpet which transfers the particle-particle interaction forces. This instability is analogous to the buckling phenomenon of linear force chains studied by Winkelmann et al. [17], where compressive force plays an important role along the carpet. Misalignment angle  $\theta$ , due to turbulent fluctuations, transforms the horizontal shear stress into a vertical downward force onto the particle. The net buoyancy force  $F_b - F_g$ , or restoring force, of the particle balances the downward destabilising force. Therefore, the length of the carpet  $\lambda$  mainly determines the cumulative force  $F_c$  acting on the particle within the carpet, and subsequently its threshold flow velocity  $U_{b,c}$ .

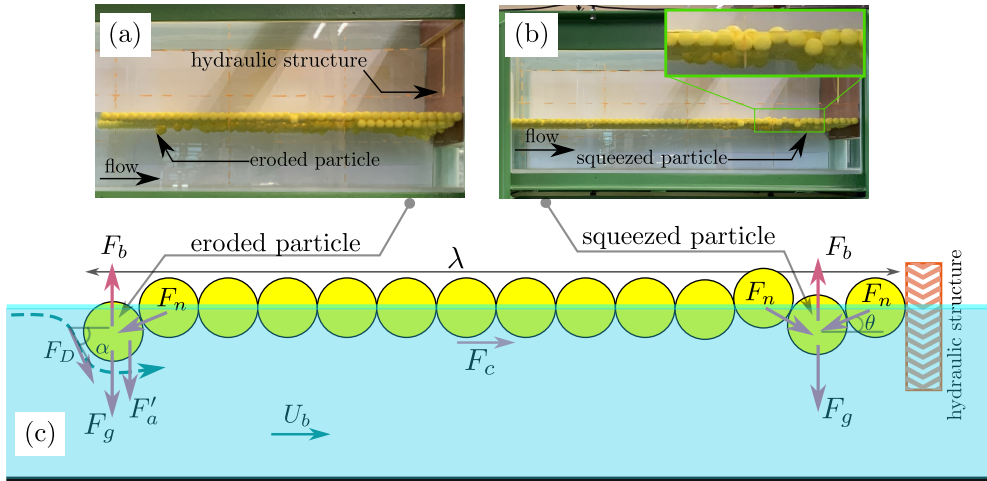


Figure 5.2: Instabilities of the carpet layer: (a) experimental observation of *erosion* of the particle, (b) experimental observation of *squeezing* instability, and (c) conceptual sketch of two instability mechanisms and the involved driving forces and restoring forces.

Moreover, experimental measurement of velocity profiles showed the stream-wise development of velocity profiles upstream and downstream the carpet. The flow transition occurs to the floating carpet from the open to closed channel via an additional boundary layer development at the carpet. Once the flow reaches the fully developed condition under the carpet, an asymmetric velocity profile was observed due to the roughness differences between the top

carpet and the bottom of the flume, which differs from the symmetric velocity profile in a simple closed channel flow.

In determining  $U_{b,c}$  with Eq. 2.11 in Chapter 2, the friction coefficient of the carpet  $C_f^t$ , experimentally obtained from the fully developed flow condition, was applied along the carpet, and drag coefficient of the sphere  $C_D = 0.5$  was used. The resulting  $U_{b,c}$  for squeezing instability was shown in figure 5.3(a) using a solid line YT2025, comparing with experimental result denoted as circles. A good qualitative agreement was observed between analytical prediction and experimental result although the former prediction shows a curved line and the latter one shows a linear line.

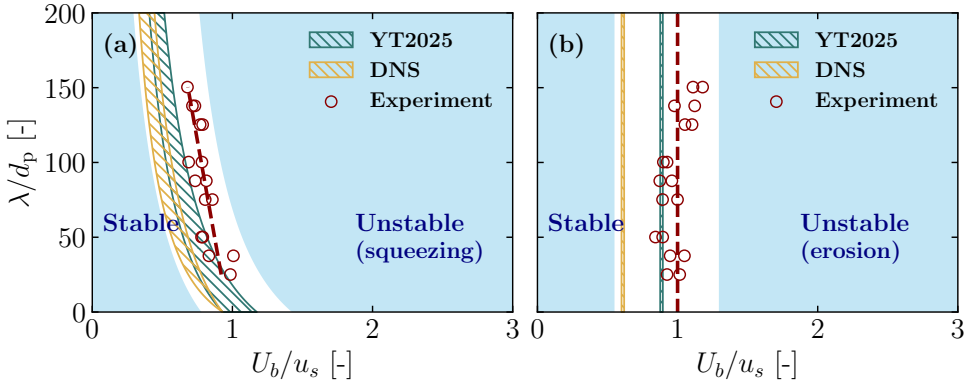


Figure 5.3: Modified stability regimes for (a) squeezing using an adapted friction coefficient of the carpet  $C_f^t$ , and (b) erosion using the an adapted drag coefficient  $C_D$  of the sphere of  $d_p = 2$  cm at the leading-edge of the carpet. The range indicates the lower bound and upper bound of threshold velocities for squeezing and erosion as discussed in Chapter 2.

Detailed understanding of hydrodynamic response to the flow transition was studied numerically in Chapter 3 using a smooth carpet and a rough carpet. Using Direct Numerical Simulation (DNS) with a volume penalisation method, the flow transition was investigated focusing on the turbulent stresses and mean velocity profiles, variations of friction coefficients, and hydrodynamic forces on the particles inside the carpet. Once the open channel flow transitions to a smooth carpet, the Blasius velocity profile was observed over a short distance, before it develops into a turbulent boundary layer where the flow approaches the fully developed flow as shown in figure 5.4(a). In case of flow transitioning to a carpet with a rough surface (figure 5.4(b)), the flow does not encounter a laminar velocity profile, and it directly transitions to turbulent boundary layer approaching the asymmetric closed channel flow.

In the asymmetric channel, the wall-normal location of maximum velocity is observed above that of zero Reynolds shear stress. Due to asymmetric roughness at the top boundary, a stronger shear stress occurs to a bottom surface, enhancing further bed erosion.

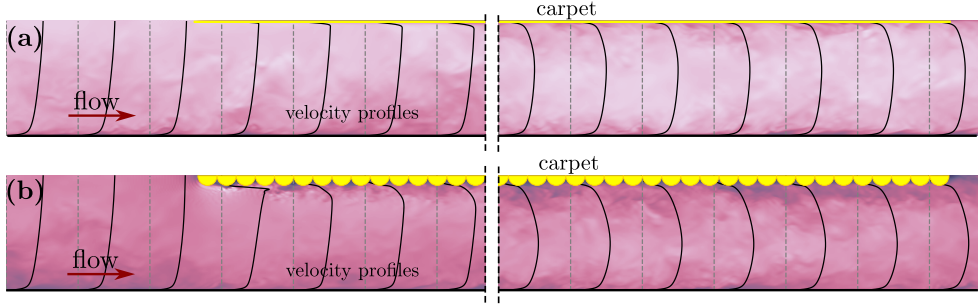


Figure 5.4: Instantaneous velocity snapshot for flow transition cases: (a) from the open-to-closed smooth channel, and (b) from the open-to-closed rough channel using DNS method detailed in Chapter 3. Streamwise averaged velocity profiles are also shown on the snapshots.

Due to the boundary layer development at the carpet, the friction coefficient  $C_f^t$  of the carpet was found to vary along the flow transition until the fully developed flow condition. To incorporate the effect of variation of  $C_f^t$  in Eq. 2.11, the averaged value  $\overline{C_f^t}$  was calculated as  $\frac{1}{\lambda} \int_0^\lambda C_f^t(x_1) dx_1$  in which  $C_f^t(x_1)$  is the numerical result from DNS, and it is larger than  $C_f^t$  of fully developed flow condition such that  $\overline{C_f^t}/C_f^t = 1.28$ . This means that the carpet-averaged friction coefficient over a developing boundary layer  $\overline{C_f^t}$  is 28% larger than the one  $C_f^t$  considering only the fully developed flow condition. With the new averaged  $\overline{C_f^t}$  in Eq. 2.19, the resulting  $U_{b,c}$  denoted by “DNS” is smaller than the result of using  $C_f^t$ , which means that considering the variation of friction coefficient provides a more lower (safer) estimate of threshold velocity of squeezing instability.

Erosion instability of the carpet is defined as the complete dislodgement of the particle located at the leading edge of the carpet as shown in figure 5.2(a) and 5.2(c), which is similar to bedload sediment transport in rivers. The mean force of the approach flow  $F_D$  is mostly responsible for this particle erosion, together with turbulent fluctuation forces  $F_a'$ . The threshold flow velocity for erosion is predicted by Eq. 2.19 which includes the drag coefficient of the sphere  $C_D$ , friction coefficient of the bottom  $C_f$ , and angle of the streamline deflection  $\alpha$ . Figure 5.3(b) compares the analytical prediction and experimental result

using the conventional value of  $C_D = 0.5$ . The angle of streamline deflection  $\alpha$  was determined using  $\arctan(U_3/U_1)$  where  $U_1$  and  $U_3$  denote the streamwise and vertical components of the velocity vector in the proximity of the leading edge of the carpet. Since erosion takes place only at the carpet's leading edge by definition,  $U_{b,c}$  depends on the approach flow velocity alone, not on the carpet length.

The presence of the carpet influences the flow dynamics and hydrodynamic forces and coefficients acting on the particles in the flow, especially near the carpet. Better quantification of  $C_D$  is required to predict  $U_{b,c}$  in Eq. 2.19, especially near the flow transition region. Therefore, Chapter 4 analysed numerically the drag and lift forces, and coefficients of the particles in the presence of the carpet. In a flow transition point, the particle experiences a strong drag and lift force due to a flow acceleration, which is very susceptible to erosion instability. For a particle located slightly downstream of the transition point, flow separation beneath the carpet is imposing larger fluctuating forces, making the particle also vulnerable to erosion. Particles located in the fully developed flow condition and underneath the carpet seem more stable because of the shielding effect by the neighbouring particles of the carpet.

Using numerical results from Chapter 4, drag coefficient of the particle at the transition point  $C_D^{\text{trans}}$  was found larger than nominal value of  $C_D = 0.5$  such that  $C_D^{\text{trans}}/C_D = 1.6$ . Using  $C_D^{\text{trans}}$  in Eq. 2.19 results in a lower estimate of  $U_{b,c}$  for erosion instability as shown in figure 5.3(b). Moreover, the standard deviation of  $F_L$  is found 6 times larger than the assumed pressure fluctuation force  $F'_a$ , therefore the assumed value was increased in the new predicted  $U_{b,c}$ . Hence, the overall stability of the carpet was safely determined by the better parametrisations of  $C_f^t$  and  $C_D$  used in Eq. 2.11 and Eq. 2.19, respectively. This means that the combined effect of spatial variation of shear stress along the carpet and flow acceleration at the transition point exerts more destabilising force on the carpet, further weakening the carpet stability.

### 5.1.1 Societal Impacts

The scientific findings of Chapter 2 will support an effective waste-collection strategy by identifying geographical locations where the flow velocity is optimal. The analytical prediction of squeezing instability will also assist quantification of cumulative shear force of the debris carpet acting on the hydraulic

structure. In addition, the predictive formula will help prevent structural failure of the waste-collection devices and assist in determining the appropriate timing for transferring collected waste from the channel to land. In other words, the appropriate collection timing corresponds to the period during which the debris carpet remains stable and does not collapse under excessive cumulative shear force.

Furthermore, understanding the mechanism of erosion instability will help estimating the immersed depth of the floating waste-collection devices, particularly in determining whether particles remain beneath the carpet or are transported downstream by the mean flow. In cases where the eroded particles remain attached to the carpet, the initially single carpet transforms to a multi-layered carpet, depending on the submergence depth of the hydraulic structure in the flow. For instance, if the submergence depth is shallow relative to the characteristic length of the debris, the eroded particles will escape the capturing zone and be transported downstream of the structure. In case of deep submergence of hydraulic structures, such multilayer development imposes additional normal forces on the structures because the particles are unable to escape and continue to accumulate.

The acquired knowledge in Chapter 3 on flow transition and an asymmetric closed channel can be beneficial to not only collecting the floating debris accumulation but also mitigation of bed erosion in the channel. Lessons learned can be used for the role of driftwood and ice-covers with respect to the interactions with hydraulic infrastructures. Knowledge of the mixing process underneath the carpet will also enhance our understanding of the transport of nutrients and energy essential to riverine ecosystems [100], for both its positive and negative impacts.

## 5.2 Outlook

This research revealed many new features on debris accumulations, but it also pointed out some additional aspects that need investigation in the future. This section discusses the future perspectives of the research and its implications for both scientific and societal aspects.

### 5.2.1 Scientific aspects

This research contributed a deeper understanding of debris accumulation at hydraulic structures in open channel flows using experimental and numerical methods. Debris accumulation studied here consists solely of mono-disperse (i.e., single type of properties) floating spheres. Therefore, to extend the validity of the analytical framework developed in Chapter 2, poly-disperse particles with various densities should be incorporated both in the theoretical analysis and in the laboratory experiments. When examining the erosion instability of a particle, it is recommended to consider the impulse-based stability criterion, as particle dislodgement is affected not only by the magnitude of the force but also by its duration. Regarding the experimental setups, Particle Image Velocimetry (PIV) technique could be considered to obtain the complete flow field near the flow transition. Moreover, computer vision techniques should also be applied to monitor the particle motion, which is important for accurately determining the threshold flow velocity for squeezing and erosion instabilities.

This study also provided fundamental insights into the flow response to the transition from an open to a closed channel, as well as the stress and velocity profiles in an asymmetric closed channel. This gained knowledge is pivotal to estimate the cumulative force of the carpet, and an increase in the shear stress at the bed erosion. Moreover, the roughness function  $\Delta U_1^+$  obtained from this study will be useful for drag modelling in large scale applications. To expand the current study, however, further research should consider a diverse range of roughness elements, and higher Reynolds number to observe its effect across scales. Since the free surface effect is clearly observable in the laboratory experiments, free surface variation should also be incorporated in the simulations instead of rigid-lid assumption, especially to study the carpet's effect on the flow upstream of the carpet. The free surface deformation at the stagnation point as observed in the experiments leads to a local increased water level and is therefore stabilising the carpet. Absence of this effect in the numerical simulation could explain the low threshold of erosion obtained from simulation data in comparison with the experiments.

The present simulation setups did not consider moving particles in the flow to study the erosion instability although quasi-static manner of the particles were included. Therefore, moving particles should be simulated in the future study to better understand the dynamics of erosion instability and de-

5 terminate the threshold flow velocity. It is noted that substantial computational resources will be required to carry out a simulation of this scale capable of capturing erosion events. However, for high-Reynolds-number flows, fully scale-resolving simulations (DNS) are still far beyond 2026's current computational capabilities for studying real-world cases. Therefore, Large Eddy Simulation (LES) or Reynolds Averaged Navier-Stokes (RANS) approaches are recommended for such kinds of large-scale applications. In that case, a two-way force coupling between the flow and the particle needs to be considered in the simulation to properly account the presence of the solid phase in the fluid phase. In this regards, it is important to note that the drag coefficient of the particle is varying in different positions with respect to the carpet, thus force parametrisation should be cautioned for the particle tracking study, especially under the debris layer, in the large-scale hydraulic model. Furthermore, to numerically simulate the accumulation process of debris, particle-particle interaction models have to be incorporated together with the two-way coupling, leading to the four-way force coupling, otherwise the particles do not interact with one another and the carpet formation will not be observed as in reality. Future research should focus on multilayered formation aspect of the debris accumulation to quantify the loadings on the hydraulic structures.

From the perspective of the operational modelling practice where details of the flows are neglected, such as non-hydrostatic pressure distribution, the effect of debris accumulation should also be added in the hydraulic modelling software suites. To this end, the momentum conservation equation of the Shallow Water Equations (SWE),

$$\frac{\partial Q}{\partial t} + \frac{\partial}{\partial s} \left( \frac{\alpha_c Q^2}{A_c} \right) + g A_c \frac{\partial h}{\partial s} + c_f^b \frac{|Q|Q}{A_c R} = 0, \quad (5.1)$$

needs to be modified by adding an extra friction term for the debris carpet such that

$$\frac{\partial Q}{\partial t} + \frac{\partial}{\partial s} \left( \frac{\alpha_c Q^2}{A_c} \right) + g A_c \frac{\partial h}{\partial s} + \left( P_b c_f^b + P_t c_f^t \right) \frac{|Q|Q}{A_c^2} = 0, \quad (5.2)$$

where  $Q$  is the flow discharge,  $h$  is the height of the free surface above the reference level (therefore,  $h = \text{datum head} + \text{water depth}$ ),  $s$  is the streamwise coordinate,  $\alpha_c$  is the coefficient of conveyance,  $A_c$  is the conveyance area,  $P_b$  is the wetted perimeter of the channel,  $P_t$  is the wetted perimeter of the carpet which is approximately equal to the width of the channel for a full carpet (figure 5.5(a)), and  $R$  is the hydraulic radius. Here,  $c_f^b$  and  $c_f^t$  in Eq. 5.2 are

defined as  $\tau_b/(\rho U^2)$  and  $\tau_t/(\rho U^2)$ , respectively. Modified momentum equation (Eq. 5.2) can be used to simulate the discharge and water level in the shallow water systems where long wave approximation is valid.

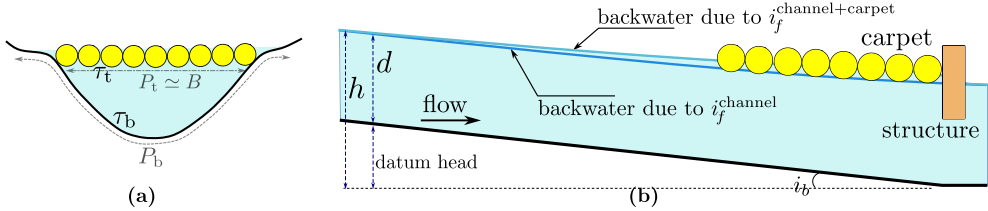


Figure 5.5: (a) Typical cross-section of a river covered with a debris accumulation where carpet's shear stress  $\tau_t$  applies over the wetted perimeter  $P_t$  and bed shear stress  $\tau_b$  applies over the  $P_b$ , and (b) longitudinal profile of a river depicting an increased backwater level due to the combined friction slope of channel and carpet  $i_f^{channel+carpet}$ , compared to the backwater rise due to solely the channel friction  $i_f^{channel}$ .

To make Eq. 5.2 simpler for the steady flow in a one-dimensional case, we obtain the backwater curve equation

$$\frac{dd}{ds} = \frac{i_b - i_f}{1 - Fr^2}, \quad (5.3)$$

in which  $d$  is the water depth,  $i_b$  is the slope of the channel bed, and

$$i_f = \left( P_b c_f^b + P_t c_f^t \right) \frac{Q^2}{A_c^2} \quad (5.4)$$

that is called the friction slope taking the contribution of carpet resistance into account. Due to this additional resistance, the increased backwater rise will occur to the channel with a debris accumulation, compared to the case with only bottom friction as shown in figure 5.5(b). Therefore, quantifying the friction coefficient of the debris carpet is essential for predicting flood levels and discharge capacity of hydraulic structures in urban drainage systems vulnerable to debris clogging.

### 5.2.2 Societal aspects

The most urgent action to prevent plastic debris from entering the ocean is to collect them from rivers, which are the main conveyors of debris transport to the ocean. Therefore, installing more waste-collection devices in rivers is

beneficial for mitigating plastic pollution. In this regard, it is recommended to install scientifically proven, well-designed devices in optimal river locations where flow velocity is not high. To achieve this, large-scale pilot projects should first be conducted in rivers or canals to evaluate the effectiveness of these devices and to use the collected data (e.g. flow velocity, water depth, amount of captured debris) to further refine the analytical models. It should be noted that some plastic debris does not float on the water surface but remains suspended within the water column. In this case, floating waste-collection devices cannot capture them effectively. Therefore, other collection methods should be considered, such as the bubble-screen technique (<https://thegreatbubblebarrier.com>) which requires energy input to operate.

Future studies should also focus on the physical and chemical processes occurring underneath the debris carpet, as this layer can block sunlight and inhibit oxygen exchange with the atmosphere, thereby impacting aquatic ecosystems. Monitoring underwater flow conditions should also be incorporated into waste-removal operations to prevent damage to the ecosystems as well as local scour. Such research will be valuable to similar physical obstacles in channels such as ice-covers and driftwood accumulations.

Regarding the impact on hydraulic structures in drainage systems, maintaining their structural reliability is crucial for ensuring user safety. This research has shown that debris accumulation can exert significant loads on these structures, potentially leading to structural damage. In addition, debris blockages in the channel can reduce the drainage capacity of hydraulic structures, increasing the risk of urban flooding. Therefore, urban planners and engineers should incorporate the effects of debris accumulation on urban hydraulic structures into their design guidelines.

For optimal debris-removal strategies, real-time sensors that detect debris loads on waste-collection devices should be installed to prevent structural failure caused by excessive loading. Furthermore, since weather conditions influence debris transport in rivers, predictive models of the carpet stability should be integrated with weather forecasting data to prevent excessive debris inflow into the collection devices.

Moreover, government agencies should support research and development (R&D) activities focused on the design of waste-collection devices and on conducting field studies. In addition, policymakers should enforce rules and regulations to control the use of plastic products and to manage waste in accordance with circular-economy principles. Startups and entrepreneurs working on plastics circularity and develop innovative alternatives to plastic should

also be encouraged and supported by local and national governments.



## References

- [1] C. d. Donaldson et al. Construction of a dynamic model of the production of atmospheric turbulence and the dispersal of atmospheric pollutants. In *Workshop on micrometeorology*, volume 313, page 392. Amer. Meteor. Soc, 1973.
- [2] R. C. Thompson, W. Courtene-Jones, J. Boucher, S. Pahl, K. Raubenhaimer, and A. A. Koelmans. Twenty years of microplastic pollution research—what have we learned? *Science*, 386(6720):eadl2746, 2024.
- [3] N. B. Hartmann, T. Huffer, R. C. Thompson, M. Hasselov, A. Verschoor, A. E. Daugaard, S. Rist, T. Karlsson, N. Brennholt, M. Cole, et al. Are we speaking the same language? recommendations for a definition and categorization framework for plastic debris, 2019.
- [4] D. Honingh, T. van Emmerik, W. Uijttewaal, H. Kardhana, O. Hoes, and N. van de Giesen. Urban River Water Level Increase Through Plastic Waste Accumulation at a Rack Structure. *Frontiers in Earth Science*, 8 (February):1–8, 2020. ISSN 22966463. doi: 10.3389/feart.2020.00028.
- [5] J. R. Jambeck, R. Geyer, C. Wilcox, T. R. Siegler, M. Perryman, A. Andrady, R. Narayan, and K. L. Law. Plastic waste inputs from land into the ocean. *science*, 347(6223):768–771, 2015.
- [6] J. W. Cottom, E. Cook, and C. A. Velis. A local-to-global emissions inventory of macroplastic pollution. *Nature*, 633(8028):101–108, 2024.
- [7] M. Ryberg, A. Laurent, and M. Z. Hauschild. Mapping of global plastic value chain and plastic losses to the environment: with a particular focus on marine environment. 2018.
- [8] The Pew Charitable Trusts. Breaking the plastic wave: A comprehensive assessment of pathways towards stopping ocean plas-

- tic pollution. [https://www.pew.org/-/media/assets/2020/07/breakingtheplasticwave\\_report.pdf](https://www.pew.org/-/media/assets/2020/07/breakingtheplasticwave_report.pdf), 2020. Accessed: November 10, 2025.
- [9] Organisation for Economic Co-operation and Development (OECD). Global plastics outlook: Policy scenarios to 2060. [https://www.oecd.org/content/dam/oecd/en/publications/support-materials/2022/02/global-plastics-outlook\\_a653d1c9/Global%20plastics%20outlook%20-%20policy%20scenarios.pdf](https://www.oecd.org/content/dam/oecd/en/publications/support-materials/2022/02/global-plastics-outlook_a653d1c9/Global%20plastics%20outlook%20-%20policy%20scenarios.pdf), 2020. Accessed: November 10, 2025.
- [10] M. H. DiBenedetto. The fluid mechanics of ocean microplastics. *Annual Review of Fluid Mechanics*, 58, 2025.
- [11] R. Brouwer, Y. Huang, T. Huizenga, S. Frantzi, T. Le, J. Sandler, H. Dijkstra, P. van Beukering, E. Costa, F. Garaventa, et al. Assessing the performance of marine plastics cleanup technologies in europe and north america. *Ocean & Coastal Management*, 238:106555, 2023.
- [12] M. D. Griffin, Z. T. Diana, R. Karasik, and M. M. Dunphy-Daly. Do plastic clean-up technologies work? what research does (and doesn't) tell us. *Marine Pollution Bulletin*, 209:116978, 2024.
- [13] M. Bergmann, H. P. H. Arp, B. C. Almroth, W. Cowger, M. Eriksen, T. Dey, S. Gündoğdu, R. R. Helm, A. Krieger, K. Syberg, et al. Moving from symptom management to upstream plastics prevention: The fallacy of plastic cleanup technology. *One Earth*, 6(11):1439–1442, 2023.
- [14] D. W. Poppema, L. Burghardt, L. Benet, D. Wüthrich, E.-M. Klopries, B. Dewals, and S. Erpicum. Bridge clogging in belgium and germany during the 2021 floods. *Water Resources Research*, 61(11):e2024WR039218, 2025.
- [15] T. Van Emmerik, T.-C. Kieu-Le, M. Loozen, K. Van Oeveren, E. Strady, X.-T. Bui, M. Egger, J. Gasperi, L. Lebreton, P.-D. Nguyen, et al. A methodology to characterize riverine macroplastic emission into the ocean. *Frontiers in Marine Science*, 5:372, 2018.
- [16] A. Marin and M. Souzy. Clogging of noncohesive suspension flows. *Annual Review of Fluid Mechanics*, 57, 2024.

- 
- [17] J. Winkelmann, A. Mughal, D. Weaire, and S. Hutzler. Equilibrium configurations of hard spheres in a cylindrical harmonic potential. *Europhysics Letters*, 127(4):44002, 2019.
- [18] A. Tordesillas and M. Muthuswamy. On the modeling of confined buckling of force chains. *Journal of the Mechanics and Physics of Solids*, 57(4):706–727, 2009.
- [19] M. R. Kuhn and C. S. Chang. Stability, bifurcation, and softening in discrete systems: a conceptual approach for granular materials. *International Journal of Solids and Structures*, 43(20):6026–6051, 2006.
- [20] S. Prakash, H. Perrin, and L. Botto. Buckling of a monolayer of platelike particles trapped at a fluid-fluid interface. *Physical Review E*, 109(1):014801, 2024.
- [21] M. Takaki and X. Gu. Motions of a floating elastic plate in waves. *Journal of the Society of Naval Architects of Japan*, 1996(180):331–339, 1996.
- [22] M. Singh, M. H. Meylan, and R. Gayen. Time-domain motion of a floating or obliquely submerged non-uniform elastic plate. *Physics of Fluids*, 35(4), 2023.
- [23] J.-C. Tatinclaux and M. Gogus. Asymmetric plane flow with application to ice jams. *Journal of Hydraulic Engineering*, 109(11):1540–1554, 1983.
- [24] R. N. Parthasarathy and M. Muste. Velocity measurements in asymmetric turbulent channel flows. *Journal of Hydraulic Engineering*, 120(9):1000–1020, 1994.
- [25] J. Guo, H. Shan, H. Xu, Y. Bai, and J. Zhang. Exact solution for asymmetric turbulent channel flow with applications in ice-covered rivers. *Journal of Hydraulic Engineering*, 143(10):04017041, 2017.
- [26] J.-S. Wang and J. P. Tullis. Turbulent flow in the entry region of a rough pipe. *Journal of Fluids Engineering*, 96(1):62–68, 1974.
- [27] J. J. Allen, M. A. Shockling, G. J. Kunkel, and A. J. Smits. Turbulent flow in smooth and rough pipes. *Philosophical Transactions of the Royal Society A: Mathematical, Physical and Engineering Sciences*, 365(1852):699–714, 2007.

- [28] K. Hanjalić and B. E. Launder. Fully developed asymmetric flow in a plane channel. *Journal of Fluid Mechanics*, 51(2):301–335, 1972.
- [29] T. Ikeda and P. A. Durbin. Direct simulations of a rough-wall channel flow. *Journal of Fluid Mechanics*, 571:235–263, 2007.
- [30] P. Bradshaw, R. B. Dean, and D. M. McEligot. Calculation of interacting turbulent shear layers: duct flow. 1973.
- [31] X. Wu and P. Moin. Direct numerical simulation of turbulence in a nominally zero-pressure-gradient flat-plate boundary layer. *Journal of Fluid Mechanics*, 630:5–41, 2009.
- [32] A. F. Mills and X. Hang. On the skin friction coefficient for a fully rough flat plate. *Journal of fluids engineering*, 105(3):364–365, 1983.
- [33] A. Rouhi, D. Chung, and N. Hutchins. Direct numerical simulation of open-channel flow over smooth-to-rough and rough-to-smooth step changes. *Journal of Fluid Mechanics*, 866:450–486, 2019.
- [34] E. J. Shaughnessy, I. M. Katz, and J. P. Schaffer. *Introduction to fluid mechanics*. Oxford University Press New York, 2005.
- [35] R. A. Antonia and R. E. Luxton. The response of a turbulent boundary layer to a step change in surface roughness part 1. smooth to rough. *Journal of Fluid Mechanics*, 48(4):721–761, 1971.
- [36] M. Li, C. M. De Silva, A. Rouhi, R. Baidya, D. Chung, I. Marusic, and N. Hutchins. Recovery of wall-shear stress to equilibrium flow conditions after a rough-to-smooth step change in turbulent boundary layers. *Journal of Fluid Mechanics*, 872:472–491, 2019.
- [37] X. Fang, M. F. Tachie, and K. Dow. Turbulent separations beneath semi-submerged bluff bodies with smooth and rough undersurfaces. *Journal of Fluid Mechanics*, 947:A19, 2022.
- [38] H. Homann, J. Bec, and R. Grauer. Effect of turbulent fluctuations on the drag and lift forces on a towed sphere and its boundary layer. *Journal of Fluid Mechanics*, 721:155–179, 2013.
- [39] L. Zeng, S. Balachandar, P. Fischer, and F. Najjar. Interactions of a stationary finite-sized particle with wall turbulence. *Journal of Fluid Mechanics*, 594:271–305, 2008.

- 
- [40] S. Balachandar and J. K. Eaton. Turbulent dispersed multiphase flow. *Annual review of fluid mechanics*, 42(1):111–133, 2010.
- [41] M. Maxey. Simulation methods for particulate flows and concentrated suspensions. *Annual Review of Fluid Mechanics*, 49(1):171–193, 2017.
- [42] J. G. B. Derraik. The pollution of the marine environment by plastic debris: A review. *Marine Pollution Bulletin*, 44(9):842–852, 2002. ISSN 0025326X. doi: 10.1016/S0025-326X(02)00220-5.
- [43] D. Ronckers, D. W. Poppema, and D. Wüthrich. Experimental study on driftwood accumulation at submerged culverts. In *Proceedings of the 10th International Symposium on Hydraulic Structures (ISHS 2024)*, pages 781 – 790, Zurich, 2024. ETH Zurich. doi: 10.3929/ethz-b-000676024.
- [44] L. J.J. Meijer, T. van Emmerik, R. van der Ent, C. Schmidt, and L. Lebreton. More than 1000 rivers account for 80% of global riverine plastic emissions into the ocean. *Science Advances*, 7(18), 4 2021. ISSN 23752548. doi: 10.1126/sciadv.aaz5803.
- [45] S. Jueyi, W. Jun, H. E. Yun, and K. Faye. Velocity profiles and incipient motion of frazil particles under ice cover. *International Journal of Sediment Research*, 25(1):39–51, 2010.
- [46] M. Peters, K. Dow, S. P. Clark, J. Malenchak, and D. Danielson. Experimental investigation of the flow characteristics beneath partial ice covers. *Cold Regions Science and Technology*, 142:69–78, 2017.
- [47] I. Schalko, C. Lageder, L. Schmocker, V. Weitbrecht, and R. M. Boes. Laboratory flume experiments on the formation of spanwise large wood accumulations: I. effect on backwater rise. *Water Resources Research*, 55(6):4854–4870, 2019.
- [48] L. Burghardt, D. W. Poppema, Loïc Bénét, D. Wüthrich, S. Erpicum, and E.-M. Klopries. Multi-lab investigation of the effect of debris composition on bridge clogging during floods. In *Proceedings of the 10th International Symposium on Hydraulic Structures (ISHS 2024)*, pages 791 – 800, Zurich, 2024. ETH Zurich. doi: 10.3929/ethz-b-000676025.
- [49] G. Piton, A. R. Ceron-Mayo, and S. Lambert. Small-scale modeling of flexible barriers. ii: Interactions with large wood. *Journal of Hydraulic Engineering*, 149(3):04022044, 2023.

- [50] I. Calmet and J. Magnaudet. Statistical structure of high-reynolds-number turbulence close to the free surface of an open-channel flow. *Journal of Fluid Mechanics*, 474:355–378, 2003.
- [51] F. M. White and J. Majdalani. *Viscous fluid flow*. McGraw-Hill New York, 2021.
- [52] E. Rathakrishnan. *Instrumentation, measurements, and experiments in fluids*. CRC press, 2007.
- [53] P. S. Jackson. On the displacement height in the logarithmic velocity profile. *Journal of fluid mechanics*, 111:15–25, 1981.
- [54] D. Chung, N. Hutchins, M. P. Schultz, and K. A. Flack. Predicting the drag of rough surfaces. *Annual Review of Fluid Mechanics*, 53:439–471, 2021.
- [55] F. T. Nieuwstadt, J. Westerweel, and B. Boersma. *Introduction to Theory and Applications of Turbulent Flows*. Springer, 2016.
- [56] W. P. Breugem, B. J. Boersma, and R. E. Uittenbogaard. The influence of wall permeability on turbulent channel flow. *Journal of Fluid Mechanics*, 562:35–72, 2006.
- [57] H. A. Einstein and E.-S. A El-Samni. Hydrodynamic forces on a rough wall. *Reviews of modern physics*, 21(3):520, 1949.
- [58] B. A. Kironoto, W. H. Graf, and Reynolds. Turbulence characteristics in rough uniform open-channel flow. *Proceedings of the Institution of Civil Engineers-Water Maritime and Energy*, 106(4):333–344, 1994.
- [59] H. Afzalimehr and C. D. Rennie. Determination of bed shear stress in gravel-bed rivers using boundary-layer parameters. *Hydrological sciences journal*, 54(1):147–159, 2009.
- [60] I. Nezu. Open-channel flow turbulence and its research prospect in the 21st century. *Journal of Hydraulic Engineering*, 131(4):229–246, 2005.
- [61] N. Saito and D. I. Pullin. Large eddy simulation of smooth–rough–smooth transitions in turbulent channel flows. *International Journal of Heat and Mass Transfer*, 78:707–720, 2014.

- 
- [62] U. Ismail, T. A. Zaki, and P. A. Durbin. Simulations of rib-roughened rough-to-smooth turbulent channel flows. *Journal of Fluid Mechanics*, 843:419–449, 2018.
- [63] C. Yan Toe, W. Uijttewaal, and D. Wüthrich. Stability of an idealized floating carpet of plastic spheres in an open channel flow. *Journal of Hydraulic Engineering*, 151(4):04025010, 2025.
- [64] H. T. Shen. Mathematical modeling of river ice processes. *Cold Regions Science and Technology*, 62(1):3–13, 2010.
- [65] I. Schalko, L. Schmocker, V. Weitbrecht, and R. M Boes. Backwater rise due to large wood accumulations. *Journal of Hydraulic Engineering*, 144(9):04018056, 2018.
- [66] H. Luo, H. Ji, Z. Chen, B. Liu, Z. Xue, and Z. Li. An analytical study for predicting incipient motion velocity of sediments under ice cover. *Scientific Reports*, 15(1):1912, 2025.
- [67] H. T. Shen and T. O. Harden. The effect of ice cover on vertical transfer in stream channels 1. *JAWRA Journal of the American Water Resources Association*, 14(6):1429–1439, 1978.
- [68] W. Huai, H. Chen, Z. Yang, D. Li, and F. Wang. Estimation of the suspended sediment concentration in ice-covered channels based on the gravitational theory. *Journal of Hydrology*, 637:131337, 2024.
- [69] S. Beltaos. River ice jams: Theory, case studies, and applications. *Journal of Hydraulic Engineering*, 109(10):1338–1359, 1983.
- [70] H. T. Shen, L. Liu, and Y. Chen. River ice dynamics and ice jam modeling. In *IUTAM Symposium on Scaling Laws in Ice Mechanics and Ice Dynamics: Proceedings of the IUTAM Symposium held in Fairbanks, Alaska, USA, 13–16 June 2000*, pages 349–362. Springer, 2001.
- [71] J. E. Zufelt and R. Ettema. Fully coupled model of ice-jam dynamics. *Journal of Cold Regions Engineering*, 14(1):24–41, 2000.
- [72] T. Van Buren, D. Floryan, L. Ding, L. H. O. Hellström, and A. J. Smits. Turbulent pipe flow response to a step change in surface roughness. *Journal of Fluid Mechanics*, 904:A38, 2020.

- [73] E. A. Fadlun, R. Verzicco, P. Orlandi, and J. Mohd-Yusof. Combined immersed-boundary finite-difference methods for three-dimensional complex flow simulations. *Journal of Computational Physics*, 161(1):35–60, 2000.
- [74] J. Kim and P. Moin. Application of a fractional-step method to incompressible navier-stokes equations. *Journal of computational physics*, 59(2):308–323, 1985.
- [75] P. Costa. A fft-based finite-difference solver for massively-parallel direct numerical simulations of turbulent flows. *Computers & Mathematics with Applications*, 76(8):1853–1862, 2018.
- [76] J. H. Ferziger, M. Perić, and R. L. Street. *Computational methods for fluid dynamics*. springer, 2019.
- [77] N. Li and S. Laizet. 2decomp & fft-a highly scalable 2d decomposition library and fft interface. In *Cray user group 2010 conference*, pages 1–13, 2010.
- [78] Fortran. Fortran 2003 draft international standard, 2004. URL <https://wg5-fortran.org/N1601-N1650/N1602.pdf>.
- [79] A. Patil, U. C. K. Paranjothi, and C. García-Sánchez. Gensdf: An mpi-fortran based signed-distance-field generator for computational fluid dynamics applications. *SoftwareX*, 30:102117, 2025.
- [80] A. E. Perry, T. T. Lim, and E. W. Teh. A visual study of turbulent spots. *Journal of Fluid Mechanics*, 104:387–405, 1981.
- [81] X. Wu. New insights into turbulent spots. *Annual Review of Fluid Mechanics*, 55(1):45–75, 2023.
- [82] J. Yuan and U. Piomelli. Roughness effects on the reynolds stress budgets in near-wall turbulence. *Journal of Fluid Mechanics*, 760:R1, 2014.
- [83] C. Chan-Braun, M. García-Villalba, and M. Uhlmann. Force and torque acting on particles in a transitionally rough open-channel flow. *Journal of Fluid Mechanics*, 684:441–474, 2011.
- [84] S. Wu, K. T. Christensen, and C. Pantano. A study of wall shear stress in turbulent channel flow with hemispherical roughness. *Journal of Fluid Mechanics*, 885:A16, 2020.

- 
- [85] J. Nikuradse et al. Laws of flow in rough pipes. 1950.
- [86] P. Burattini, S. Leonardi, P. Orlandi, and R. A. Antonia. Comparison between experiments and direct numerical simulations in a channel flow with roughness on one wall. *Journal of Fluid Mechanics*, 600:403–426, 2008.
- [87] S. A. Savelyev and P. A. Taylor. Internal boundary layers: I. height formulae for neutral and diabatic flows. *Boundary-Layer Meteorology*, 115(1):1–25, 2005.
- [88] M. Li, C. M. de Silva, D. Chung, D. I. Pullin, I. Marusic, and N. Hutchins. Modelling the downstream development of a turbulent boundary layer following a step change of roughness. *Journal of Fluid Mechanics*, 949:A7, 2022.
- [89] P. Davidson. *Turbulence: an introduction for scientists and engineers*. Oxford university press, 2015.
- [90] D. K. Tafti and S. P. Vanka. A numerical study of flow separation and reattachment on a blunt plate. *Physics of Fluids A: Fluid Dynamics*, 3(7):1749–1759, 1991.
- [91] L. Chan, M. MacDonald, D. Chung, N. Hutchins, and A. Ooi. Secondary motion in turbulent pipe flow with three-dimensional roughness. *Journal of Fluid Mechanics*, 854:5–33, 2018.
- [92] A. A. Zaidi. Particle resolved direct numerical simulation of free settling particles for the study of effects of momentum response time on drag force. *Powder Technology*, 335:222–234, 2018.
- [93] A. O. Celik, P. Diplas, C. L. Dancey, and M. Valyrakis. Impulse and particle dislodgement under turbulent flow conditions. *Physics of Fluids*, 22(4), 2010.
- [94] A. Yousefi, P. Costa, and L. Brandt. Single sediment dynamics in turbulent flow over a porous bed—insights from interface-resolved simulations. *Journal of Fluid Mechanics*, 893:A24, 2020.
- [95] W. Chester, D. R. Breach, and I. Proudman. On the flow past a sphere at low reynolds number. *Journal of Fluid Mechanics*, 37(4):751–760, 1969.

- [96] T. A. Johnson and V. C. Patel. Flow past a sphere up to a Reynolds number of 300. *Journal of Fluid Mechanics*, 378:19–70, 1999.
- [97] N. I. K. Ekanayake, J. D. Berry, and D. J. E. Harvie. Lift and drag forces acting on a particle moving in the presence of slip and shear near a wall. *Journal of Fluid Mechanics*, 915:A103, 2021.
- [98] P. Shi and R. Rzehak. Lift forces on solid spherical particles in unbounded flows. *Chemical Engineering Science*, 208:115145, 2019.
- [99] F. Kamoliddinov, I. U. Vakarelski, and S. T. Thoroddsen. Hydrodynamic regimes and drag on horizontally pulled floating spheres. *Physics of Fluids*, 33(9), 2021.
- [100] T. D. Prowse. River-ice ecology. ii: Biological aspects. *Journal of Cold Regions Engineering*, 15(1):17–33, 2001.

# Acknowledgements

This thesis is the final product of amazing teamwork.

First of all, Marjan, Wim, and Matthijs worked together to fund this Ph.D thesis financially and logistically. Of course, Lindsey and Veronique also played an important role in keeping everything running smoothly amid my difficult circumstances. Bert and Marten from Rijkswaterstaat are also acknowledged here for their financial support of this work.

I should say that writing an acknowledgements section is not an easy task, as an accidental omission or mistake may cause confusion or hurt feelings among colleagues and friends. I will do my best, and I ask for forgiveness in advance for any unintentional oversights.

I would like to express my deepest gratitude to those who supported me through the saddest experience of my life, the sudden passing of my father. In particular, Jennifer, Kshitiz and Sriya, Su, Stuart and Patricia, Afia, Pyae Phio Kyaw, Marjan, Veronique, and Lindsey helped me enormously, in ways ranging from providing meals to mental support.

I would like to sincerely thank my supervisors, Wim and Davide, for guiding me through this journey. From both of you, I learned how to conduct research. I am also very grateful to have worked alongside Akshay (who also taught me how to run numerical simulations properly), Baptiste, and Pedro, who supported me in publishing my second paper in the Journal of Fluid Mechanics. I would also like to acknowledge Freek from IHE Delft, and Frans and Frank from Deltares for their valuable insights into practical applications.

I would also like to thank Ton and Marcel for their advice and guidance ahead of my postdoctoral interview at Utrecht University. I feel very fortunate to have had the chance to speak with both of you, true experts in your respective fields.

I also had a wonderful time in Waterlab, though it is hard to do justice to everyone here. Marijn has been a true cheerleader for me, and Eki has been an invaluable advisor to international colleagues on matters such as allowances,

taxes, housing, and translation, and friend to me. Thanks also to Jelle and Jianwei for making our office alive, and to Patricia, Kshitiz, Jill, Ana, Kifayath, Claudia, Alejandra, Gladys, and Michael for sharing this PhD journey with me. Thank you all for the memories.

I would also like to thank Waterlab's technical support team, and especially Chantal, for her flexibility.

Being a fellow of the TU Delft Global Initiative has been a privilege, opening doors to people with diverse backgrounds and perspectives. I am inspired and motivated by its mission to tackle real-world societal challenges. Thank you, Claire, Roel, Rezi, and the wider community.

The Green Village has felt like home throughout this entire process. Thank you, Tim, Jean-Paul, and others, for solving every technical problem that came my way. I have also cherished living there alongside my fellow villagers, especially Inna and her family.

I would also like to thank my wonderful girlfriend, Jennifer, who has supported me in every dimension of my life, mentally, emotionally, and practically. We share the same values and tastes, which matters more than people might think.

Finally, my family has been my greatest source of strength throughout. Thank you to my brother, who has devotedly cared for our mother and father in my absence, as I have been away from home for so long. My father and mother have always been so proud of me. I think of my father every single day— his humour, his warmth, and his generosity.

မယ်မယ်၊ ဘဘ နှင့် ကိုကိုတို့ကို အများကြီးကျေးဇူးတင်ပါတယ်လို့ မှတ်တမ်းတင်ပါရစေ ခင်ဗျား။ ငယ်စဉ်ကတည်းက လိုလေသေးမရှိ ကျွေးမွေးပြုစုစောင့်ရှောက်ပေးတဲ့ ကျေးဇူးတရားများကိုလည်း အောက်မေ့မိပါတယ်ခင်ဗျား။ မိသားစုခက်ခဲနေစဉ်ကာလမှာ ကူညီစောင့်ရှောက် အားဖြည့်ပေးကြတဲ့ ဆွေမျိုးသားချင်း မောင်နှမများကိုလည်း ရင်ထဲကနေ လှိုက်လှိုက်လဲ့လဲ့ ကျေးဇူးတင်ကြောင်းမှတ်တမ်းတင်ပါရစေခင်ဗျား။  
ရုတ်တရက်ခွဲခွာသွားတဲ့ ဘဘကိုလည်း နေ့စဉ်နဲ့အမျှ သတိရတမ်းတလွမ်းဆွတ်လျက်ပါ ခင်ဗျား။

# Curriculum vitae



Chit Yan Toe was born in Palaw, Myanmar, on 9 August 1993. He studied for a Bachelor of Engineering, specialising in river and coastal engineering, at the Myanmar Maritime University from 2009 to 2014. He continued his studies with a Master of Science in Civil Engineering at Delft University of Technology from 2016 to 2018. During his M.Sc. studies, he specialised in Environmental Fluid Mechanics, focusing on processes from rivers to oceans, particularly computational methods and theoretical approaches.

After his master's studies, he returned to Myanmar to serve at Myanmar Maritime University as a lecturer in river engineering and introductory computational hydraulics. He also participated in Myanmar–Dutch joint projects as an independent modelling expert during this time.

From December 2021 to December 2025, he conducted his Ph.D research at his alma mater, TU Delft, on the topic of plastic debris in open channel flow.

After completing his Ph.D., he began his research on plastic debris in coastal waters at Utrecht University as a postdoctoral researcher on 1 June 2026.

He loves reading and collecting books.



# Scientific output

## Journal Publications

- **2025:** *Stability of an Idealized Floating Carpet of Plastic Spheres in an Open Channel Flow*  
**Chit Yan Toe**, Wim Uijttewaal, Davide Wüthrich  
*J. of Hydraul. Eng.*, **151**(4):04025010, 2025
- **2026:** *Numerical analysis of flow and stress redistribution at an open-to-closed channel transition caused by floating debris carpets*  
**Chit Yan Toe**, Wim Uijttewaal, Baptiste Hardy, Akshay Patil, Pedro Simões Costa, Davide Wüthrich  
*J. of Fluid Mech.*, **1027**(A18), 2026
- **2026:** *Hydrodynamic forces on the positively buoyant particles in an open-channel flow with a floating carpet*  
**Chit Yan Toe**, Wim Uijttewaal, Davide Wüthrich  
(in preparation for publication)

## Conference Presentations

- **2022:** *Predicting the flow and transport of plastic debris in open waters*  
**Chit Yan Toe**, Wim Uijttewaal, Davide Wüthrich  
*NCR DAYS 2022: Anthropogenic Rivers*
- **2022:** *Different approaches for particle representation in plastic debris transport models*  
**Chit Yan Toe**, Wim Uijttewaal, Davide Wüthrich  
*River Flow 2022: Proceedings of the 11th Conference on Fluvial Hydraulics*
- **2022:** *Modelling of Plastic Waste Accumulation at Hydraulic Structures*

**Chit Yan Toe**, Wim Uijttewaal, Davide Wüthrich

*Proceedings of the 7th IAHR Europe Congress (Athens, 2022)*

- **2023:** *Carpet Formation due to Accumulation of Floating Plastic Debris at Hydraulic Structures*

**Chit Yan Toe**, Wim Uijttewaal, Davide Wüthrich

*JMBC Symposium 2023*

- **2024:** *Accumulation of floating particles at hydraulic structures*  
Antonio Magherini, **Chit Yan Toe**, Laura M. Stancanelli, Davide Wüthrich,  
Wim Uijttewaal  
*NCR DAYS 2024: Tomorrow's Rivers*

## *The Legacy*

*"The shrines where you bowed in prayer,  
The radiance of Truth, and the torch of Wisdom—  
May they remain, brilliant and glowing,  
long after you are gone."*

*Zaw Gyi (1907-1990)*

သင်္ဃေသွားသော်

"သင်ဦးချ၍ အမျှဝေရာ  
စေတီသာနှင့် သစ္စာအရောင်  
ဉာဏ်တန်ဆောင်လည်း  
ပြောင်လျက်ဝင်းလျက် ကျန်စေသတည်း။"

ဇော်ဂျီ (၁၉၀၇-၁၉၉၀)